Flow-Induced Vibrations of foreign objects inside steam generator's tube bundle

by

Sahil Mahey

A thesis
presented to the University of Waterloo
in fulfillment of the
thesis requirement for the degree of
Master of Applied Science
in
Mechanical and Mechatronics Engineering

Waterloo, Ontario, Canada, 2017

I hereby declare that I am the sole author of this thesis. This is a true copy of the thesis, including any required final revisions, as accepted by my examiners.

I understand that my thesis may be made electronically available to the public.

Abstract

Flow induced vibrations of foreign objects were studied experimentally at University of Waterloo's water flume facility. The main objective of this study was to understand the three dimensional dynamic response of foreign objects inside normal triangle tube bundle and estimate semi-empirically the amount of time taken by these objects to cause critical wear damage to the tube bundle tubes. Based on the information obtained from previous Foreign Objects Search and Retrieval (FOSAR) activities , the dynamic response of wire and plate samples each with non-dimensional length L/D = 2.8, 3.4, 4.0 and 4.6 were studied at Re_D = 36,257 and 42,682, and Tu = 2.0% and 7.5%, respectively. They were placed inside tube bundle in the shape of a hook, which allowed pitching motion, yawing motion and Z direction translation motion. Using Archard's semi-empirical wear equation and available wear coefficients, wear was estimated for tubes made from I600 and I690 material, due to vibration of foreign objects made from S409, S403 and S304 material.

Experimentally recorded three dimensional dynamic response of the foreign objects showed that these objects are undergoing stationary random vibration. The Z amplitude response is significantly higher than the response in X and Y direction. For all the foreign objects with measurable vibration response, the contribution of yaw component to the overall motion is negligible, meaning that foreign objects are exhibiting planar response. As a result, the dynamic interaction between foreign object and tube bundle tube surface will only be of sliding type. Additionally, it was observed that the planar response has significant contribution from both pitching and Z translation motion component.

Parametric study showed that the geometry of the foreign object affects its RMS amplitude, with wire samples having larger RMS amplitude than plate samples. The non-dimensional length (L/D) affects the response of the foreign object depending on its geometry. The RMS amplitude of wire samples did not show any significant change with the change in L/D, whereas only plate samples of L/D = 3.4 and 4.0 showed measurable vibration response. Moreover, both wire and plate samples are more likely to vibrate in high Reynolds number flow environment, and the amplitude of vibration decrease with increase in turbulence intensity for all foreign objects samples studied. Comparing current results with the results from previous studies showed that even small changes in the foreign object's geometry could result in significant variation in RMS amplitude.

Wear analysis showed that both wire and plate samples had a potential to do critical wear damage (i.e. wear out 40% of tube wall thickness) within four year period as the flow velocity is increased. Influence of material combination on foreign object related wear is more significant in low flow velocity environment. Geometry of the foreign object also affects the critical wear time with wear due to plate samples being more aggressive than

wire samples. Additionally, it was shown that foreign objects vibrating in high turbulence intensity environment had higher critical wear time. Similar to material combination, effect of geometry and turbulence intensity becomes progressively more significant as the velocity decreases. Based on the results obtained in this study, during FOSAR activities, priority should be given to foreign objects found in high flow velocity and low turbulence intensity environment, since these objects are more likely to vibrate and cause critical wear damage within four year time period.

Acknowledgments

I would like to thank my supervisor, Prof. Serhiy Yarusevych. Your guidance and support have been invaluable.

I would also like to thank my fellow students, Chris Morton, Tom Kirk, Jeff McClure, Andrew Lambert, Jia Cheung Hu, John Kurelek, Eugene Zivkov, Ajith Airody, and Brian Kettlewell for their help when needed.

I am thankful to University of Waterloo's machine shop staff for their guidance.

I would finally like to thank Natural Sciences and Engineering Research Council, Babcock and Wilcox Canada, and the University of Waterloo for their financial support for my research.

Dedication

Dedicated to my parents Usha Rani Mahey and Jagdish Lal Mahey.

Table of Contents

List of Figures

List of Tables

List of Nomenclature

A_X, A_Y, A_Z	amplitude of displacement time realization in X,Y, and Z direction, respectively
$\bar{A}_X, \bar{A}_Y, \bar{A}_Z$	mean amplitude of displacement time realization in X,Y, and Z direction,respectively
A'_X, A'_Y, A'_Z	rms amplitude of displacement time realization in X,Y, and Z direction, respectively
B_o	axis of rotation for pitching motion
B_c	axis of rotation for yaw motion
B_r	central axis of the longer leg of foreign object
C_n	normal force coefficient
D	tube diameter
D_h	diameter of foreign object hook
d_w	diameter of wire samples
d_p	width of plate samples
E	Young's modulus
e	number of tubes in contact with the foreign object
F_n	normal force on the tube bundle tube due to foreign object
F_N	drag force on foreign object
f	frequency
G_{ZZ}	power spectral density of displacement time realization
H	critical depth of the wear scar
h	thickness of tube-bundle tube
h_p	thickness of plate samples
I	moment of inertia
K	sliding wear coefficient
L	length of foreign object
m	maximum width of the wear scar
P	pitch of tube bundle

p	point on foreign object where vibration data is recorded
p_D	shortest distance of point p from axis B_o
Q	wear volume
q_c	critical wear volume
Re_D	reynolds number based on D, $\frac{\rho U_p D}{\mu}$
$Re_{d,wire}$	reynolds number based on d_w, $\frac{\rho U_p d_w}{\mu}$
$Re_{d,plate}$	reynolds number based on d_p, $\frac{\rho U_p d_p}{\mu}$
R_{ZZ}	autocorrelation of displacement time realization in Z direction
S_d	sliding distance
S_v	sliding velocity
T	critical wear time
Tu	turbulence intensity
t	time
U_o	free-stream velocity
U_p	pitch velocity
$\bar{U}$	mean streamwise velocity
u, v, w	image coordinates
X, Y, Z	streamwise, transverse and spanwise directions, respectively
ρ	density of water
α	contact angle
θ	pitch angel
ϕ	yaw angle
τ	time delay
ν	poisson's ratio
μ	dynamic viscosity

Chapter 1

Introduction

Nuclear power plants are an important source of energy in many countries around the globe [3]. Steam generators used in nuclear power plants are one of its key components. The purpose of the steam generator is to extract thermal energy produced from the fission reaction, which is then used to run turbines and produce electricity. Additionally, it also acts to prevent the highly pressurized radioactive coolant on the primary side from leaking into the environment. Primary side of a steam-generator contains fluid which brings in the heat produced at the core of a nuclear reactor. This heat is then transferred to the low pressure fluid present in the secondary side through tube bundle. The three steam generator designs commonly used in power plants are as follows:(i) the recirculating vertical U-tube steam generators,(ii) the once through steam generators,(iii) and the horizontal boiling steam generators [4–6]. The similarity in the above mentioned designs is the use of tube-bundle to transfer heat from primary side to secondary side fluid. Since steam generator tubes separate the radioactive and non-radioactive fluids, it is very important to prevent any tube degradation that can eventually lead to its rupture. The tube degradation mechanisms are mainly related to corrosion, fatigue, and wear [5–7]. In recent years, the

use of better corrosion resistant materials has reduced the failure of tubes due to corrosion, leaving wear-related damages as one of the main source of tube failures [4]. The flow-induced vibration experienced by the steam generator tubes cause the tubes to slide against the anti-vibration bars or against each other resulting in tube wear. Another important source of wear caused on the tubes surface is the foreign objects(or loose parts).

During steam generator's regular operation, foreign objects often get logged inside the tube-bundles, which often results in extensive damage to the tubes [4,6,8]. Realitive motion between foreign object and tube-bundle tube leads to tube wall thinning and rupture. Past experiences have shown that foreign-objects-related wear has sometimes resulted in leakage of highly radioactive fluid, which then got released into the environment through pressure release valves present in the secondary side of a steam generator [6, 7, 9]. Thereby foreign objects not only cause a potential risk to environment, but are also costing power plants hundreds of thousands to millions of dollars for every forced outage [8]. Hence, it is important to understand three dimensional dynamic response of foreign object inside tube bundle to better understand foreign-object-related wear damage.

The data collected from previous Foreign Objects Search and Retrieval (FOSAR) activities have shown that these objects vary not only in shape, size, and mass, but also have highly unpredictable configuration inside the tube bundle [8,10]. All these parameters infulence foreign object's dynamic behaviour inside tube bundle. Moreover, the flow around the foreign objects logged inside the tube bundle also directly influence the dynamic behaviour of the foreign object. Complex flow enviroment inside tube bundle result in non-uniform velocity and turbulence intensity along foreign object's entire length [11,12]. The flow may or may not have oscillatory behaviour depending on the geometry of the heat exchangers

tube arrays, pitch-to-diameter ratio and Reynolds number [13]. In addition, random pressure fluctuations that are always present inside the tube-bundle for all Reynolds number can also influence the object dynamic response greatly.

The possible flow-induced vibration that the foreign object can undergo when inside the tube bundle is the vortex-induced vibration, galloping vibration, vibration induced by oscillating flow and/or turbulence induced random vibration. When exposed to sufficiently high cross-flow velocity structures shed vortices. These vortices result in a periodic forcing on the structure surface causing a periodic response. This type of vibration response in called Vortex-Induced Vibration(VIV) [14]. Similarly, galloping is also a periodic response, but it is produced due to non-periodic loading on the structure. [14–16]. Finally, the Vibration-induced by oscillatory flow is another excitation phenomena that could result in periodic response of the structure as a consequence of fluctuating flow around the structure. In contrast, random vibration due to turbulence is a non-periodic response. For this type of vibration a statistical approach is required to analyse the motion [13, 14]. Nevertheless, all of the above-mentioned phenomenons are highly coupled fluid structure interaction problems.

The dynamic of foreign objects influence the type of surface interaction taking place between foreign object and tube bundle tubes. As a result, these objects can damage tubes through sliding, fretting, impact and sliding, or impact and fretting wear, which inflicts different amount of damage on the tubes [13, 17, 18]. Hence, to properly access foreign objects related damage, there is a need to identify the type of wear process the tube-bundle tubes experiences due to foreign objects. The amount of wear experienced is also dependent on the foreign object material, contact angle, normal force, and the amount of

time they are in contact with each other [13, 19]. Sliding distance, one of the main factors is also directly influenced by the object's dynamic response inside the tube-bundle.

Overall, the dynamic response of the foreign objects is complex and not well understood. Most previous studies focuses on the wear estimates using the response of the tubes, rather than the response of foreign objects [19–22]. Since majority of objects are found right above the tube sheet where the tube response is minimum. The amount of wear estimated using the above analysis cannot fully explain the wear observed during FOSAR activities. To the best of author's knowledge, work done by Alquaddoomi and Catton [23] and Bonilla et al. [1] are the only studies that have looked at the response of the foreign object, focusing on the effects of upstream velocity and object's geometry. However, no wear analysis was done in their work. Hence, there is a need to study the dynamic response of the foreign objects to enable a better estimation of foreign objects related wear.

This study focuses on characterizing the three dimensional dynamic response of the foreign objects in a tube bundle. The aim is to identifying the parameters influencing the response of the object and to estimate the associated wear. The main objectives of this work are as follows:

1. Studying the effects of length, geometry, upstream velocity, and turbulence intensity on the three dimensional response of the foreign object.

2. Identifying the type and amount of wear the foreign objects can cause to the tubes in a common steam-generator design.

Detailed literature review is provided in Chapter 2. The experimental set up is discussed

in Chapter 3, followed by comprehensive analysis of the results in Chapter 4. Finally, the concluding remarks and recommendations are presented in Chapter 5 and 6, respectively.

Chapter 2

Background

This chapter gives an overview of foreign objects characteristics, excitation mechanisms and wear types. Details about stream-generator's design are given in Section 2.1, followed by discussion on history and characteristics of these objects inside tube bundles in Section 2.2. Section, 2.3 and 2.4, discuss the flow behaviour inside tube bundles and possible foreign object's excitation mechanisms, respectively. Finally Section 2.5, highlights possible wear types the steam generator tubes can experience due to foreign objects, including previous studies on foreign objects related wear.

2.1 Steam Generator Design

Stream generators are an essential part of a nuclear power plant. A typical plant has two to six steam generators, with larger plants having as many as twelve [4]. Shell-and-tube is the commonly used steam generator design in nuclear industry. Three popular shell-and-

tube stream-generator designs are as follows:(i) the recirculating vertical U-tube steam generators,(ii) the once through steam generators,(iii) and the horizontal boiling steam generators [4–6]. These steam generator designs allow heat transfer, without letting the radioactive and non-radioactive fluid getting mixed.

Most popular among the three is the recirculating U-tube steam generator [4]. The cross-section of typical recirculating steam generator is shown in Figure 2.1. The fluid flowing inside the tubes is called primary fluid, while the fluid flowing over the tubes is called secondary fluid. These recirculating steam generators typically have between 2000 to 15000 tubes, depending on power plant's capacity. [4, 6]. The primary fluid velocity ranges within 0.9-2.4 m/s, whereas secondary fluid velocity range is usually within 0.6-1.5 m/s [24]. For this steam generator (Figure 2.1), the primary fluid carrying thermal energy produced by the fission reaction enters the steam generator through primary inlet. It passes through the U-tubes before exiting from primary outlet. The secondary fluid enters the stream generator through feedwater inlet, where it mixes with the fluid draining from steam separators. This fluid then travels through the downcommer and enters the tube bundle at about 90^o to the tubes. The secondary fluid, as it passes through tube bundle, absorbs heat and gets converted into steam. This stream exits the generator through steam outlet. The tubes inside the steam generator are mainly arranged in either in-line, rotated square, parallel triangle or normal triangle configuration (Figure 2.2). The staggered layout results in more compact tube arrangement [24]. This provides higher heat transfer rates and more rigid tube-sheet, but also makes cleaning of the tube sheet area and Foreign Object Search and Retrieval (FOSAR) activities difficult [24].

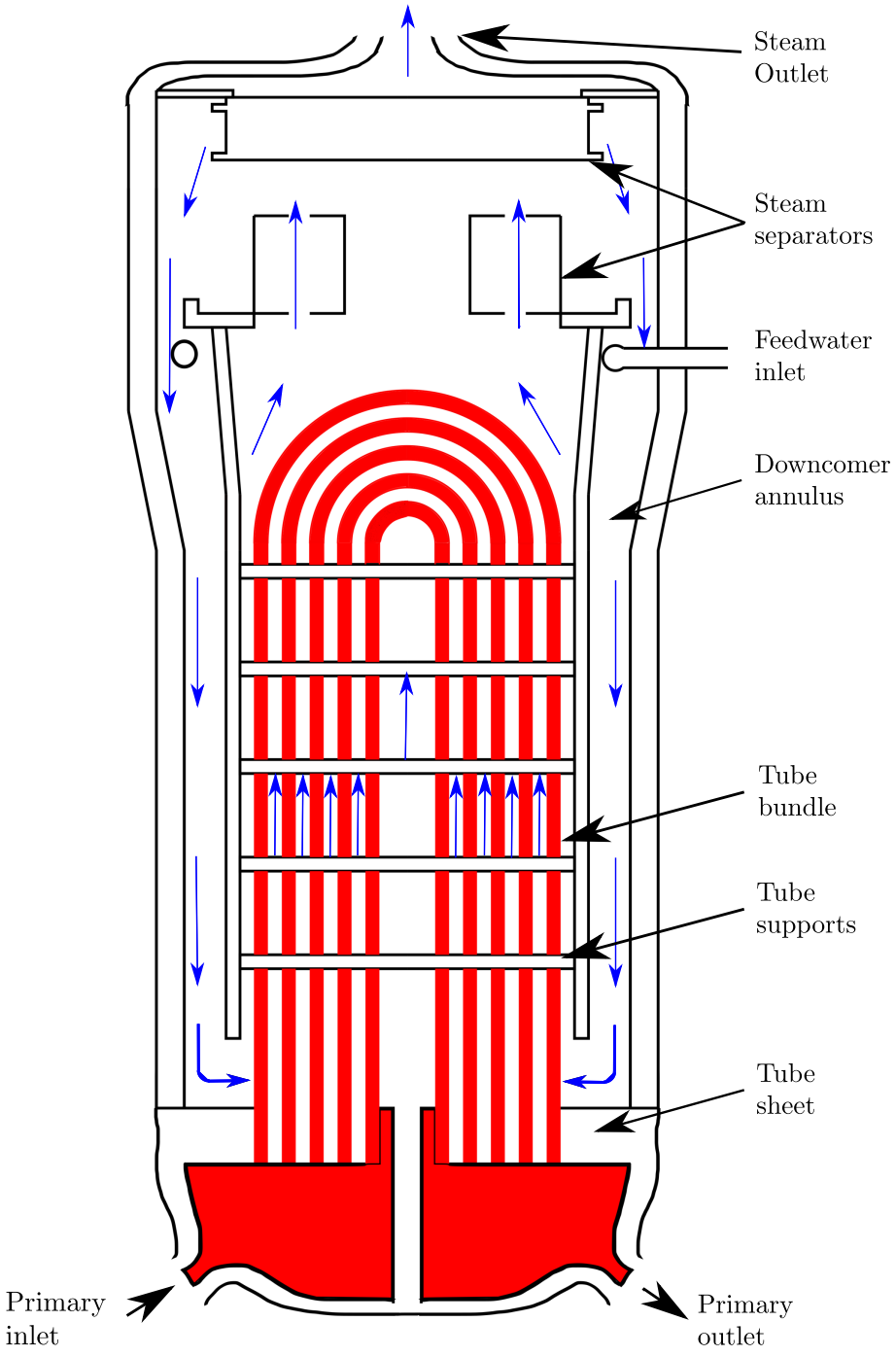

Figure 2.1: Recirculating U-tube steam generator cross section. Adapted from [4]

The once-through stream generators is the second most popular design in North America, mainly used in Canada's CANDU and U.S. power plants [25]. This design experience less intrusion of the tube bundle by the foreign objects, hence, foreign objects are not the main source of tube damage [4, 6]. Finally, the horizontal boiling steam generators are used in Russian designed power plants [6]. These stream generators also have lower risk of foreign objects related tube degradation, instead, corrosion is the main source of tube damage [6]. Most of previous FOSAR activities data on foreign objects related wear is retrieved from the power plants that have recirculating or once through type steam generator designs [4, 9, 26, 27]. Of particular interest to this study is the area above tube sheet in the recirculating stream generators, where most foreign objects related damage occurs [4, 6–8].

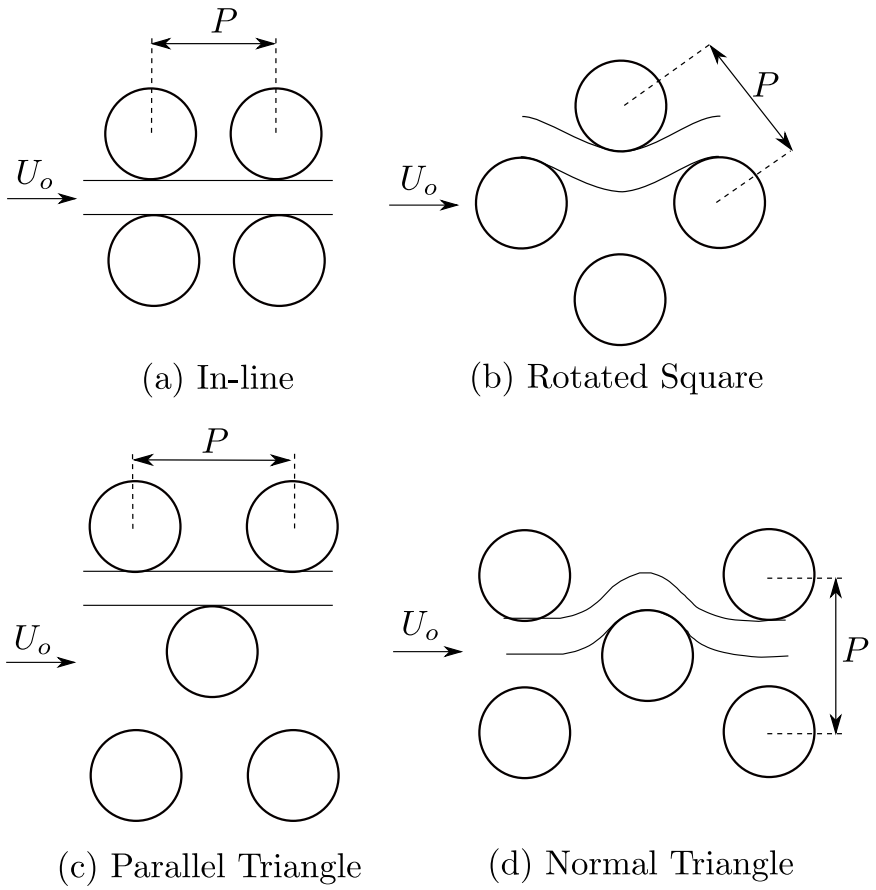

(a) In-line (b) Rotated Square

(c) Parallel Triangle (d) Normal Triangle

Figure 2.2: Commonly used array geometries in steam generators. Adapted from [13]

2.2 Foreign Objects

Wear due to foreign objects started emerging as a problem in late 1970s [8]. Between 1978 to 2005, foreign objects have resulted in eight major primary-to-secondary leakage incidents in U.S. alone [8]. In addition, there were multiple other incidents where foreign objects that have resulted in tube damage were detected and removed from the tube bundle preventing possible tube rupture [4]. These objects were either left behind during

the maintenance activity or were a part of broken components [26]. Nuclear power plants have a scheduled refuelling outage period once every four years [28]. The FOSAR activities and other maintenance related actives are usually scheduled during this period. Any unscheduled outage results in damages ranging from hundreds of thousands to millions of dollars [8]. Therefore, every effort is made to remove foreign objects that are detected during the regular outage. If the removal is not possible, it is important to at least assess the possible damage that it can cause to steam generator tubes.

One of the early incidents resulting in forced outage due to foreign objects was the Ginna power plant event in 1982 [4, 6]. In this incident, steam generator's tubes damaged as a result of foreign objects were plugged without removing the foreign objects, which eventually lead to multiple tube ruptures. As a consequence, Nuclear Regulatory Commission (NRC) recommended visual inspection of the tube sheet area to detect and remove foreign objects [29]. In addition, Loose Part Monitoring System (LPMS) was also recommended to be installed in all power plants to detect any foreign objects as soon as they are introduced into the steam generator. This system is not 100% reliable and the removal of foreign objects that are detected by the LPMS is not always possible because of geometric constrains, lack of appropriate tools, etc. Moreover, steam generators with staggered tubes arrangement makes it difficult to retrieve foreign objects during the FOSAR activities compared to tube bundles with square arrangement [24].

In 1990s, despite the increased awareness due to foreign objects related damage, the frequency of foreign objects related incidents has not reduce [8]. For this reason, many steam generator manufactures have proposed foreign objects exclusion systems to trap the objects before they get logged inside the tube bundle. A review by Electric Power Research

Institute (EPRI) on accessing the trapping capabilities of these systems [8], have shown that these systems are capable of trapping most but long slender objects.

Data collected from previous FOSAR activities show that about 90% of these foreign objects are found within first five rows of the tube bundle [4, 6–8]. Most of these objects and related tube damage are found near the tube sheet. This is the area where the flow velocity is maximum, and the first few rows are in cross flow orientation. The foreign objects vary in shape, size, mass, and material type [9, 26]. Wire and Metal gasket type objects accounts for more than 50% of the foreign object population recovered during the FOSAR activities [30]. A Report released by EPRI has mentioned that the majority of these foreign objects are long and slender [8]. In addition, the report also mentions the typical length of these objects to be around 0.25 inches. Most of these objects, however do not result in tube damage. The most damaging objects have a length between two to three inches [30].

2.3 Flow inside tube-bundle

Foreign objects are logged inside a tube bundle and their vibration response, which cause tube damage depends on the flow behaviour. Flow around tubes inside an array of tubes behaves differently from the flow around single cylinder. As discussed in previous section, tubes inside a steam generator are mainly organised in four different arrangements (Figure 2.2). It is difficult to retrieve foreign objects from a tube bundle with staggered arrangement when compared to an in-line arrangement [24]. Therefore, objects when stuck inside a tube bundle with staggered tube arrangement are often left inside until specialized tools are

developed to retrieve them during future outage period. This study focuses on staggered tube bundle with normal triangular geometry and the flow behaviour in such arrangement is discussed here. This section discusses interstitial(i.e. between tubes) flow, and development of turbulence intensity and vortex shedding inside such geometry.

The geometry of an array plays a significantly role in influencing the flow behaviour inside tube bundles. Consider Figure 2.2, for an in-line and parallel triangular tube bundle, the flow form 'straight' lanes between adjacent tube columns. In contrast, the normal triangular and rotated square tube arrangements force the flow to follow 'a wavy' path [11,12]. Zukauskas [11,31] has compared the flow in normal triangle tube bundle to flow in a channel with alternating contraction and expansion. As the flow moves through normal triangular tube bundle it experiences variation in velocity and turbulence intensity [11,32]. Zdravkovish [33], conducted pressure measurements around tubes situated in first few rows of the normal triangular tube bundle, and concluded that the pressure distribution around the tubes past the third row stays very similar. The variation in pressure distribution around the tubes seen in the first three rows can be attributed to the difference in the shape of near wake behind the first rows compared to subsequent rows (Figure 2.3). The flow moving around a tube in first row experiences higher acceleration between adjacent tubes in that row, where the gap is minimum (M_1 on Figure 2.3). For these tubes, the separation occurs around 90^o mark resulting in wider wake. This wider wake further restricts the effective flow area (M_2 on Figure 2.3) as the flow moves towards the tubes in second row resulting in an increase in favorable pressure gradient. This followed a small adverse pressure gradient, before another flow acceleration near the 90^o mark (M_3 on Figure 2.3), past which the adverse pressure gradient forces the flow to separate. The wake

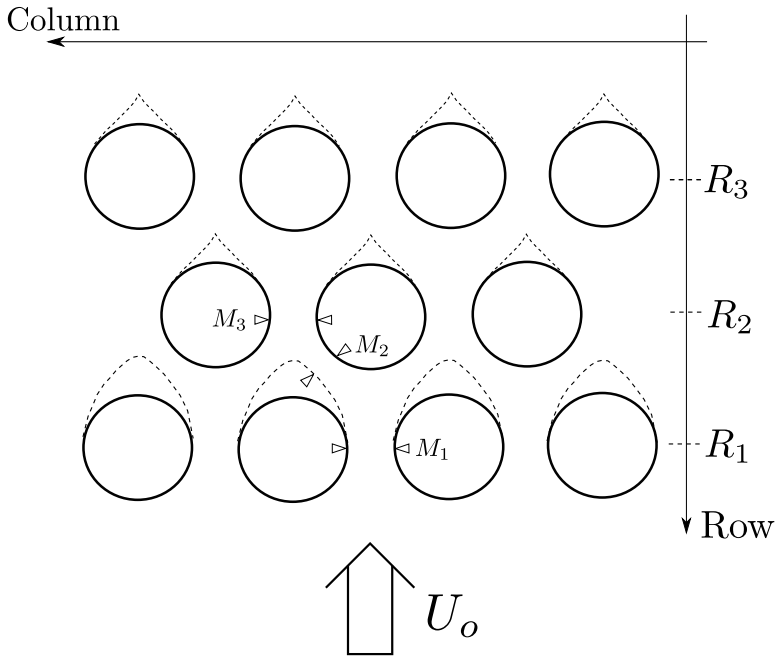

Figure 2.3: Interstitial flow in normal triangular tube bundle. Adapted from [33]

shape stays similar from the second tube onwards, hence, the variation in the effective flow area around the tubes from third row onwards stays similar resulting in similar pressure distribution.

Tube-bundles acts as grid and generator turbulence as the flow passes over the tubes. Previous studies have shown that for staggered array, the turbulence intensity increases significantly in the first four rows [34,35]. The rate of turbulence generation and dissipation reaches equilibrium after 4th row. The turbulence intensity in the first few rows of the tube bundle ranges from 10% to 50%. In addition, the flow experience large turbulence intensity fluctuations as it moves around every tube [36].

This complex flow environment inside tube bundle leads to confusion about the exis-

tence of vortex shedding inside the tube bundle in early years [13, 14]. Owen [37] argues that vortex shedding cannot occur inside tube bundle because of the chaotic nature of the flow. Later, a flow visualization study done by Abd & Weaver [38] , showed vortex shedding in rotated square tube bundle. Similar observations are reported in the visualization study done investigating vortex shedding in normal triangular tube bundle [12,39]. Additionally, other studies reported the existence of multiple peaks (up to three) in the turbulence spectra recorded inside of the normal triangular tube bundle [39–42]. Polak and Weaver [39], recorded alternate vortex shedding from the first tube bundle row. Ziada [12], in his experiments recorded alternate vortex shedding from the first row and simultaneous vortex shedding from the second. Experiential studies leads to the conclusion that the vortex shedding inside of tube bundle depends on tube bundle geometry, tube location, P/D, and Reynolds number [40, 43]. This discussion will be focused on the vortex shedding in the periphery(first four-to-five rows) of the normal triangular tube bundle. The P/D influences the number of peaks in the turbulence spectra recorded inside tube bundle [39]. Ziada and Oengoren [42], gives a rough classification of the normal triangular tube bundle into small ($P/D \leq 1.8$), intermediate ($1.8 < P/D < 2.7$) and large ($P/D \geq 2.7$) tube spacing, based on the number of peaks observed in the turbulence spectra. They recorded upto three peaks listed in increasing order (f_1, f_2, f_3) in the turbulence spectra inside the first five rows of the tube bundle. They attributed $f_3 \& f_2$, to the alternate and symmetric vortex shedding by the tubes in the first and second row of the tube bundle respectively, while $f_1 = f_3 - f_2$ is due to non-linear interaction between the other two peaks. Tube bundle with small ratio has stronger f_3 frequency content, intermediate ratio has strong $f_2 \& f_3$ frequency contents and large ratio has stronger f_2 frequency content. Tubes bundle inside

steam generators used in nuclear power plant have P/D ranging from 1.2 to 1.5 [13], hence the discussion will focus on the vortex shedding in tube bundle with small ratio. Ziada and Oengoren [42], based on previous studies provided the following empirical equation of Strouhal number to predict flow periodicity (f_3) in normal triangular tube bundle.

$$St_g = \frac{1}{2.4((P/D)-1)^{0.41}}$$

For the given P/D, the vortices shedding from the first tube rows disperses very rapidly as it moves towards the second row [44]. Hence, the peak in the turbulence spectra is limited to the tubes in the first row only. Ender and Moller [31], studied four P/D ratio ranging from 1.05 to 1.60 and found that behind the second and third row of the tube bundle, decreasing P/D ratio suppress the peak in the turbulence spectra. In addition, as the P/D decreases and Reynolds number increases the peak in the turbulence spectra will become weaker and wider [14, 43].

2.4 Flow-induced vibration

Foreign objects placed in such complex flow environment will experience non-uniform velocity and turbulence intensity across its entire length. When logged inside the tube bundle, foreign object's interaction with the surrounding fluid produce forces on its surface, which may result in vibration response. Alquaddoomi & Catton [23], studied the dynamic repose of foreign objects by placing them in front of the first row of tube bundle, perpendicular to upstream flow and tube axis. They observed random vibration of foreign objects.

However, no study is yet performed to understand dynamic response of the foreign objects logged into the tube bundle. This section describes the possible flow induced vibration mechanisms that foreign objects may experience inside the tube bundle.

2.4.1 Vibration due to Oscillating flow

Objects placed in oscillating flow environment can result in resonant vibration response leading to system vibrating at its natural frequency [14]. Foreign objects logged in tube-bundle might experience this type of vibration because of the periodic vortex shedding from the inlet tubes. Such response occurs when the flow is oscillating at a frequency matching the natural frequency of the structure and can be suppressed if the external forcing is weak [14]. The vibration of the rigid or flexible objects due to the periodic vortex shedding from the upstream cylinder or periodic nature of the ocean waves have been studied extensively, for example, cantilever beam placed behind bluff body shedding vortices, ship motion due to ocean waves or petroleum pipe lines responding to sea currents [14, 45, 46]. Periodic vortex shedding from the inlet tubes does happens in staggered tube bundle. But for tube bundle with small P/D ratio weak vortex shedding is expected only in the first row of the tube bundle. Therefore for such cases, the resonant response of the foreign objects because of the weak periodic vortex shedding from upstream cylinder is unlikely in the current tube-bundle.

2.4.2 Vortex-Induced Vibration (VIV)

When a bluff body is subjected to sufficiently high cross flow it shed vortices [13, 14]. Consider a cross section of a bluff body such as a circular cylinder (Figure 2.4). The adverse pressure gradient faced by the flow as it moves around the cylinder's widest point, results in a boundary layer separation forming two separated shear layers. As the flow velocity increases, these shear layers roll into vortices that shed alternately from each end. This is a periodic shedding process which is a function of Reynolds number, $Re_d = \frac{\rho d U_o}{\mu}$, where, ρ is density of the fluid, d is the characteristic length of the bluff body, U_o is the flow velocity and μ is the dynamic viscosity of the fluid. It is commonly represented by the Strouhal number, $S = \frac{f_s d}{U_o}$ where f_s is the shedding frequency.

The alternate vortex shedding from the bluff body, results in net fluctuating lift force on its surface which can lead to Vortex induced vibration response(VIV). Blevins [14], has provided extensive literature review on this topic. For large VIV to occur, the induced forces needed to be coherent over the span of the bluff body and have forcing frequency near the natural frequency of the structure [13,14]. When the shedding frequency is synchronized with the natural frequency of the structure, a lock-in effect occurs [14]. When this occurs the shedding frequency looks onto the natural frequency for a range of upstream flow velocity. During this effect, the object can vibrate with relatively high amplitude. The VIV is a self limiting vibration phenomenon, i.e. outside this lock-in band of reduced velocities the system's vibration response is negligible.

For foreign objects to experience VIV, vortex shedding must occur from the object, and result in forces with good coherence over its span. Foreign objects are placed in highly

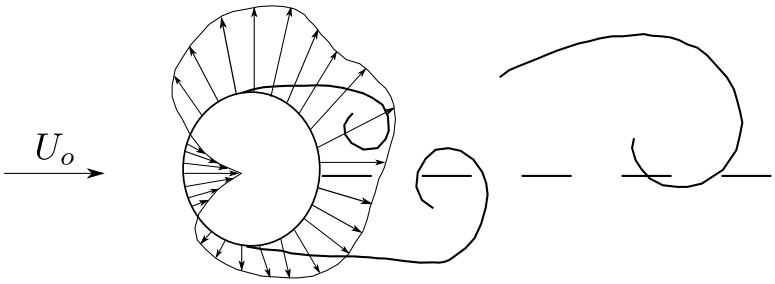

Figure 2.4: Instantaneous pressure distribution on cylinder shedding vortices in cross flow. Adapted from [14]

unsteady, three dimensional and turbulent flow environment. In such flow environment, the vortex shedding will likely be influenced by flow velocity, turbulence intensity, blockage ratio, yaw angle and interference effects [36]. The velocity and turbulence intensity is non-uniform throughout the entire length of the foreign object. Under such condition, the shedding frequency is expected to vary along the span of the foreign object. Griffin [47], suggested that in non-uniform flow a bluff body shed vortices in multiple cells, characterized by different shedding frequency. Similarly, varying turbulence intensity across object's span will also result in varying shedding frequency [47]. In addition, inside normal triangular tube bundle the blockage ratio is also changing along the span of the foreign object. Richter & Naudscher [48], in their experiment on circular cylinder in cross flow have reported that the shedding frequency increases with the increase in blockage ratio. Therefore, part of foreign objects placed in high blockage ratio area will likely shed vortices at higher frequency. Hence, this changing blockage ratio also results in different shedding frequency across foreign object span. This variation in the shedding frequency due to non uniform velocity, turbulence intensity and blockage ratio leads to the reduction in the correlation length of the induced fluctuating force on the foreign object.

Moreover, inside the tube bundle the angle between flow and foreign object is changing across the span of the object. For an object placed at an angle to the free stream velocity, the shedding frequency becomes a cosine function of a yaw angle [49, 50]. Similarly, the force acting on it will also become a function of this angle, hence reducing the magnitude of the force [36]. Hence, the changing angle further adds to the reduce correlation length and magnitude of the induced forces.

The parameters discussed so far either reduces the correlation length and/or the magnitude of the force, but do not completely suppress the vortex formation. Inside normal triangular tube geometry with small P/D, the tubes in the vicinity of foreign object are highly likely to interfere in vortex formation process. Jubran et al [51], in their study concluded that the presence of interfering body in the wake of a bluff body suppress vortex shedding. For most of its length, foreign object will have tube present near it. Therefore foreign object's area in the vicinity of tube bundle tube will not shed vortices because of the interference effect.

Overall, foreign objects inside normal triangular tube bundle with small P/D will experience vortex shedding only in the area that is away for the tube. This vortex shedding will be incoherent and will result in weaker force. Therefore, under such constrains it is highly unlikely that the foreign object will experience VIV.

2.4.3 Galloping

Galloping is a self-excitation flow induced vibration phenomenon [52]. Unlike VIV, the forces required for galloping response are the consequence of the motion of the structure

itself. Galloping results in a large amplitude response, usually occurring at the lowest natural frequency of the structure. This type of vibration is usually associated with the structures that have non-circular cross-section [15, 16]. For example, consider the bluff body presented in Figure 2.5. The flow separate at the sharp edges of the front face, as a result the two shear layers encloses the whole body behind the front face. The forces required for galloping response exists primarily on this portion (after separation) of the structure [15]. Parkinson [15], view this in terms of "inner circulation flow", which for this example would result in low pressure on bottom surface and high pressure on top. The downward motion of the structure causes the lower shear layer to move closer and become more curved, while the top shear layer move away and become less curved. Consequently, the instantaneous net pressure force (F) generated on the body, is in the same direction as the instantaneous velocity of the structure ($\dot{z}$) resulting, in negative damping. For systems with negative damping, the energy from the flow is encouraging the motion of the structure. The amplitude of vibration, continue to grow until the damping become positive again. In contrast to VIV, galloping is not self-limiting, and the amplitude of vibration increases with increasing cross-flow velocity.

The galloping response is influenced by the Reynolds number, afterbody shape and length, aspect ratio, cross-sectional shape, and turbulence intensity. The vibration amplitude of galloping structure increases with increase in Reynolds number [14]. Additionally, structure's afterbody shape and length also significantly influence the galloping response [14, 15, 53]. Objects with no 'afterbody' do not gallop [15]. Here, afterbody refers to the part of bluff object downstream of the separation point, which in case of bluff body shown in Figure 2.5 is the whole body behind the front face. The afterbody is important

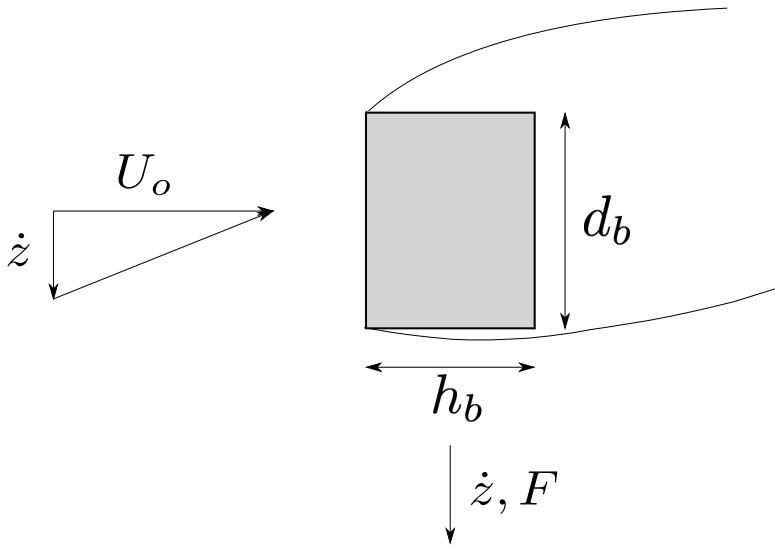

Figure 2.5: Galloping structure in cross flow. Adapted from [56]

because the forces required for system oscillation exist mainly in this area. Experiment conduced by Toebes & Eagleson [54] have shown that the structure without afterbody oscillates with significantly smaller amplitude compared to the structure with afterbody.

Aspect ratio ($\frac{h_b}{d_b}$) of the object, determine whether the structure will have soft or hard galloping response [53]. Soft galloping built up spontaneously from rest where as the hard galloping requires initial input. Parkinson [55], in his experiments on cylinders with rectangular cross-section have shown that, objects will have soft galloping response if the aspect ratio is between 0.75 and 4. As the aspect ratio is decrease to be between 0.375 and 0.75 the object will show hard galloping response [53, 55]. Nakamura and Tomonai [56], in their experiments, on the rectangular cross-section prisms confirms that critical aspect ratio for the onset of soft galloping is 0.75.

The foreign objects under consideration have circular (for wire samples) and rectan-

gular (for plate samples) cross-section. While cylinders with rectangular cross-section can produce galloping response, cylinder with circular cross-section placed in normal cross-flow are however immuned to such instability [53]. Nevertheless, circular cylinder placed in yawed and/or inclined position have been shown to produce galloping response [57]. For yawed and/or inclined cylinder, the component of velocity along the axis of the cylinder disrupts the interaction between the two separated shear layers resulting in net force on object's afterbody. Matsumoto et al [57], showed that interrupting the velocity component along the axis of the cylinder prevent galloping response in yawed cylinders.

In addition, Turbulence intensity also have a significant effect on the galloping response of the objects. Nakamura and Tomonai [56], have shown that the critical $\frac{h_b}{d_b}$ ratio for the onset of soft galloping decreases with increase in turbulence intensity. Laneville and Parkinson [58], showed that increasing turbulence intensity causes the soft galloping to unstable, and hard galloping to become weaker.

Overall, the aspect ratio of the foreign object with rectangular cross-section used in this study ($\frac{h_b}{d_b} < 0.375$), is below the minimum aspect ratio required for galloping response. Foreign objects with circular cross-section are placed at a yaw and inclined position to the flow, but the presence of stem-generator tubes and constant change in the flow angle with respect to the cylinder axis, is expected to interrupt the axial component of the flow along its span hence suppressing or minimizing any galloping type response. In addition, for the part of cylinder, that is away from the tubes, high turbulence intensity would weaker the net galloping force generated, if they are generated. Therefore, for this study both rectangular and circular geometry are not expected to gallop, once logged inside of tube bundle.

2.4.4 Turbulence-Induced Vibration

The random pressure fluctuations inside the tube bundle can result in the random response of the structure such as foreign object. This was first reported by Alquaddoomi & Catton [23], in their experiments on foreign objects made of wire and metal gasket, by placing them normal to upstream flow and tube axis in front of the first row of tube bundle tubes. In this orientation, the metal gasket sample did not vibrate, whereas the wire sample responded in random manner. In turbulent flow environment, the surrounding fluid imposes random pressure forcing function on the surface of the structure [14]. This random forcing function results in a random response of the structure that cannot be expressed in terms of a deterministic mathematical function [59]. Statistical approach is usually used when dealing with structure vibrating in random manner [13,59]. The random vibrations are influenced by the forcing function and vibrating structure characteristic.

The turbulent flow results in a random pressure forcing function acting on the foreign object inside tube bundle. The parameters that influence the random vibration response are the integral length scale and turbulence intensity [60]. In the periphery of steam generator, the correlation length is influenced by upstream turbulence integral length scale [61]. If the force acting on the structure is completely uncorrelated, the structure will not vibrate [13]. Savkar et al [62] studied the correlation length effects on the forces of the cylinder by varying the upstream turbulence length scale using grids of different sizes while keeping turbulence intensity constant. They found that the net unsteady forces on the cylinder increase with increasing integral length scale of the upstream turbulence. Gorman [63] studied the effects of upstream turbulence on the vibration response of the peripheral

tubes in tube bundle. He attributed the reduction in the tube vibration to the break down of the correlation length by the upstream grid. For tubes away from periphery, Owen [37] argued that the effect of upstream turbulence is negligible. For such tubes, the random vibrations are largely influenced by the turbulence generated inside the bundle, but the integral length scale would be relatively small deep inside the tube bundle [61].

In addition, to the large correlation length, the energy of the excitation forces need to be large enough to cause large random response [60]. Bruun & Davies [64] studied the influence of upstream turbulence intensity on the unsteady forces acting on a cylinder placed in cross-flow. They showed that, increasing the turbulence intensity by just increasing the Reynolds number results in the reduction in spanwise correlation and net random forces acting on the cylinder. The random forcing function acting on a vibrating system is typically characterized by the PSD function which can be wide or narrow and probability density function(PDF) which can be Gaussian or non-Gaussian [14].

For linear random vibration analyse, the forcing function is assumed to be stationary and ergodic [13,65]. By doing so, all the statistical quantities, such as mean, mean square, variance and standard deviation can assumed to be independent of time and space. According to random vibration theory, for a given system characteristics and power spectral density (PSD) of the forcing function, the mean square response of the system can be given as [13],

$$\langle z^2 \rangle = \int_{-\infty}^{\infty} S_z(\omega) d\omega = \int_{-\infty}^{\infty} |H(\omega)|^2 S_f(\omega)$$

where $S_z(\omega)$ is the system response PSD, $S_f(\omega)$ is the forcing function PSD, and $H(\omega)$ is the frequency response function. The random vibrating system is characterised by the

root mean square and power spectral density of the response function [14]. This PSD of the responce can be narrow or wide band process depending on the structure under consideration. Elastic structures such as tubes in tube bundle tends to vibrate at its natural frequency. When wide band random forcing function acts on it, the response will be dominated by narrow band of frequencies centred around the natural frequency of the structure [14], resulting in narrow band response. For weekly resonant or non-resonant response, the wide band forcing function spectra results in wide band response spectra.

In conclusion, the geometry of the tube-bundle and/or foreign objects under study will likely not permit vibration due to oscillating flow, VIV and/or galloping response of foreign objects. The highly turbulent flow environment inside of the tube bundle, however would produce random forces on the object's surface. Whether or not these foreign objects would vibrate because of these random forcing function would highly depend on correlation length and turbulence energy in the flow. The correlation length tends to be large in the periphery of the tube bundle and decreases in the inner regions. Therefore, it is highly likely that the excitation forces are well correlated with high energy atleast in the peripheral region of the tube bundle, resulting in foreign objects possibly respond in random manner.

2.5 Tube Wear

Studying vibration response of foreign objects is important, as such response may result in wear related tube damage. Wear refers to the removal of material due to mechanical causes i.e., relative motion between two surfaces in contact [17, 18]. Wear process which is defined by the characteristics of relative motion and geometry of the two surfaces in

contact leads to different amount of wear. Most common wear processes inside the steam generator are fretting wear, impact wear and impact fretting wear [13, 66]. In addition, sliding and impact sliding have also been observed in some parts of steam generator [67]. Sliding wear occurs due to sliding type contact, mainly for sliding distance larger than 300 μm occuring between the two surfaces in contact [17,18,67–69]. Fretting on the other hand occurs due to very small amplitude (between 20-300 μm) reciprocating motion between two surfaces in contact [17, 68, 69]. Impact wear is beacuse of repeated hammering or impact, resulting in wastage of material [70]. Whereas, impact fretting and impact sliding are the combination of impact and fretting or impact and sliding wear processes, respectively.

As the two surfaces interact with each other, depending on the wear process they experience different wear mechanisms which are usually one or more of the following four: adhesive wear, tribo-oxidative wear, abrasive wear and contact fatigue wear [17,18]. Adhesive wear occurs due to the atomic bonds formed between the contacting asperities, if the strength of adhesive force is large enough it could result in material removal during relative motion. Tribo-oxidative wear occurs due to interaction of the surface with environment containing oxygen, producing brittle oxide layer which is chipped away during relative motion. Abrasive wear is due to hard particles on base or counter body ploughing through or plastically removing the weak surface during its movement [17]. Finally, contact fatigue is due to reciprocating loading on the contacting surfaces, results in surface crack, a growth of crack and removal of material. Wear mechanisms during sliding wear process are adhesive and/or tribo-oxidative, which determines the amount of material removed [17]. Fretting has contact fatigue or tribo-oxidative type wear mechanisms, each occurring depending on the amount of peak-to-peak displacement during reciprocating motion between contact

surfaces. Finally, fatigue wear mechanism results in material removal during impact wear process.

For tubes inside tube bundle, the removal of 40% of the wall thickens is considered as critical wear [10, 22]. Depending on the dynamic response of foreign objects inside tube bundle, the tubes may experience sliding wear, fretting wear or impact fretting/sliding type wear process. Wear due to pure sliding should be greater than pure fretting wear [71]. Archard & Hirst [72] proposed an empirical relation for wear due to sliding motion between two components. According to their analysis, the volume removed can be calculated as:

$$Q = K F_n S_d \tag{2.1}$$

where Q is the wear volume, K is the wear coefficient, F_n is the normal contact force and S_d is the total sliding distance. Equation 2.1, is also used to express volume removed due to fretting wear [73]. Stowers & Rabinowicz [73] and Connor [74] have used this equation 2.1 to calculate fretting wear on tube bundle tubes inside steam generator. While, Hong et al. [66] and Kwon et al. [75], have used modified form of equation 2.1 to analyze impact-fretting type wear. However, Equation 2.1 relies on experimental data to determine the term on right hand side.

The critical wear volume depends highly on the geometry of the contacting surfaces [13]. Jo et al [22], in their analysis used a simplified expression to calculate critical wear volume based on the geometric relation between the wear volume and critical wear depth. This expression is for flat foreign objects in contact with the steam generator tube (Figure 2.6). The critical wear volume can be related to tube diameter(D) by the following expression

[22], $Q = \frac{D^2 L_s [2\alpha - sin(2\alpha)]}{8}$, where, L_s is the length of wear volume, α is a contact angle, and it related to critical depth and the wear scar width (m) as, $\alpha = cos^{-}1(1 - \frac{2H}{D})$.

For this study, emperically obtained wear coefficients by previous researchers are used to estimate foreign object related wear. The wear coefficient (K) depends on the type of materials in contact and the ambient conditions [13]. For example, stainless steal Alloy 301 when sliding against tubes made from Alloy I600 would wear the tube twice as fast compared to Alloy 409 sliding against Alloy I600 [26]. Similarly, ambient flow conditions such as temperature have significant effect on the wear rate. Fisher & Guerout [76], studied the effects of temperature, water chemistry and tube material on the fretting wear. They have shown that temperature and tube material have significant effect on the wear coefficient, where as the water chemistry has a negligible affect. Steam generator tubes are commonly made from stainless steal Allow I800, I600 or I690 [4, 26]. Multiple studies have calculated fretting wear coefficient (K) for various materials commonly used in nuclear industry and found that the coefficient lies between 1.4E-15 to 104.4E-15 Pa^{-1} [26, 68, 71, 74, 76–83]. However, fewer studies have focused on determining sliding wear coefficients for materials used in nuclear industry [67, 80, 84, 85].

Previous studies have assumed fretting wear process when analysing the wear of the steam generator tubes as a result of foreign objects using Equation 2.1 [19–22, 26]. Jo et al [22] studied the wear damage due to foreign objects rubbing against the vibrating tube. They found the flow velocity, which governs the normal force between two surfaces, to be a major factor in determining the remaining life of the tube, and increasing it could reduce tube bundle tubes to its critical depth within a year. In a similar experiment, Kim et al [20], proposed a simplified vibration model for the steam generator tubes to calculate

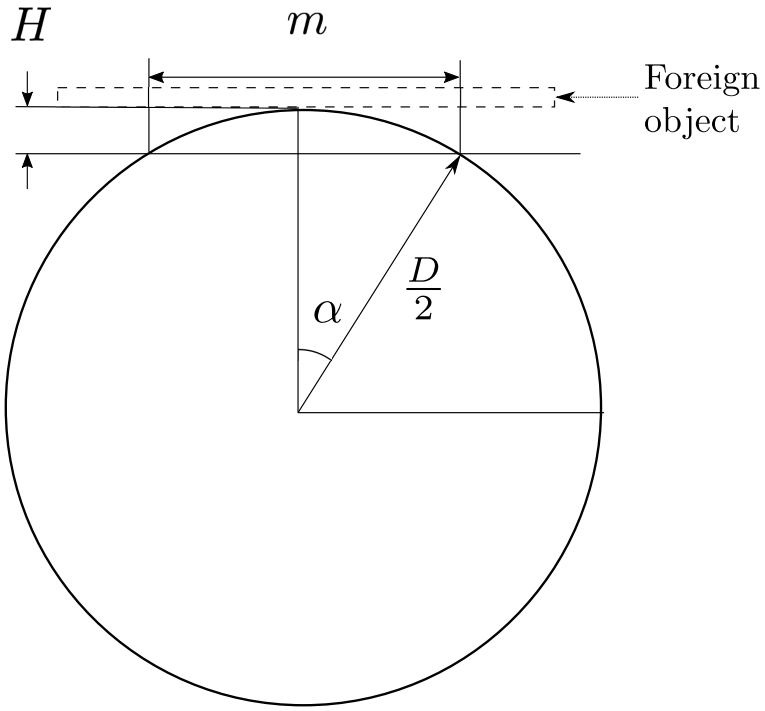

Figure 2.6: Critical wear on tube bundle tube due to foreign object. Adapted from [22]

sliding distance.

Overall, foreign object's physical characteristics and location inside steam generator are obtained from previous studies(Section 2.1 and 2.2). In this location, the flow field is highly complex(Section 2.3), and the interaction of foreign objects with such flow environment might result in flow induced vibration(Section 2.4). This vibration response in conjunction with empirically derived wear coefficients discussed in this section will be used to estimate the amount of time required for foreign objects to wear out steam generator tubes to its critical depth.

Chapter 3

Experimental Methodology

3.1 Experimental Facility

All experiments were performed at University of Waterloo's water flume facility (Figure 3.1). The flume is supplied through an elevated constant head tank, with the flow rate controlled using a gate valve located in the settling chamber. Inside the flume, the water passes through the settling chamber and flow conditioners before reaching the test section. The flow conditioning elements consists of a combination of honeycombs and screens to reduce the turbulence intensity below 3% and a flow uniformity within 1%. The test section is 2.4 m long and has a normal cross-section area of 1.2 by 1.2 m. The flume walls in the test section are made from 19 mm thick glass to allow optical access.

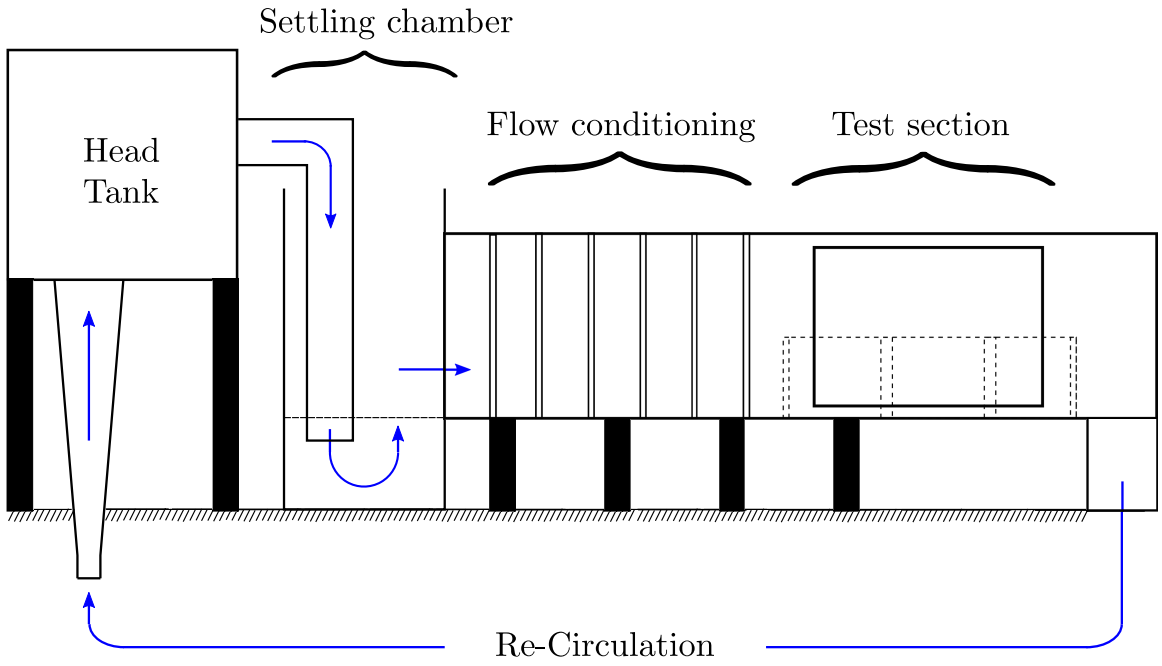

Figure 3.1: University of Waterloo's water flume facility.

3.2 Experimental Set-up

The test set-up consists of converging-diverging channel, turbulence generating grid, tube bundle and foreign objects. The isometric view of the overall setup is shown in Figure 3.2.

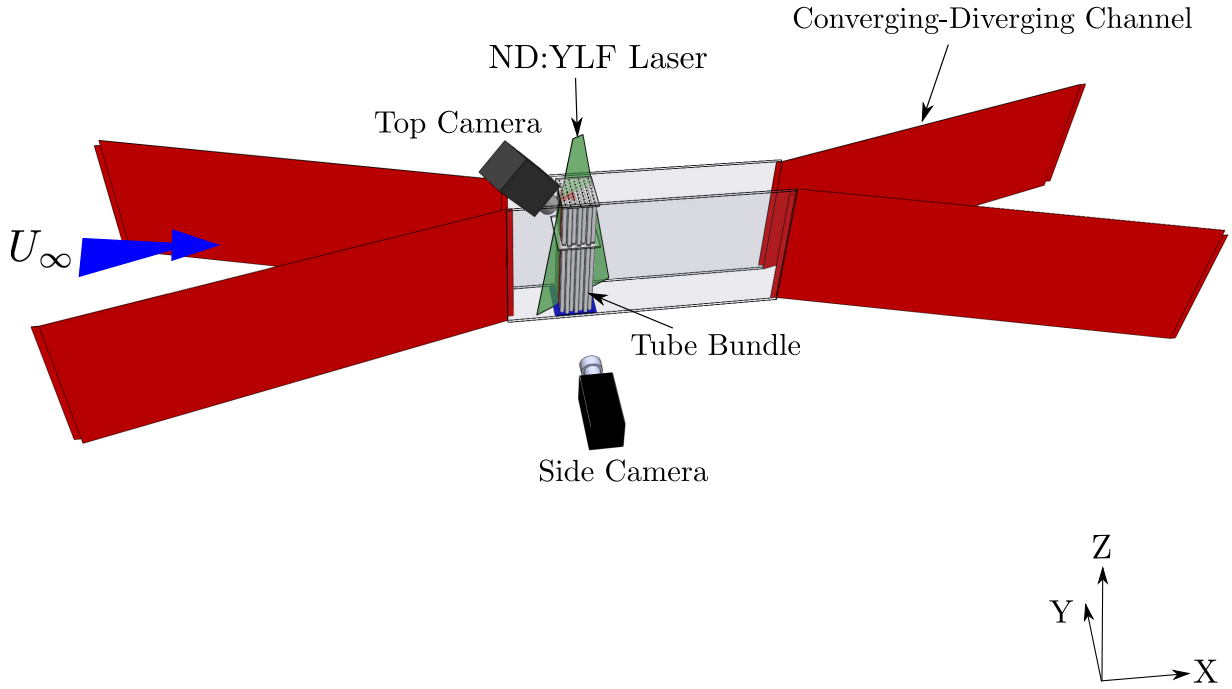

Figure 3.2: Isometric view of experimental set-up.

Without the converging diverging channel, the maximum flow velocity inside the test section was 0.08 m/s. For the present experiment, the test section of the flume was modified to facilitate higher flow rates. In particular, the channel with aspect ratio of 6:1 was installed to increase the flow velocity upstream of the tube bundle. Figure 3.3, shows the top view of the channel installed in water flume's test section. Its throat had a cross-sectional area of 0.63 by 0.20 m and length of 1.2 m. Its walls were made from 12.7 mm thick acrylic glass for optical access. The maximum flow velocity upstream of the tube-bundle after installing the channel was 0.54 m/s ($Re_{D,U_o} = 9,478$) without upstream grid and 0.64 m/s ($Re_{D,U_o} = 11,126$) with upstream grid installed.

Experiments at higher turbulence intensity were conducted by installing square mesh grid with mesh size of 43.5 mm (2.5D) and thickness of 8 mm (0.46D) upstream of the tube bundle. The grid was installed at the inlet of the throat section and the distance between the grid and tube bundle was 342 mm (19.6D). The mesh was created based on the recommendation of Roach [86], to create homogeneous, isotropic turbulence upstream of the tube bundle. Stream wise turbulence intensity decays downstream of the square mesh grid. This decay was measured by measuring the turbulence intensity at multiple stream wise locations downstream of the grid. The turbulence intensity in the throat upstream of tube bundle was below 2% and flow uniformity within 4% without the grid present. However, with the grid installed, the turbulence intensity increases to 7.5% with flow uniformity below 15%.

The tube bundle's design was based on B&W's steam generator model installed in Braidwood Nuclear Power Plant, Unit 1. Tubes with outer diameter (D) of 17.46 mm were used to build this bundle. They were arranged in normal triangular arrangement with P/D

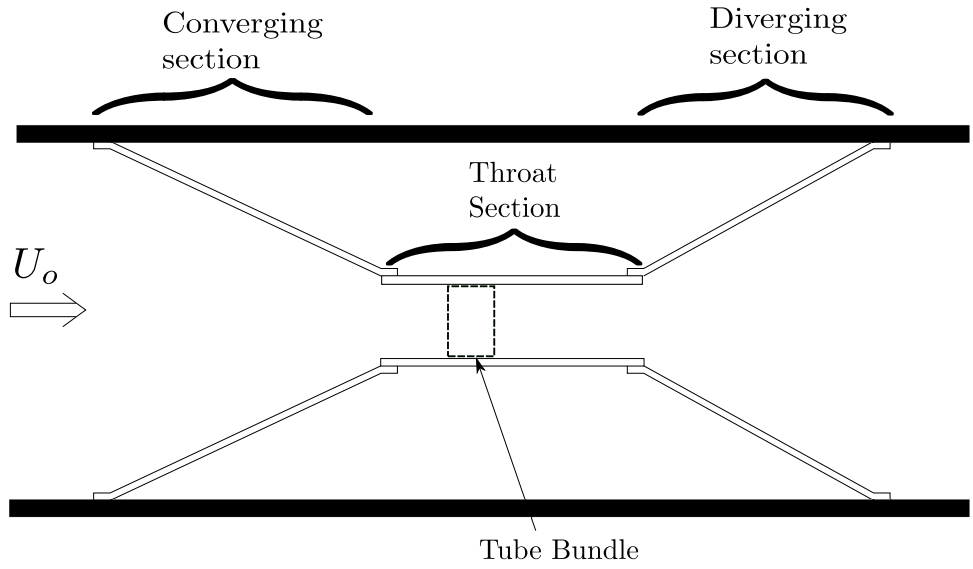

Figure 3.3: Top view of the converging-diverging channel install in water flume's test section.

ratio of 1.35. Figure 3.4, shows the side view of the tube bundle placed 20.4D downstream of the throat's inlet. It consisted of 5 rows and 16 columns.

For this study, it is important to recreate the flow conditions that exists in the periphery area of the industrial heat exchanger right above the tube sheet, since majority of foreign obejcts are found in this region. Similar flow conditions helps in simulating the dynamic forces these foreign objects experience inside tube bundle and study the resulting vibration response. The interstitial flow inside tube bundle changes upto third row of the tube bundle and remain unchanged afterwords [33]. Previous studies have shown that tube bundle with 5 to 6 rows are enough to simulate a tube-bank [34, 87]. In addition, 16 columns are used to minimize the wall effects on the flow behaviour in the central columns (consists of I690 tubes as shown in Figure 3.4b) of the tube bundle where foreign objects were placed [23,88].

The total length of the tubes inside the tube bundle was (33.5D) as shown in Figure 3.4a. A plate was installed 25D from the base of the tube-bundle with the thickness of 1.5D to minimize tube vibration. All core tubes (Figure 3.4b) were made from steal alloy I690 (with thickness (h) of 1 mm), a commonly used material to build steam generator tubes. This material was used to match foreign objects boundary conditions, while the remaining tubes were made from Teflon for economic purposes.

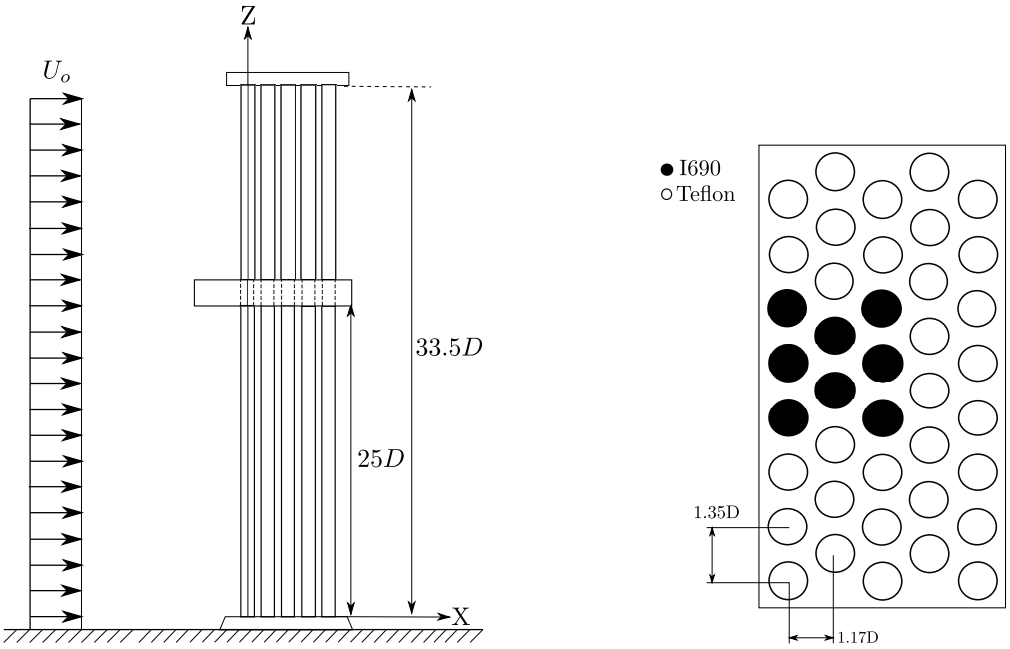

(a) Side View (b) Top View

Figure 3.4: Schematic of tube bundle.

3.2.1 Foreign Objects

Foreign Object Search And Retrieval (FOSAR) activities performed during power plant's outage period provide information about the physical characteristics of the foreign objects. Two common reported object geometries during FOSAR activities are considered: (i) a wire with diameter ($d_w = 1.2mm$) and (ii) a plate with width ($d_p = 4.5mm$) and thickness ($h_p = 0.5mm$) [5, 26, 30]. These objects were shaped into a hook as shown in (Figure 3.5c), characterized by diameter (D_h) and length (L). The hook shaped geometry allows foreign objects to yaw results in a change in (ϕ), pitch results in a change in (θ) and/or pure translation results in a change in (Z) freely inside the tube bundle with minimum constrains. All tested samples had a constant diameter (D_h) of 17.5 mm and a non-dimensional length (L/D) as shown in Table 3.1 based on previous FOSAR activities findings [30].

These test subjects were placed by hand inside the core tubes (made with alloy I690) of the tube bundle while the flume was running, as can be seen in Figure 3.5b. Foreign object's vertical position (Z/D) above the tube sheet, inside the tube bundle is determined based on the flow uniformity upstream of the bundle. The flow uniformity changes after installing the grid at throat section's inlet. In order to minimize the effect of flow non-uniformity on foreign object's response the velocity profiles upstream of the tube bundle were recorded with and without the gird. Based on these results, foreign objects were

Table 3.1: Parameters studied

Fluid Parameters		Geometric Parameters	
(Re_D)	($Tu\%$)	(L/D)	Shape
36,257	2,7.5	2.8, 3.4, 4.0, 4.6	Wire, Plate
42,682	7.5	2.8, 3.4, 4.0, 4.6	Wire, Plate

placed within Z = 216 mm (12.4D) and Z = 256 mm (14.6D) from the ground. The flow uniformity in this area was less than 7% for all experimental runs. These objects were placed at a yaw angle of $\phi = 120^o$ and a pitch angle of $\theta = 90^o$ as shown in Figure 3.5a. Once left inside the bundle, these objects reorient themselves (i.e. change angles (ϕ & θ)) until the object start vibrating about its mean position. The displacement time realization was recorded after leaving the object for two minutes inside tube bundle to reach its mean vibrating position.

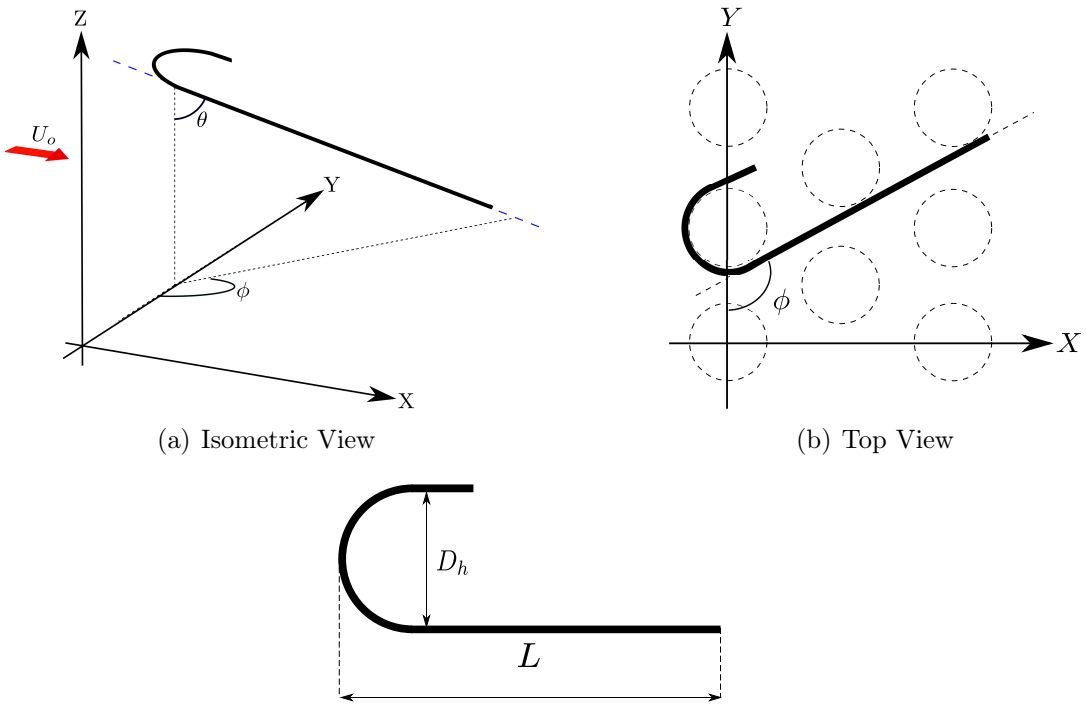

(a) Isometric View

(b) Top View

(c) Dimensions

Figure 3.5: Foreign Object's dimensions and orientation inside tube bundle.

3.3 Measurement Techniques

3.3.1 Flow Characterization

Measurement Science Equipments minLDV system (a dual beam configuration) was used to characterize the flow upstream and inside the tube bundle. The system consists of 140 mW Argon laser, Bragg Cells and detection system. Its dual beam laser creates probe volume with the dimensions of 0.15 x 0.15 x 1.24 mm^3 in X, Y and Z direction, focused at a fixed distance of 400 mm ($22.9D$) from the sensor in air ($\approx$530mm (30.3D) in water). The system was mounted on a three dimensional traverse located on top of the flume's test section. The traverse system Z-direction was calibrated to account for the change in the focal distance as the laser travel distance in air and water changes. The system gives an accuracy in positioning the probe within $\pm 1mm$ ($\pm 0.06D$). The flow was seeded with the neutrally buoyant glass spheres with mean diameter 10 μm.

The miniLDV was used to characterize the incoming flow and collect the data for spectral analysis inside the tube bundle (Appendix A). The measurement upstream of the bundle, discussed in Appendix A, showed that the flow uniformity in the region of interest was within 7% for all experimental runs and turbulence intensity within 7.5%. The Reynodls number and turbulence intensity under which the experiments were performed are tabulated in Table 3.1. The error (calculated in Appendix B) in LDV velocity measurements is estimated to be between 0-3% of the free stream velocity. The error in frequency determination are set by the resolution of the spectra, which is $\pm 0.0001 fD/U_o$.

For the velocity spectra, the data was collected at the average acquisition rate of 100

Hz for 45 minutes. The data obtained was re-sampled at 50 Hz using a sample-and-hold technique proposed by Adrian & Yao [89]. The re-sampled data was partitioned into 16 segments, each consisting of 8192 data points at 0% overlap. The Fast-Fourier transform (FFT) algorithm was applied to compute resulting spectra for each individual segment and then averaged. This yields the velocity spectra resolution of $0.0002fD/U_o$.

3.3.2 Stereo Vision

Two high speed 1024 by 1024 pixels Photron SA4 cameras, equipped with 105mm fixed focal length Nikon lenses were used to extract the instantaneous position of foreign objects, allowing time-resolved characterization of three-dimensional response. Figure 3.6, shows the position of two cameras with respect to the tube bundle. The side camera was positioned outside the flume with its optical axis perpendicular to ZX plane. The top camera was positioned upstream, looking into the tube bundle gap where foreign objects were placed.

Top camera was calibrated using custom made target (dotted array) imaged at different distances from the camera, while the side camera was calibrated using the target placed inside the tube bundle gap. The depth of field for both cameras was 50 mm. Together the cameras were able to resolve the position of the foreign object within 6 cm^3 volume (Measurement volume shown in Figure 3.6) with the resolution of 0.1 $mm/pixel$. Analysis of the images, discussed in Appendix C, allowed unique determination of the three-dimensional position of any point on an imaged object placed within the measurement volume. This method results in determining the X,Y position with the accuracy of $\pm 0.07mm$ and Z

position with the accuracy of $\pm 0.05mm$.

Each foreign object was painted black, and 1 mm wide white markers were drawn on it 1 mm apart. These objects were illuminated using an Nd:YLF laser synchronized with high-speed cameras. For each run a set of 7127 images were recorded at 150 Hz from each camera. The resultant frequency resolution of the displacement spectra is $0.002fD/U_P$. Detailed discussion on the measurement uncertainty is provided in Appendix B.

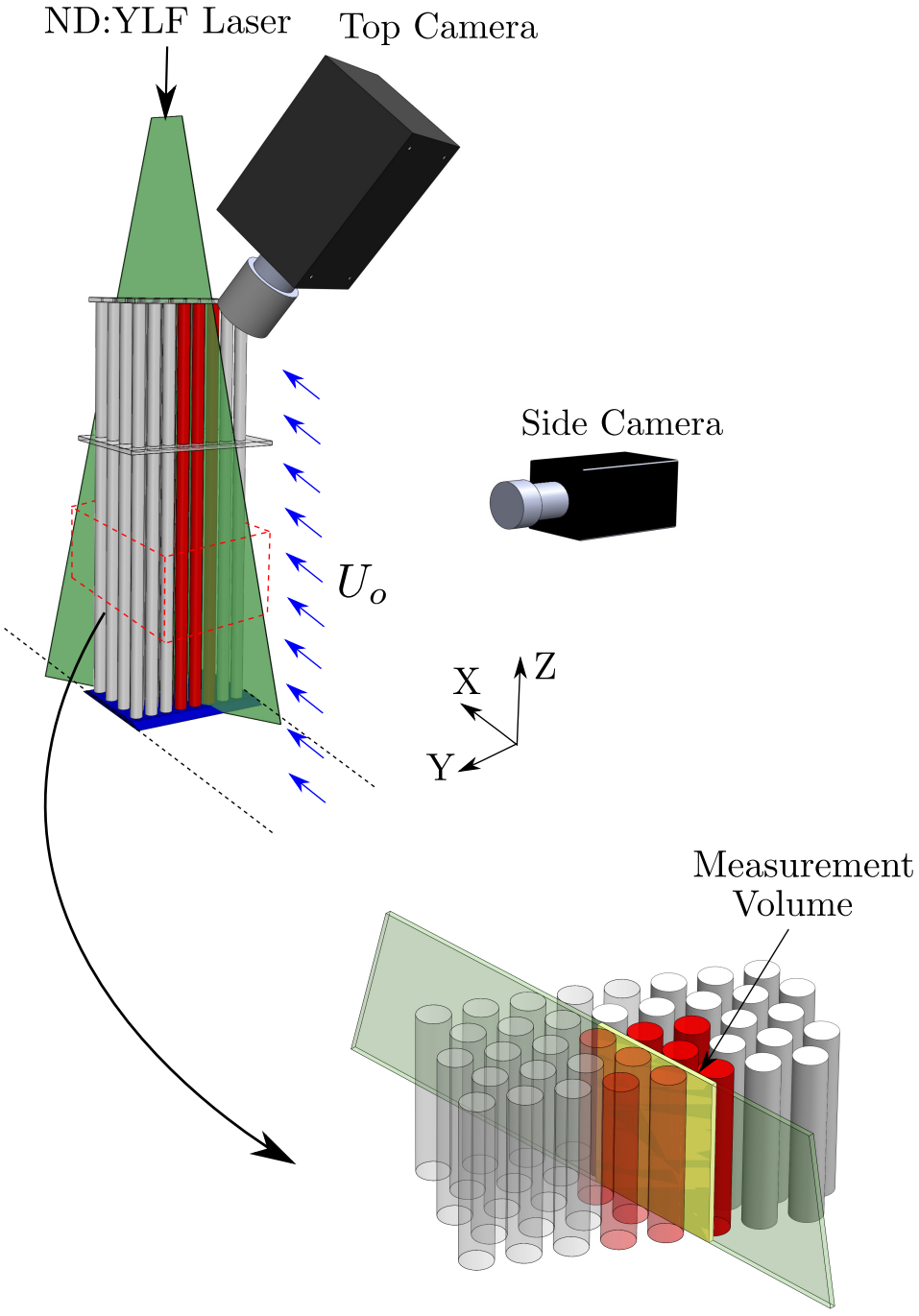

Figure 3.6: Two Camera Setup.

3.4 Wear Analysis

Foreign object vibration inside steam generator's tube bundle is expected to result in wear related tube damage. For steam generator's tubes, the removal of 40% of wall thickness is considered as critical wear [4, 22, 90]. Wear analysis is performed to determine the time required for wear scar to reach critical depth ($H = 0.40h$).

The commonly used wear model that estimates the volume removed (Q) due to sliding contact uses Archard's wear equation [13, 22, 91]:

$$Q = KF_nS_d \tag{3.1}$$

This semi-empirical equation requires wear coefficient (K), normal force (F_n) and sliding distance (S_d) as an input parameters. Since the critical depth($H = 0.4h$) and the critical volume ($Q = q_c$) are known values, the equation (3.1) is modified to determine time (T) required to reach this volume [13, 22, 76]:

$$T = \frac{q_c}{KF_nS_v} \tag{3.2}$$

where, S_v is the sliding velocity. For this analysis, parameter q_c is derived from the geometry of the wear scar, K is obtained from previous empirical studies, F_n is estimated from the experiments and S_v is either directly obtained from the experiments or extrapolated for higher Reynolds number dynamic environment. The methodology used in this section is summarized in Figure 3.7.

Inside steam-generator foreign objects are vibrating randomly against tube bundle's

tube surface. This type of dynamic response is expected to produce a wear scar as can be seen in Figure 3.8. The depth of the wear scar is a function of position Z and time [91]. The section view AA in this figure shows the segment area (shaded region) of the wear scar that has reached critical depth (H). For this study, as shown in Figure 3.9, the total volume removed (Q_T) is divided into smaller segments of volume q_i:

$$Q_T = \sum_{i=1}^{n} q_i \tag{3.3}$$

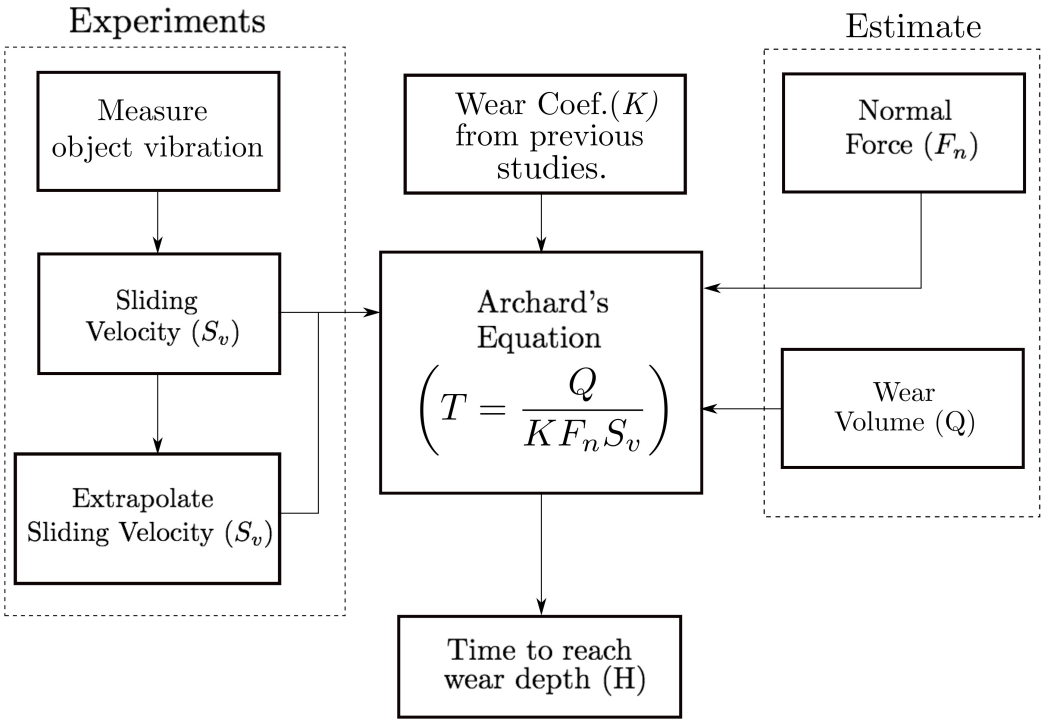

Figure 3.7: Procedure for estimating wear time due to foreign objects related tube wear damage.

where q_i is the volume of the i^{th} segment and n is the total number of segments. Each of these smaller segments experience different sliding velocity due to the random motion of foreign object, as a result, each segment achieve different wear depth for a given amount of wear time. Archard's equation 3.1 can be applied to each of these segments to obtain wear depth for a given amount of wear time. This study is interested in a segment (Marked with red in figure 3.9) that experiences maximum sliding velocity resulting in reaching a critical wear depth (H) in a shortest amount of time (T). Since the wear scar depth associated with this segment is known, the associated volume (q_c) is calculated as follows:

$$q_c = \frac{D^2[2\alpha - sin(2\alpha)]}{8} M \tag{3.4}$$

where M is the width of the segment, D is tube outer diameter and α is a contact angle, obtained as follows:

$$\alpha = cos^{-1}(1 - \frac{2H}{D}) \tag{3.5}$$

As discussed in chapter 2, wear coefficient (K) depends on material pairs in contact, the ambient conditions (temperature and water chemistry) and the wear mode (impact, fretting or sliding) [13, 76, 92]. Previous studies have provided the wear coefficient for sliding type wear mode under various ambient conditions for different material pairs as summarized in Table 3.2. These material pairs selected for current analysis have been used in previous studies to calculate foreign objects related fretting wear [22,26]. Wear coefficient for material pair of I600/304SS and I690/304SS are obtained from Lim et al [80] study since they have obtained this coefficient in water environment, unlike Kim & Lee [85] who obtained wear coefficients for these pair in air environment. For I600/409SS, I600/403SS,

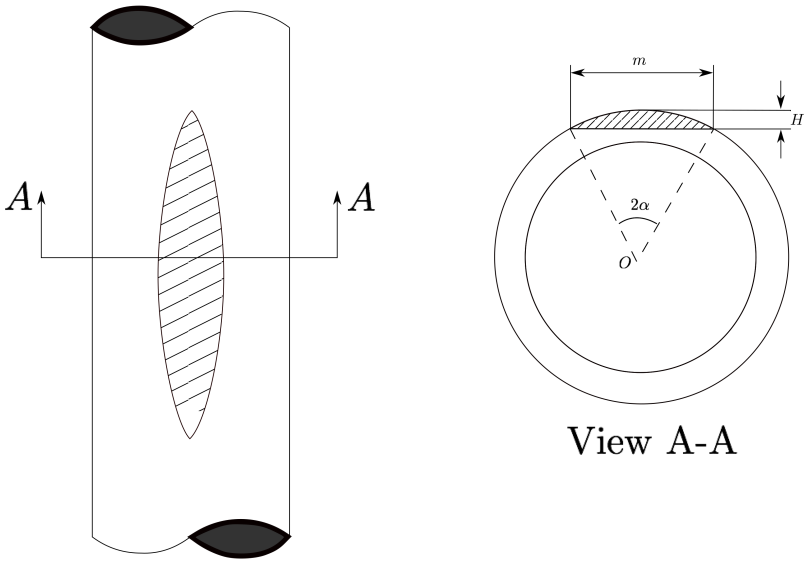

Figure 3.8: Front view of the wear scar.

Table 3.2: Wear coefficients from various studies

Material		Wear Coefficient ($10^{-15} pa^{-1}$)			
Tube	Object	Park et al [84]	Kim & Kim [67]	Kim & Lee [85]	Lim et al [80]
I600	409SS	5.84	57.1	-	-
	403SS	-	72.8	-	-
	304SS	-	-	443.7	98.1
I690	409SS	5.23	-	-	-
	304SS	-	-	366.8	142.7

I600/304SS and I690/409SS material pairs wear coefficients are obtained from Park et al [84], Kim & Kim [67] and Lim et al [80], respectively.

Foreign objects inside the tube bundle experience force perpendicular to its length (L) as shown in Figure 3.10. The normal force (F_N) is calculated as follows:

$$F_N = \frac{1}{2} C_n A_r \rho {U_p}^2 \tag{3.6}$$

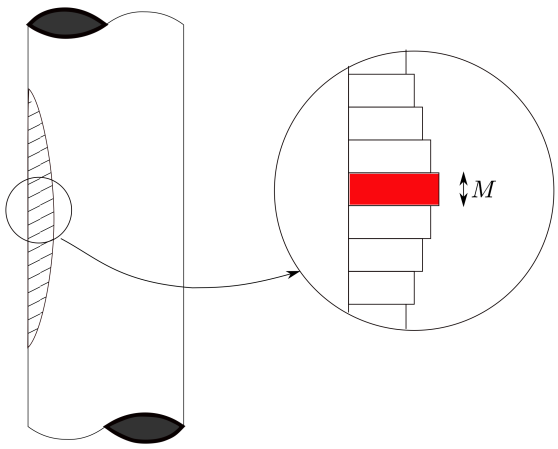

Figure 3.9: Side view of the wear scar.

where C_n is the normal force coefficient, ρ is the density of the water, A_r is the reference area and U_p is the pitch velocity. The pitch velocity is related to the upstream velocity through geometry by the equation [13]:

$$U_p = \frac{(P/D)}{(P/D) - 1} U_o \tag{3.7}$$

The fluid density is assumed to be approximately constant over the length of the foreign object typically confined to the first few rows, with significant heat transfer effects in the bulk of the fluid expected primarily in the inner rows. Furthermore, for the vibration amplitude much smaller than the length of foreign objects, which is the case in the previous study, the angle between U_p and foreign object does not vary appreciably along the length

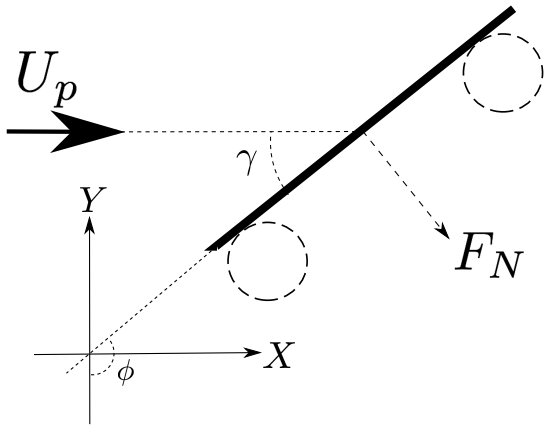

Figure 3.10: Yawed foreign object inside tube bundle.

of the object. Thus, for the foreign object geometries considered here, the foreign object is yawed bluff body in cross flow of velocity U_p. From previous empirical studies, the normal force coefficient of 0.3 for yawed cylinder and 0.8 for yawed flat plate is obtained [14,93–97]. The normal force (F_n) acting on volume q_c is obtained as follows:

$$F_n = \frac{F_N}{e} \tag{3.8}$$

where, e is the number of tubes in contact with the foreign object.

The sliding distance experienced by tube surface point of the i^{th} segment experiencing critical wear can be expressed as follows:

$$S_d = S_v * t \tag{3.9}$$

where S_v is sliding velocity and t represents wear time. The sliding velocity is estimated

directly from the displacement time realization recorded during the experiments, conducted at pitch velocity of 2 m/s and 2.5 m/s (see Appendix D) [91, 98]. Sliding velocity for higher pitch velocities is estimated by extrapolation the foreign object response, as shown in Appendix E.

Overall, the critical volume removed obtained from equation 3.4 with its respective normal force and sliding distance obtained from equation 3.8 and 3.9 are plugged into equation 3.1 to obtained modified Archard's equation 3.2. By using empirically obtained wear coefficient from previous studies, this modified Archard's equation provides the wear time (T) needed to reach known wear depth H shown in Figure 3.7.

Chapter 4

Results

This chapter presents the results of foreign object's flow induced vibration experiments and corresponding wear analysis. First, the type of vibration and characteristics of vibration respone recorded experimently are presented in Section 4.1.1. Section 4.1.2, provides insight into three dimensional kinematics of foreign object inside tube bundle. Results highlighting the effects of non-dimensional length (L/D), Reynolds number (Re_D), turbulence intensity (Tu) and geometry on the dynamic response are illustrated in Section 4.1.3. Finally, Section 4.2 presents the wear of steam generator tubes caused by the vibration of foreign objects inside tube bundle.

4.1 Foreign Object Dynamics

Figure 4.1 shows the three dimensional configuration of a hook-shaped foreign object placed inside tube bundle. These objects have two axis of rotation inside a tube bundle, i.e. axis

B_c and axis B_o shown in Figure 4.1b. Here, axis B_c is the central axis of the tube around which the hook of foreign object is placed and axis B_o is defined as an axis which is tangent to the hook and perpendicular to axis B_r (where, B_r is central axis of the longer leg of foreign object). As discussed in Appendix F, these foreign objects undergo rigid body dynamic; therefore, the overall motion can be obtained from measuring the three dimensional motion of any two points on foreign object. The quantitative analysis of the X, Y and Z displacement time realizations of a reference point p on foreign object is done to characterize the vibration response. The reference point p is located at shortest distance(P_D) away from axis B_o (Figure 4.1b) for all the objects. The statistical tools employed for the analysis of vibration response are discussed in Appendix G.

Hooked shape geometry of foreign object in conjunction with its configuration inside tube bundle allows translation motion in Z direction, yaw motion about axis B_c, and pitching motion about axis B_o, while restricting pure linear motion in X and Y direction and rolling motion (about axis that is parallel to axis B_r and passes thorough point p_o). Figure 4.2a shows the object undergoing pure translation motion in Z direction. For such a motion, the whole body of object remains parallel to its original orientation i.e. each point on foreign object undergoes same amount of displacement in Z direction [99]. For object undergoing pure yaw motion, the change in angle ϕ from ϕ_1 to ϕ_2 is experienced by the object, as shown in Figure 4.2b, resulting in a change in X and Y coordinates of point p. For pure pivoting motion shown in Figure 4.2c, the foreign object experiences a change in orientation due to the change in angle θ from θ_1 to θ_2, resulting in a change in X, Y and Z coordinates of point p.

The response amplitude in Z direction is a combination of pure translation motion

(shown in Figure 4.2a) and pitching motion (shown in Figure 4.2c), and can be expressed as $A'_Z = RMS(p_{Translation} + p_D cos(\theta))$. Whereas the response amplitude in X and Y, which contains the contrition of yaw motion (ϕ) shown in Figure 4.2b and pitching motion (θ) shown in Figure 4.2c, can be expressed as $A'_X = RMS(p_D sin(\theta)(-cos(\phi)) + f(\phi))$ and $A'_Y = RMS(p_D sin(\theta) sin(\phi) + g(\phi))$, respectively. Here, $f(\phi)$ and $g(\phi)$ represent the X and Y coordinates of point p_r (Figure 4.1) as a function of yaw angle.

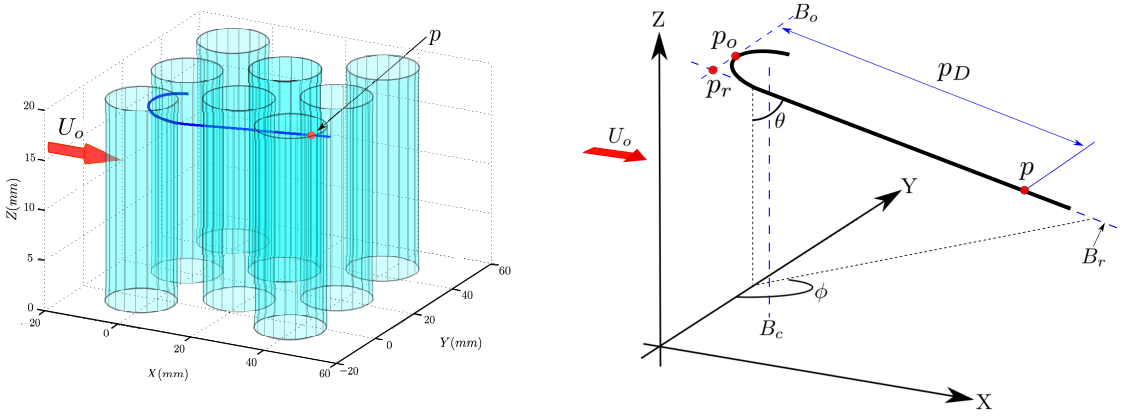

(a) (b)

Figure 4.1: Foreign object inside tube bundle (a) Three dimensional view (b) Schematic of foreign object.

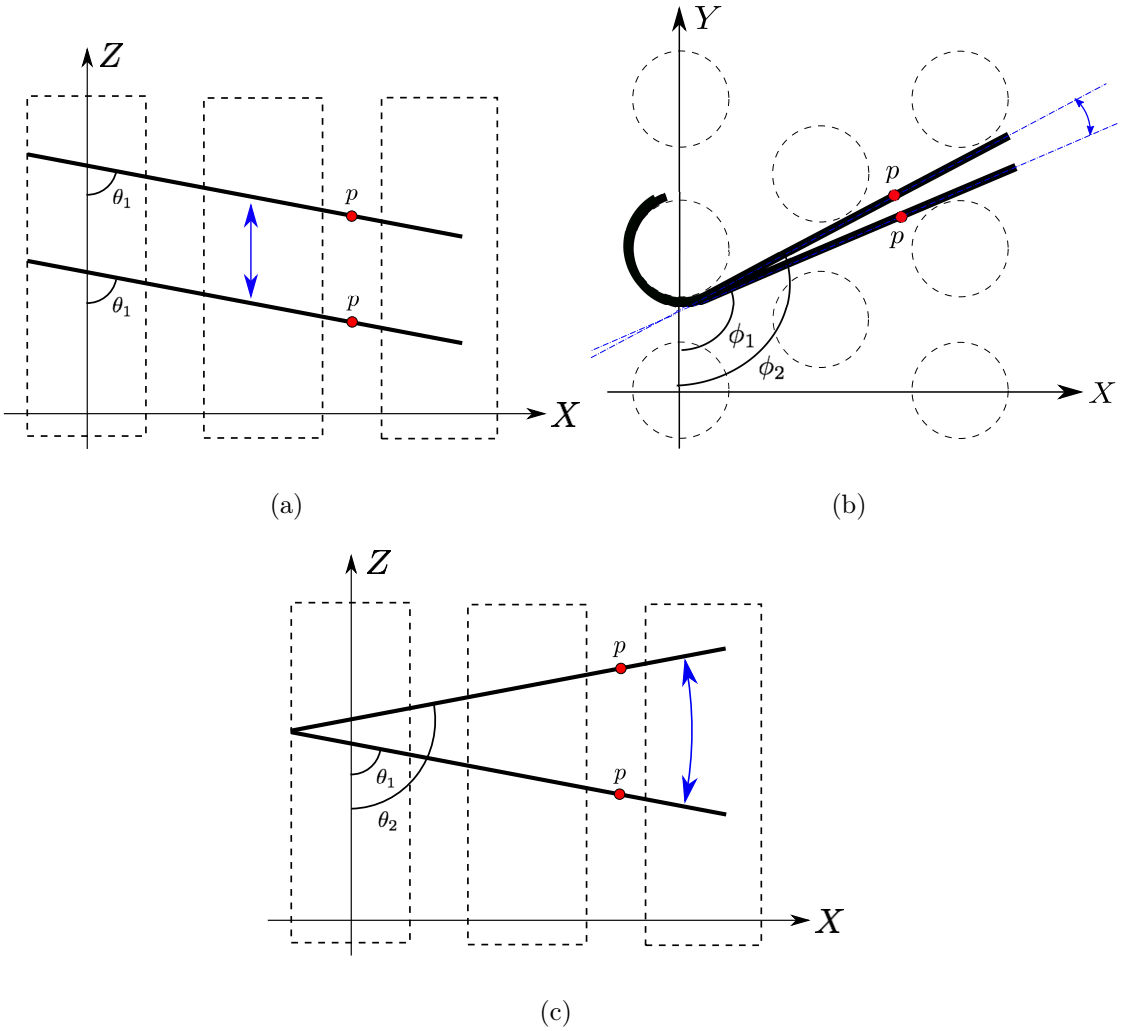

Figure 4.2: Foreign object undergoing rigid body motion (a) Pure translation motion (b) Pure yaw motion and (c) Pure pitching motion.

4.1.1 Motion Characteristics

From the visual inspection of recorded time realizations (shown in Appendix H), the vibration of foreign objects appears to be non-periodic. Since the approach to analyse deterministic and non-deterministic vibrations is different, it is important to first identify the type of vibrtaions encountered by the foreign object [100]. As the first step, autocorrelation and power spectral density of the amplitude response can be considered [100]. Figures 4.3 and 4.4 show the autocorrelation of wire and plate sample responses for length $L/D = 4$, $Tu = 2\%$ and $Re_D = 36,257$, and $Tu = 7.5\%$ and $Re_D = 42,682$, respectively. For pure white noise type random signal, the autocorrelation function will look like infinity narrow impulse function around $\tau = 0$ [101]. A similar type of result is observed in Figure 4.3 and 4.4, featuring a sharp peak at $\tau = 0$ indicative of random vibration response. The autocorrelation differs from ideal impulse function because of the fact that foreign objects undergoes frequency limited random vibration, unlike vibration represneted by pure white noise signal. The rapidly diminishing autocorrelation function indicates wider band random signal as can be seen in Figure 4.3 and 4.4a, whereas a slowly diminishing autocorrelation function as seen in Figure 4.4b, represents random vibration with narrower frequency band [59, 101]. In other words, as the frequency band becomes narrower, the rate at which the signal can change form its current value becomes more limited resulting is some correlation [101].

The normalized power spectral density (PSD) of wire and plate samples are shown in Figure 4.5 and 4.6, for $Tu = 2\%$ and $Re_D = 36,257$, and $Tu = 7.5\%$ and $Re_D = 42,682$, respectively. The absence of distinct spectral peaks in the results suggests no strong

periodic content is present in the response of foreign objects. The spectral results also confirm uneven distribution of the energy across frequencies, with higher energy content observed at low frequencies similar to turbulence energy spectra [102]. The results indicate that samples are vibrating randomly, and statistical tools used to analyze random vibration will be employed to further characterize foreign object dynamic response inside tube bundle.

Having established the random nature of foreign object displacement response inside tube bundle, next step is checking for stationarity. This is important because many data reduction procedures are only applicable to stationary processes [100]. Moreover, assumptions about foreign object statistical properties, like mean, rms amplitude, kurtosis, etc., being time invariant are only applicable if the response is stationary. A practical test for stationarity can be performed by plotting the running mean and rms of the amplitude response [103]. Figure 4.7 and 4.8 shows the running mean and rms of Z displacement of wire and plate type foreign objects with length $L/D = 4.0$. Theses plots show the convergence of the mean and rms value for both wire and plate samples within the length of the aquired displacement signal. Similar convergence of mean and rms was observed for all samples that showed measurable response (Appendix I). The absence of any monotonic or fluctuating trends in these graphs indicates the converged mean and rms values are independent of time, hence indicating the vibration response being weakly stationary. To further validate this conclusion, a reverse arrangement hypothesis test, described in Appendix J, was conduced on all the recorded time realizations [100]. The test results confirmed the random vibration response of foreign objects to be stationary.

Probability Density Function (PDF) of the amplitude response helps draw certain conclusions about the physical phenomena, and is of interest for wear analysis by indicating

where the most significant wear is expected on the tube, expected size of the wear scar, etc. Figures 4.9 and 4.10 show the PDF of wire and plate sample amplitude response for $Tu = 2\%$ and $Re_D = 36,257$, and $Tu = 7.5\%$ and $Re_D = 42,682$, respectively. Also, normal fit to the data are shown in Figures 4.9 and 4.10 with dashed lines for comparision. Notable deviations are observed between the response PDFs and the normal PDFs. Usually, the deviation from normality is either related to the non-linearity introduced by the vibration measuring instruments, non-Gaussian forcing function, and/or non-linearities introduced through the system transfer function [104]. In the present study, the displacement measurements are performed directly based on the images of the samples obtained with two cameras, which does not introduce any non-linearity, identifying the forcing function as the likely source of the observed trend.

Turbulent flow environment which results in random dynamic pressure loading on foreign object surface acts as a forcing function. At the lower turbulence intensity, the wire and plate sample shows near Gaussian distribution as can be seen in Figure 4.9a and 4.10a. In contrast, at the higher turbulence intensity investigated, the non-symmetry in the amplitude distribution about mean increases (Figure 4.9b and 4.10b). This deviation from normality with increasing turbulence intensity can be better understood by plotting Quantile-Quantile (QQ) plots, which for normal distribution should result in a straight line. Figures 4.11a, 4.11b, and 4.11c show the QQ plots of the wire sample for length $L/D = 4.0$, at $Tu = 2\%$ and $Re_D = 36,257$, $Tu = 7.5\%$ and $Re_D = 36,257$, and $Tu = 7.5\%$ and $Re_D = 42,682$, respectively. Figure 4.11a confirms that, at the lower Turbulence intensity investigated, the deviation from normal distribution is relatively minor. At $Tu = 7.5\%$ and $Re_D = 36,257$ the QQ plot (Figure 4.11b) becomes more scattered signifying larger

deviation of vibrating system PDF from normal distribution. While keeping the turbulence intensity the same at $Tu = 7.5\%$, increasing the Reynolds number produces an amplitude response which more closely follows the normal distribution (Figure 4.11c). In these QQ plots, the vibrating system arrangement remains the same in all the test cases considered, suggesting that the observed variations in amplitude response distributions are attributed to the changes in forcing functions caused by the changes in flow parameters. Based on the discussed results, the amplitude response of a foreign object vibrating inside tube bundle can be classified as a stationary, random process which tends to deviates from normal distribution at higher turbulence intensity and low Reynolds number flow environment.

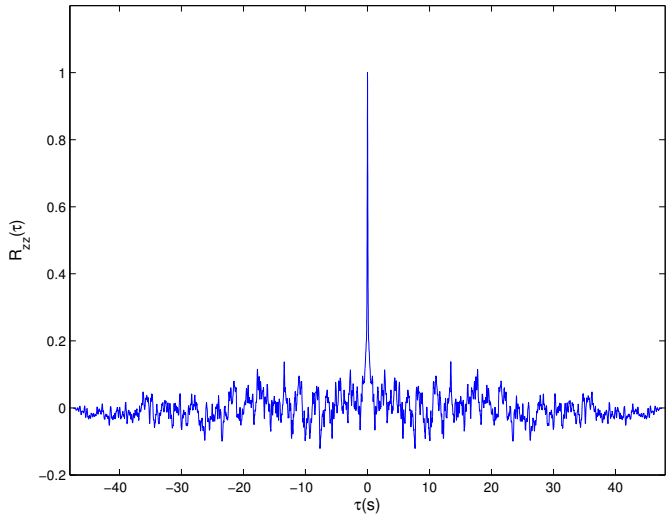

(a) Wire

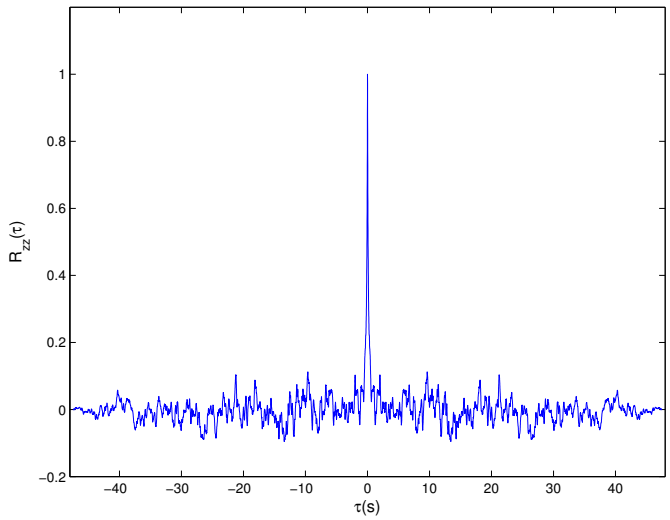

(b) Plate

Figure 4.3: Autocorrelation of Z displacement time realization from foreign object with $L/D = 4.0$ at $Tu = 2\%$ and $Re_D = 36,257$.

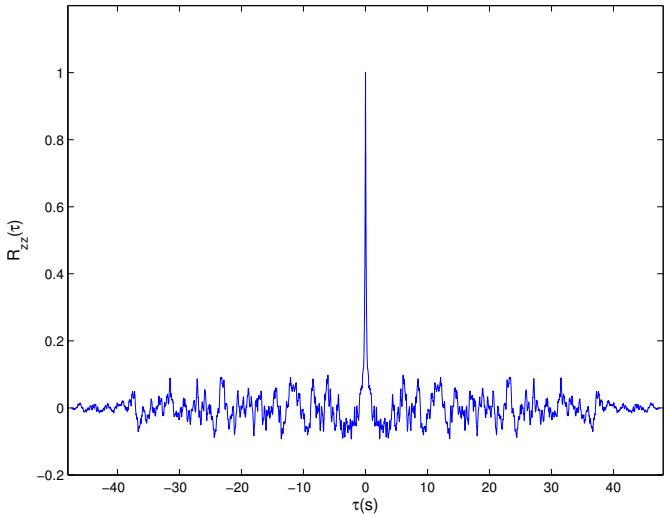

(a) Wire

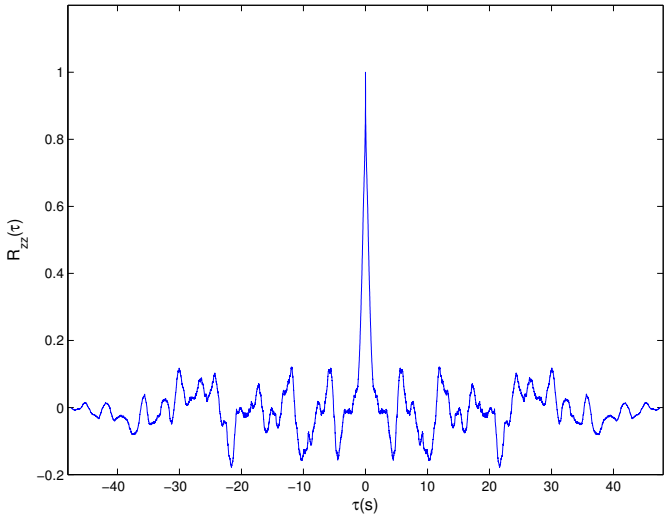

(b) Plate

Figure 4.4: Autocorrelation of Z displacement time realization from foreign object with $L/D = 4.0$ at $Tu = 7.5\%$ and $Re_D = 42,682$.

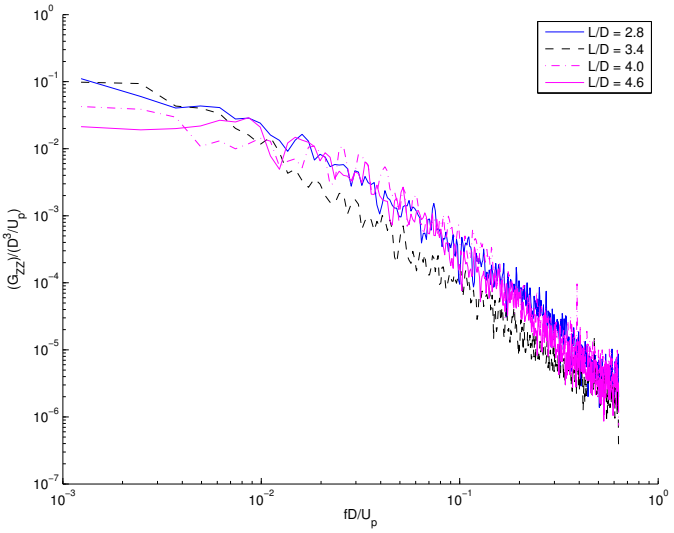

(a) Wire

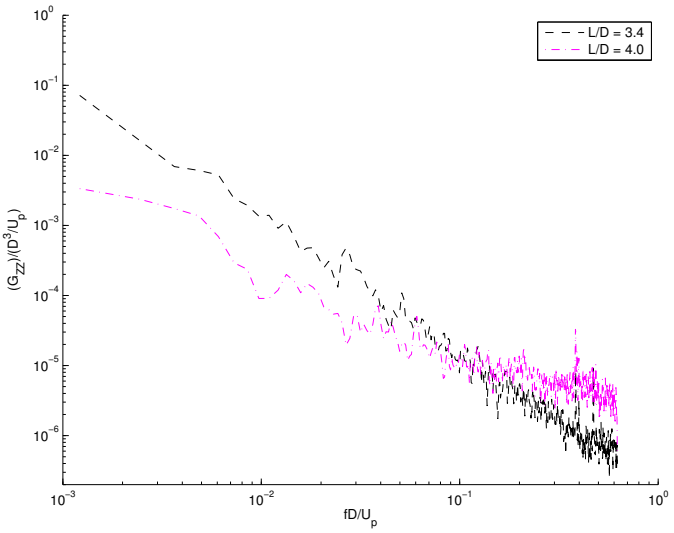

(b) Plate

Figure 4.5: Displacement power spectral density of foreign object at $Tu = 2.0\%$ and $Re_D = 36,257$.

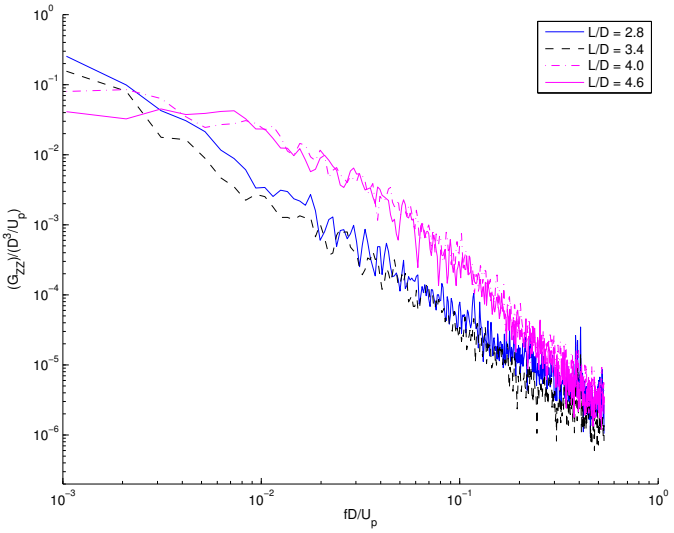

(a) Wire

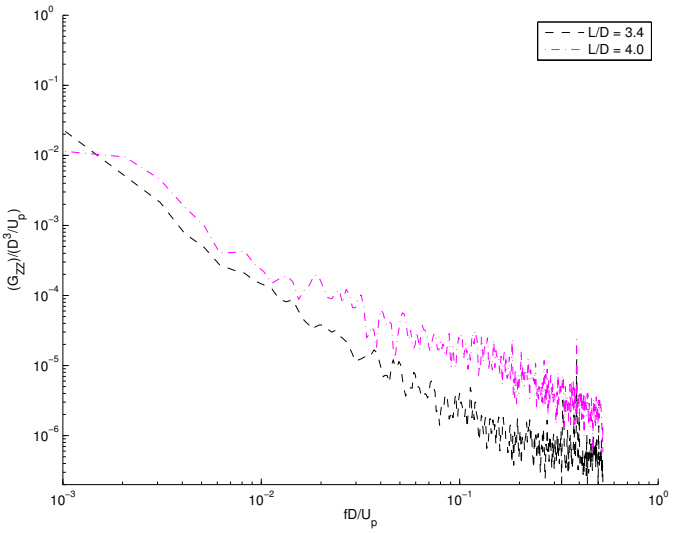

(b) Plate

Figure 4.6: Displacement power spectral density of foreign object at $Tu = 7.5\%$ and $Re_D = 42,682$.

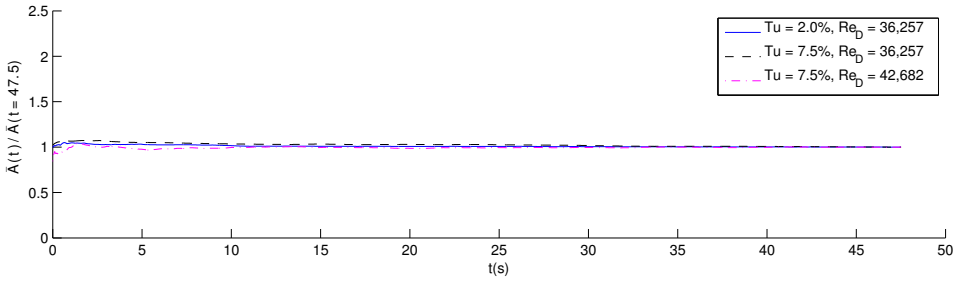

(a) Mean

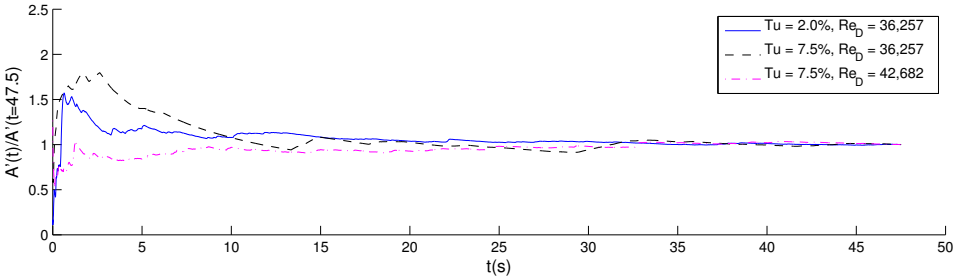

(b) RMS

Figure 4.7: Running Mean and RMS of Z displacement time realization from wire samples with $L/D = 4.0$.

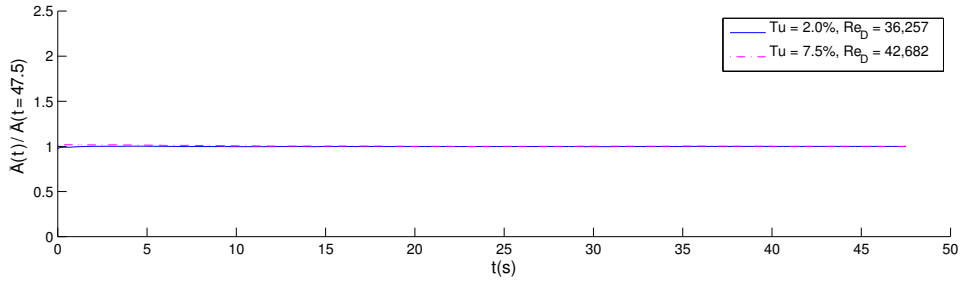

(a) Mean

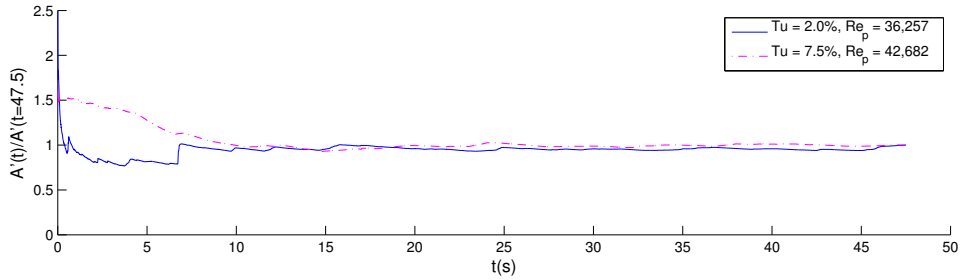

(b) RMS

Figure 4.8: Running Mean and RMS of Z displacement time realization from plate samples with $L/D = 4.0$.

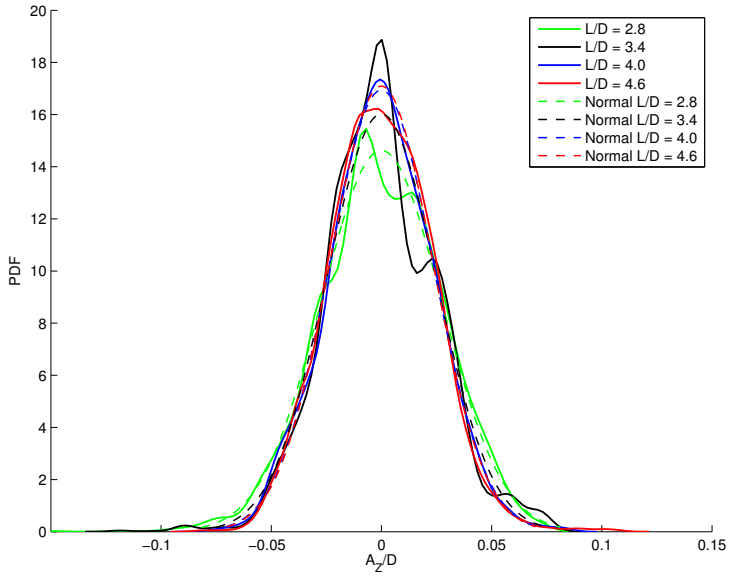

(a)

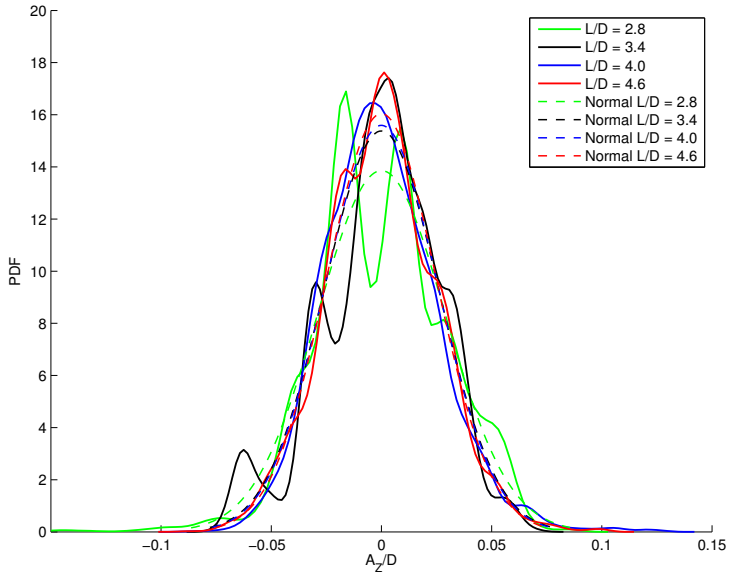

(b)

Figure 4.9: Probability Density Function of wire sample Z response recorded at (a) $Tu = 2.0\%$ and $Re_D = 36,257$ (b) $Tu = 7.5\%$ and $Re_D = 42,682$.

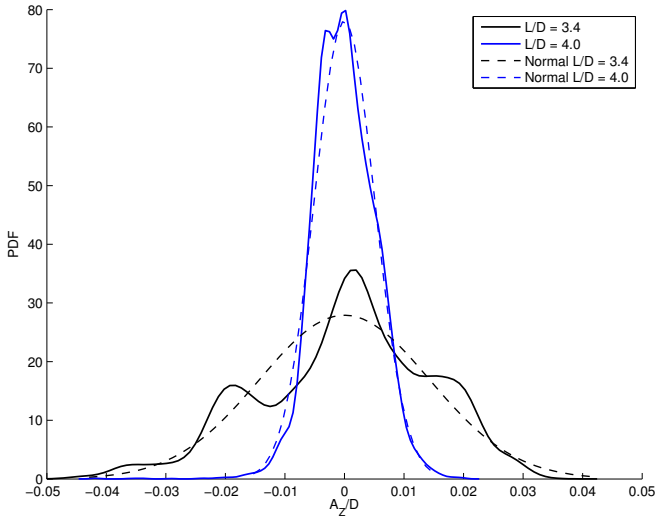

(a)

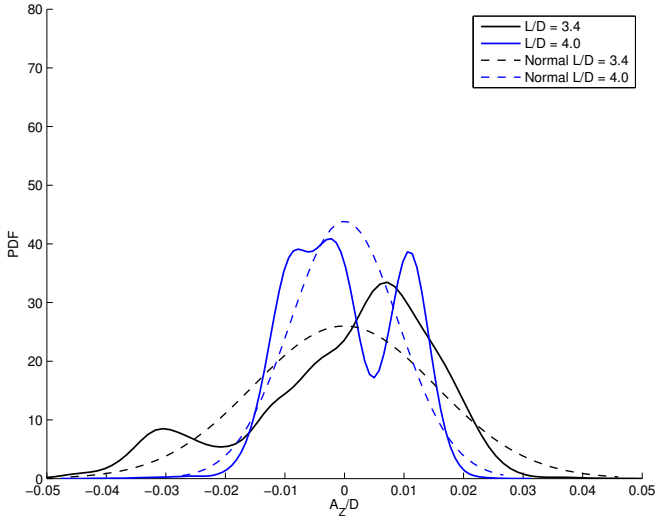

(b)

Figure 4.10: Probability Density Function of plate sample Z response recorded at (a) $Tu = 2.0\%$ and $Re_D = 36,257$ (b) $Tu = 7.5\%$ and $Re_D = 42,682$.

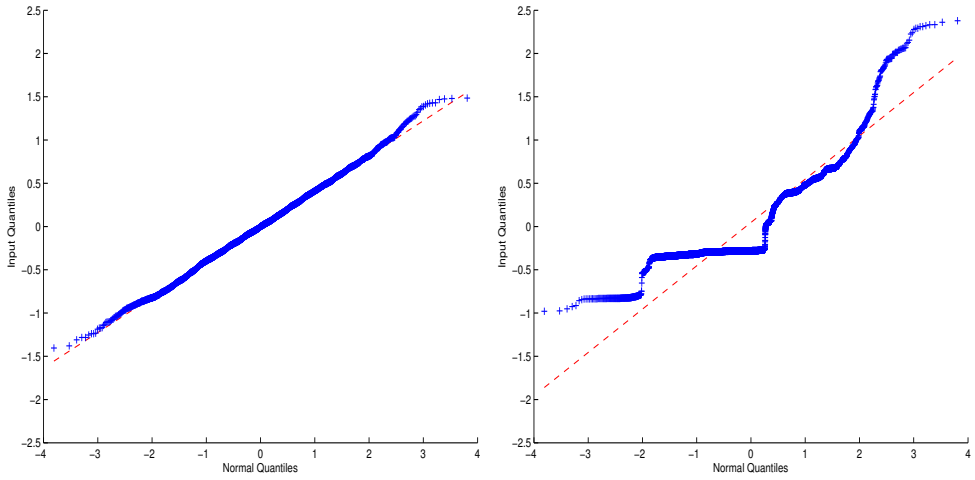

(a) (b)

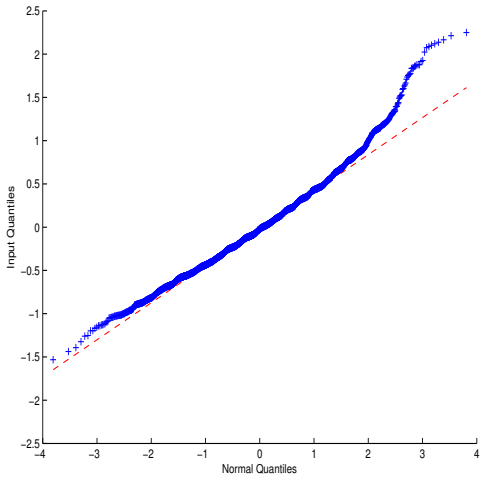

(c)

Figure 4.11: QQ plot of Z response from wire sample with $L/D = 4.0$ at (a) $Tu = 2.0\%$ and $Re_D = 36,257$ (b) $Tu = 7.5\%$ and $Re_D = 36,257$ (c) $Tu = 7.5\%$ and $Re_D = 42,682$.

4.1.2 Foreign Object Kinematics

All foreign objects are placed inside tube-bundle in a shape of a hook with orientation shown in Figure 4.1. Since foreign object can undergo translation motion, pitching motion and yaw motion, this gives the freedom for dynamic interaction between foreign object and tube bundle tubes to be of pure impact type, pure sliding type, or the combination of two. The type of dynamic interaction is determined from foreign object kinematics, and it will help determine the type of wear i.e. impact, sliding, fretting, impact sliding, etc., tube bundle tubes will experience.

Figures 4.12, 4.13, and 4.14 present the normalized rms amplitude recorded at point p on a foreign object. The results demonstrates that the response of the foreign object recorded in Z direction is significantly larger than the response in X and Y. The results for the wire-type objects in Figures 4.12a, 4.13a, and 4.14a shows that all wire samples vibrate inside tube bundle at all the investigated fluid parameters. In contrast, as can be seen in Figures 4.12b, 4.13b, and 4.14b, not all investigated plate samples show measurable vibration response. Specifically, the plate sample with L/D = 2.8 does not exhibit any substantial amplitude response. In addition, plate samples with L/D = 4.6 for $Tu = 2\%$ and $Re_D = 36,257$, $Tu = 7.5\%$ and $Re_D = 36,257$, and $Tu = 7.5\%$ and $Re_D = 42,682$ and L/D = 4.0 for $Tu = 7.5\%$ and $Re_D = 36,257$, do not stay within the measurement volume and sink to the tube-sheet; therefore, they are omitted from the plots.

As discussed at the introduction of Section 4.1, motion measured in Z direction (A'_Z) is a combination of pure translation and pitching, whereas the motion in X direction (A'_X) and Y direction (A'_Y), is due to pitching and yawing. Out of the three types of

motions that foreign object undergoes in this study, only the yaw (change in ϕ) leads to impact type surface interaction between foreign objects and tube bundle tubes. Large yaw motion would result in large difference between A'_X and A'_Y values, since the contribution of pitching motion (change in θ) is the same to these two components. The results shows no significant difference between A'_X and A'_Y which leads to the conclusion that contribution of yaw components to the overall motion is negligible. This is confirmed in Figures 4.15, 4.16, and 4.17 which present the RMS yaw angle for foreign object at $Tu = 2\%$ and $Re_D = 36,257$, $Tu = 7.5\%$ and $Re_D = 36,257$, and $Tu = 7.5\%$ and $Re_D = 42,682$, respectively. For all the cases examined the rms yaw angle is around 0.15 degrees. Thus, it can be concluded that the foreign object motion can be approximated as of planar type in the Z direction along the axis of the tube bundle tubes. Thus, the interaction between the foreign objects and the tubes is expected to be a sliding type surface interaction. Therefore, the analysis will henceforth focus on the amplitude response in Z direction.

The general planar response of the foreign object is composed of simultaneous translation in Z direction and rotation due to pitiching motion about axis B_o (Figure 4.1). For a rigid object that undergoes rotational motion, all the points on the foreign object except the points lying on the axis of rotaion should experience displacement due to rotation [99]. For a hooked shape object undergoing pitching motion, due to geometric constrains, only point p_o on the foreign object cannot experience displacement due to rotational motion and can only slide linearly against the tube surface. Hence, point p_o which only experiencing pure translation motion is the pivot point, while all other points on the foreign object experience a combination of pure translation and pitching motion. Figures 4.18, 4.19, and 4.20 presents the planar motion decomposition of point p into its linear and angular com-

ponents. In these plots, the linear rms amplitude represent the pure translation component of the overall motion of point p (which is same as overall motion of pivot point p_o), and the angular rms amplitude represents the angular contribution to the overall planar motion as a result of rotation of point p about axis B_o. These figures show that both wire and plate type foreign objects undergoes a combination of linear and angular motion. Figures 4.18a, 4.19, and 4.20a shows that the rms amplitude of the pivot point p_o (i.e. linear component of point p motion) is on the average about 40 to 70 percent of the rms amplitude of point p. Similar results are observed for plate samples of length L/D = 3.4 and 4.0 as shown in Figures 4.18b and 4.20b.

Based on the results presented in this section, it can be concluded that all wire samples vibrate inside tube bundle, whereas only plate samples of length L/D = 3.4 and L/D = 4.0 show a significant amplitude response. In addition, all foreign objects experience negligible contribution of yaw component and undergoes pure planar motion. This means that tube bundle tubes will experience sliding type dynamic interaction due to foreign object vibration and not pure impact or impact and sliding type interaction. Finally all vibrating foreign objects undergoes a planar motion with significant contribution from both pure translation and pitching component.

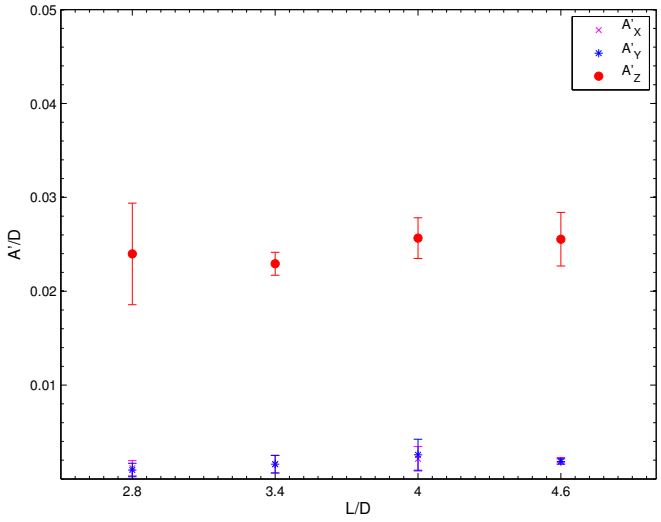

(a) Wire

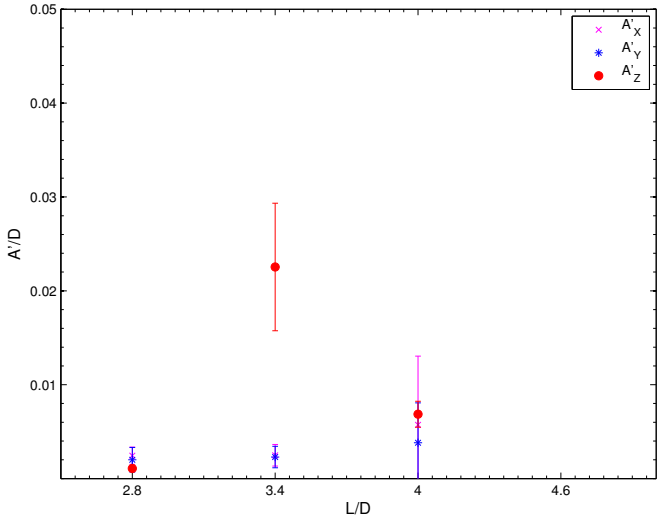

(b) Plate

Figure 4.12: Normalized RMS amplitude of point p of the foreign objects, at $Tu = 2\%$ and $Re_D = 36,257$.

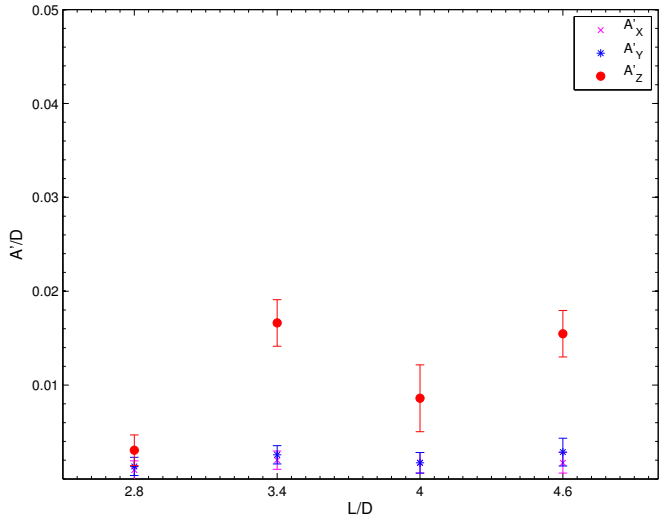

(a) Wire

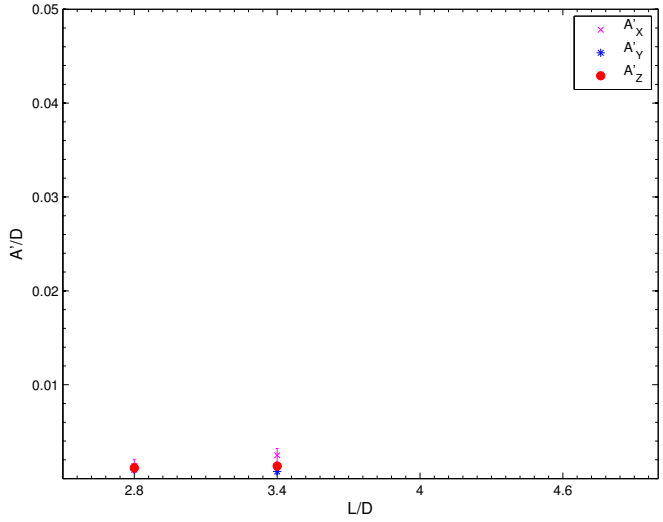

(b) Plate

Figure 4.13: Normalized RMS amplitude of point p of the foreign objects, at $Tu = 7.5\%$ and $Re_D = 36,257$.

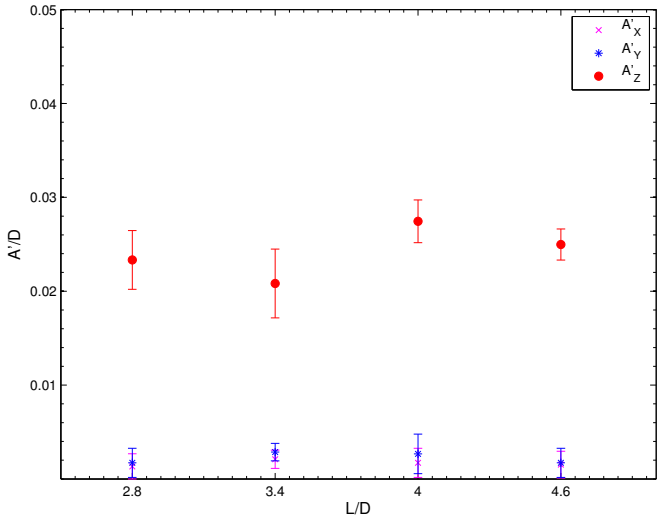

(a) Wire

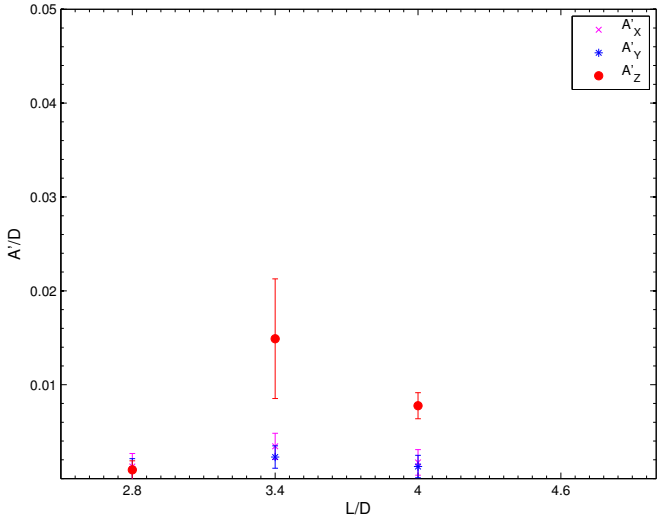

(b) Plate

Figure 4.14: Normalized RMS amplitude of point p of the foreign objects, at $Tu = 7.5\%$ and $Re_D = 42,682$.

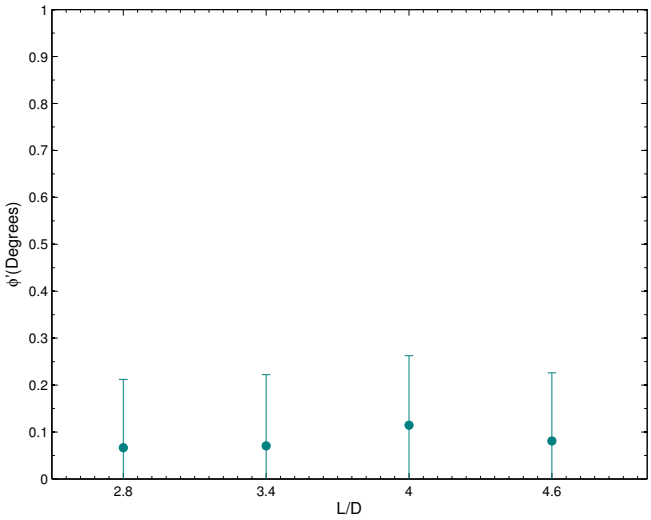

(a) Wire

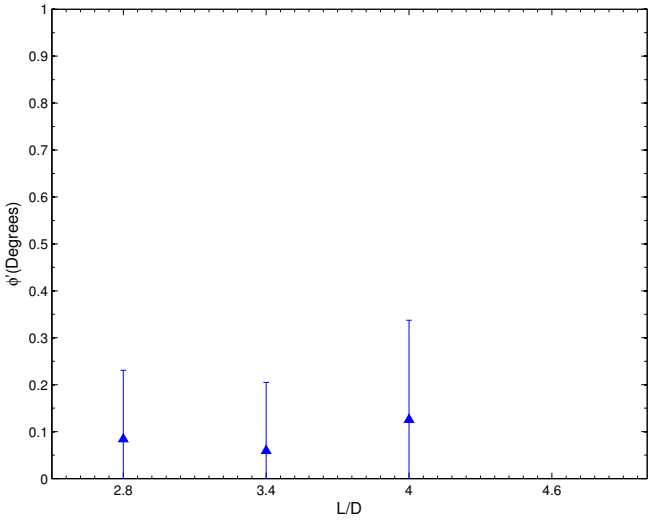

(b) Plate

Figure 4.15: RMS of foreign object yaw angle, at $Tu = 2\%$ and $Re_D = 36,257$.

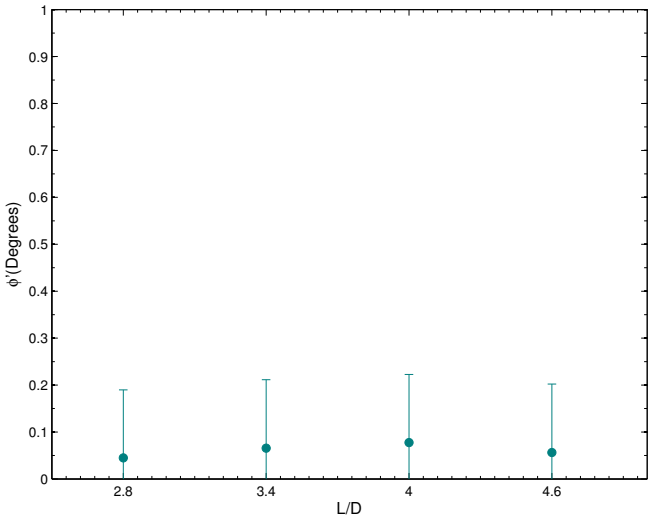

(a) Wire

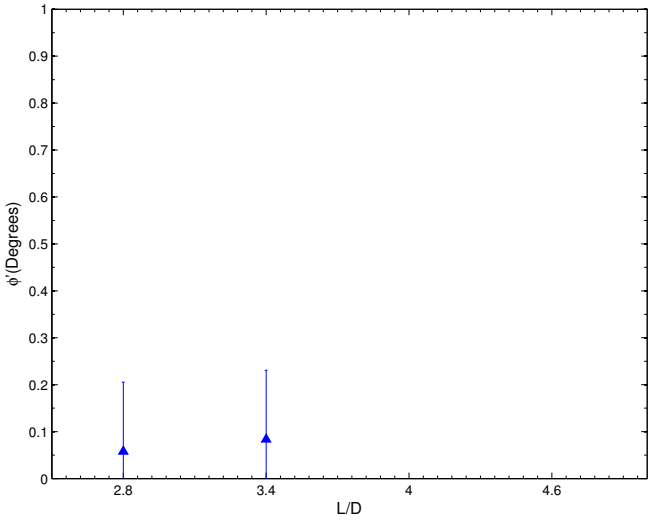

(b) Plate

Figure 4.16: RMS of foreign object yaw angle, at $Tu = 7.5\%$ and $Re_D = 36,257$.

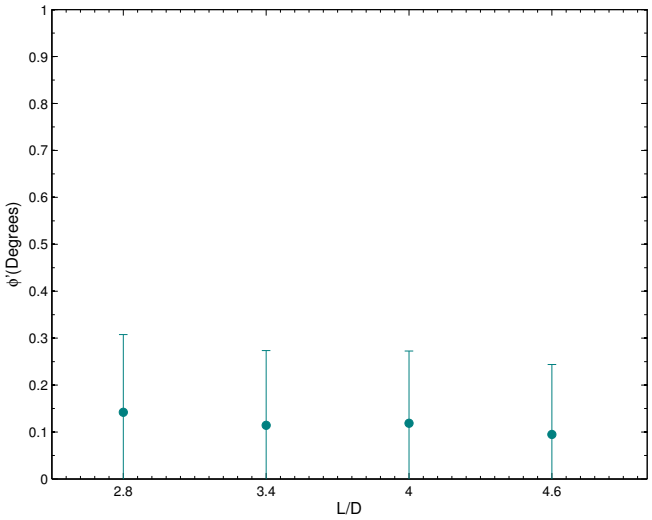

(a) Wire

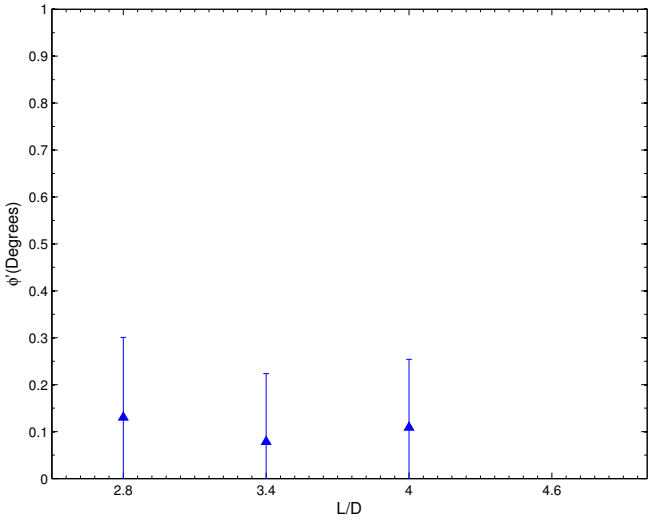

(b) Plate

Figure 4.17: RMS of foreign object yaw angle, at $Tu = 7.5\%$ and $Re_D = 42,682$.

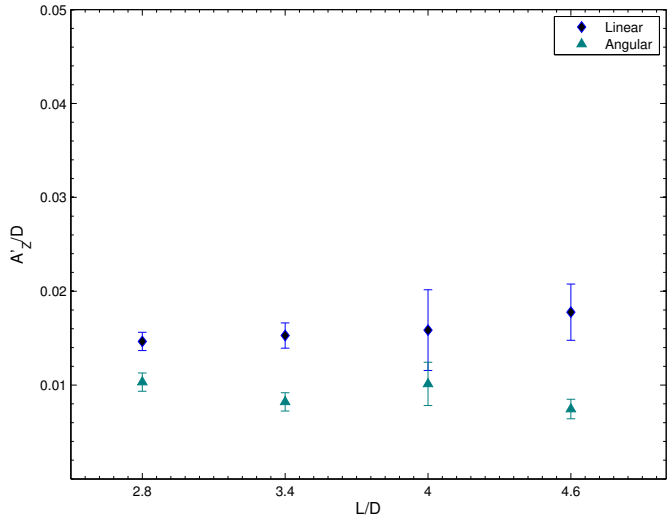

(a) Wire

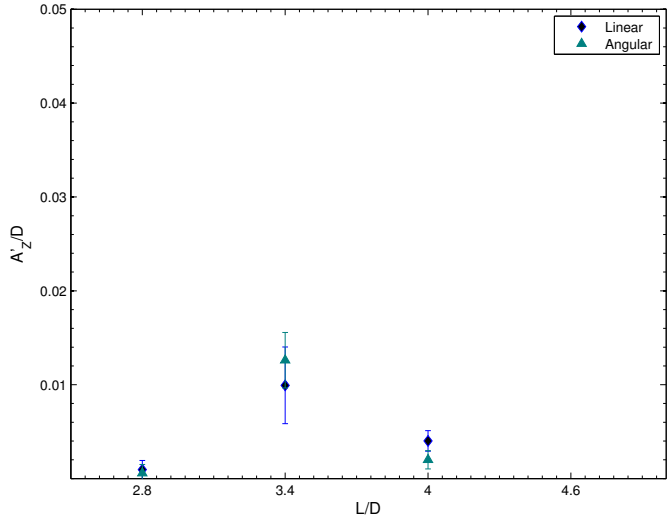

(b) Plate

Figure 4.18: Normalized linear and angular RMS amplitude of point p of the foreign object, at $Tu = 2\%$ and $Re_D = 36,257$.

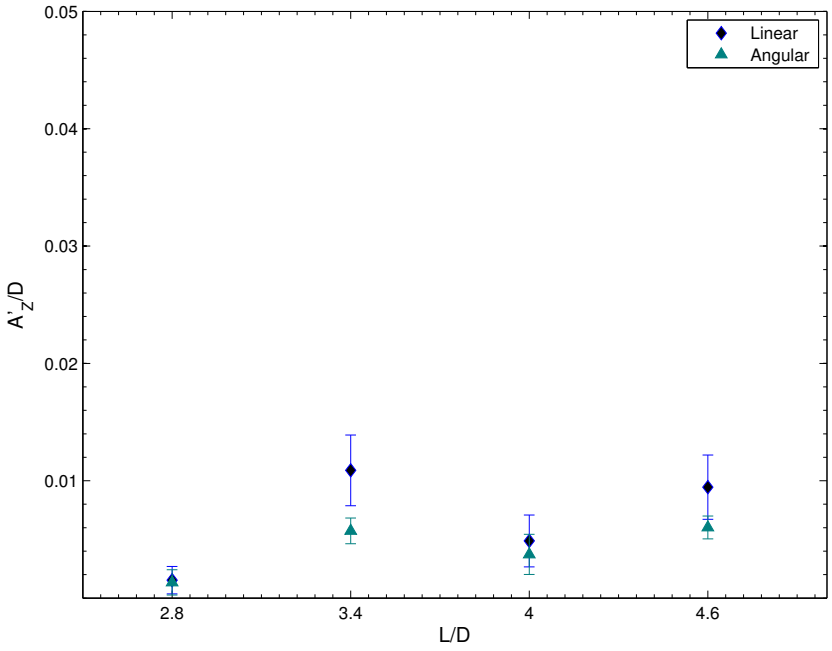

Figure 4.19: Normalized linear and angular RMS amplitude of point p of the foreign object, at $Tu = 7.5\%$ and $Re_D = 36,257$.

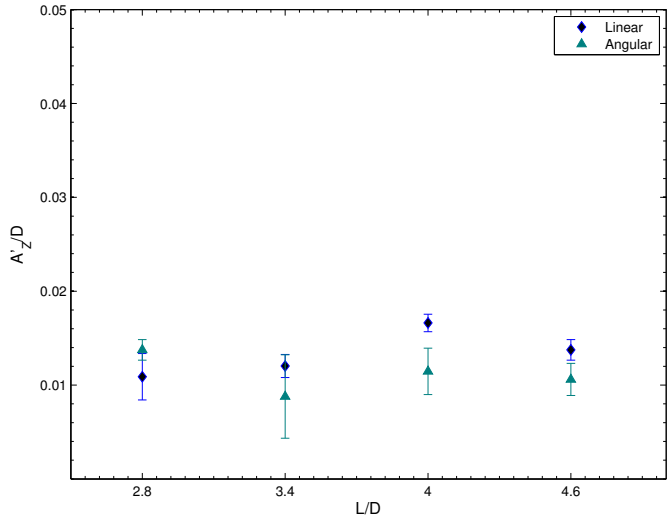

(a) Wire

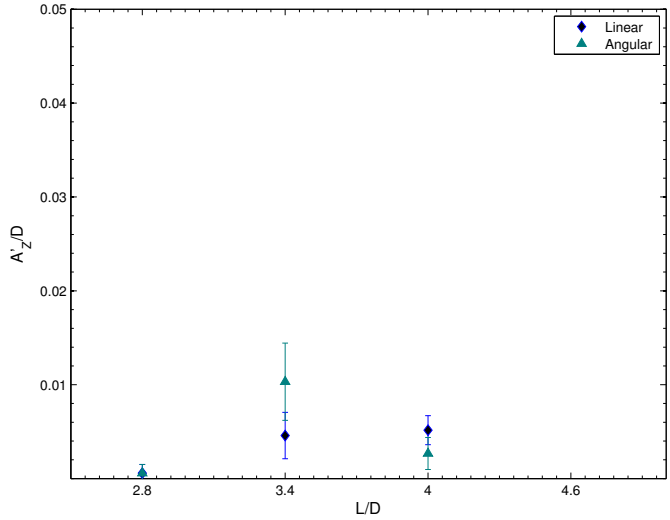

(b) Plate

Figure 4.20: Normalized linear and angular RMS amplitude of point p of the foreign object, at $Tu = 7.5\%$ and $Re_D = 42,682$.

4.1.3 Parametric study

For Foreign Object Search And Retrieval (FOSAR) activities, it is important to prioritize the removal of foreign objects associated with highest risk of tube damage. This section presents the experimental results aimed at identifying the effect of Reynolds number (Re_D), geometry, non-dimensional length (L/D), and turbulence intensity (Tu) on the dynamic response of foreign objects. This analysis will allow conclusions to be drawn in regards to steam generator area and foreign object shape associated with the most significant dynamic response.

Inside steam generator on top of tubesheet, Reynolds number (Re_D) is higher in the periphery of the tube bundle. Different power plants operate their generators at different Reynolds numbers [24]. As discusses in Chapter 2, foreign object location ranges from tube periphery to inside tube bundle, therefore they are exposed to different Reynolds number flows, hence it is important to understand if this affects the foreign object response. Figure 4.21 present the effect of Reynolds number on the amplitude response of point p of the foreign object, by plotting the amplitude response at $Tu = 7.5\%$ and $Re_D = 36,257$, and $Tu = 7.5\%$ and $Re_D = 42,682$. For wire samples (Figure 4.21a) at $Tu = 7.5\%$ and $Re_D = 36,257$, foreign objects seems to move due to impulse type loading acting on them at random intervals. Whereas at $Re_D = 42,682$, random pressure fluctuations larger than static friction is acting continuously on the system causing the foreign object to vibrate. For plate type samples shown in Figure 4.21b, no vibration response is recorded at $Tu = 7.5\%$ and $Re_D = 36,257$. This can be attributed to the fact that in low Re number flow environment the fluctuating forces generated on foreign object surface are not large

enough to overcome static friction resulting in no vibration response. Therefore, foreign objects present in steam generator areas exposed to higher flow velocities are more likely to vibrate and should be given priority during FOSAR activities.

As discussed in Chapter 2, wire and plate type objects constitute a significant portion of the foreign object population found inside steam generator tube bundle; therefore, it is important to understand their dynamic behavior and impact on tube-bundle tubes. Figures 4.22a and 4.22b show the effect of geometry on foreign object amplitude response at $Tu = 2\%$, $Re_D = 36,257$, and $Tu = 7.5\%$, $Re_D = 42,682$, respectively. For reference, the ratio of Reynolds numbers based on the characteristic cross-sectional dimension of wire (Re_{d_w}) and plate (Re_{d_p}) are Re_{d_w}/Re_{d_p}=0.168. Both graphs shows that the geometry of the foreign object plays an important role in its dynamic response, with wire type foreign objects vibrating with larger rms amplitude than plate type. Comparing Figure 4.22a to 4.22b shows that wire sample vibrate with larger amplitude than plate samples of the same length. This is speculated to be at least partially attributed to higher friction experienced by plate objects compared to wire type foreign objects, with the former having larger contact area with the tubes.

Influence of length on the dynamic response of the foreign objects is presented in Figure 4.23. The results indicate that the effect of length on the amplitude response differs for the two foreign object geometries. The rms amplitude of wire type foreign objects appears to be essentially independent of non-dimensional length (Figure 4.23a). In contrast, the dynamic response of plate type foreign object is more susceptible to their length (Figure 4.23b). As discussed earlier, plate samples with $L/D = 2.8$ and 4.6 do not show any appreciable response. For $L/D = 2.8$, the plate sample stays suspended in the tube bundle

due to mean hydrodynamic load without vibrating; whereas, plate samples with $L/D = 4.6$ sunk to the bottom of the bundle.

Turbulence intensity inside tube bundle is lower in peripheral tube rows, as such foreign objects found in tube bundle periphery are exposed to lower turbulence environment when compared to foreign objects found inside the bundle. Figure 4.24 presents the effect of turbulence intensity on the dynamic response of the foreign object. For both wire and plate type objects, their dynamic response decreases with increase in turbulence intensity. However, the decrease seen for the wire sample is less significant than that observed for the plate samples, with the latter geometry showing a suppressed amplitude response when the turbulence intensity increases form 2% to 7.5% (Figure 4.24b). For random forcing due to turbulent flow, significant response is expected for sufficiently high spacial correlations of the forcing function along the foreign object length [13]. Thus, the reduction or suppression of foreign object response with increasing turbulence intensity implies reduction in the correlation length of the dynamic force acting on foreign object surface. Therefore, foreign objects exposed to higher turbulence intensities away from tube bundle periphery can be expected to have smaller response compared to objects located in the first few row.

It is of interest to compare the present results to those of Bonilla et al. [1] conducted in the same experimental facility. Their experiments were conducted at upstream $Tu = 2.0\%$ and $Re_D = 33,775$ (approximately matching the parameters studied here). The plate samples they considered were the same as in the present study, however, wire samples had a diameter 34% smaller than that used in the present. In addition, unlike straight wire samples used here, those studied by Bonilla et al. [1] contained minor bends along the length of the sample, as illustrated in Figure 4.25. Figure 4.26 compares data from the present

study to that from Bonilla et al. [1]. The response of their wire samples shows notable variation from the current study, whereas the response of plate sample is more aligned with the current study. Comparing the results for the wire sample in Figure 4.26a, it can be seen that significant variations in the response with length of the object are observed in the data from Bonilla et al. [1]. In contrast, the current data shows invariance to the length for the wire geometry. The results suggest that even relatively minor deformations of foreign object geometry (Figure 4.25) can lead to significant changes in the amplitude response. For the plate sample, the two data sets indicate a substantial increase in response for L/D around 3.

Based on the results discussed in this section, both wire and plate type foreign objects are more likely to vibrate under higher dynamic pressure flow environment. The RMS amplitude of the foreign object also depends on its geometry, with wire samples vibrating at larger RMS amplitude when compare to plate samples. Moreover, imperfections in geometry of the foreign object can have a substantial effect on the amplitude of vibrations. The non-dimensional length of foreign object does not play a significant role in the amplitude response of wire type foreign objects. In contrast, the object length significantly affects the amplitude of response of plate samples. Finally, the results showed that the rms amplitude for all foreign objects decreases with the increase in the turbulence intensity (Tu) of the flow. Overall, the analysis done in this section shows that foreign objects located in the tube bundle area with relatively low turbulence intensity and high dynamic pressure are more likely to vibrate at appreciable amplitude and should be prioritize during FOSAR activities.

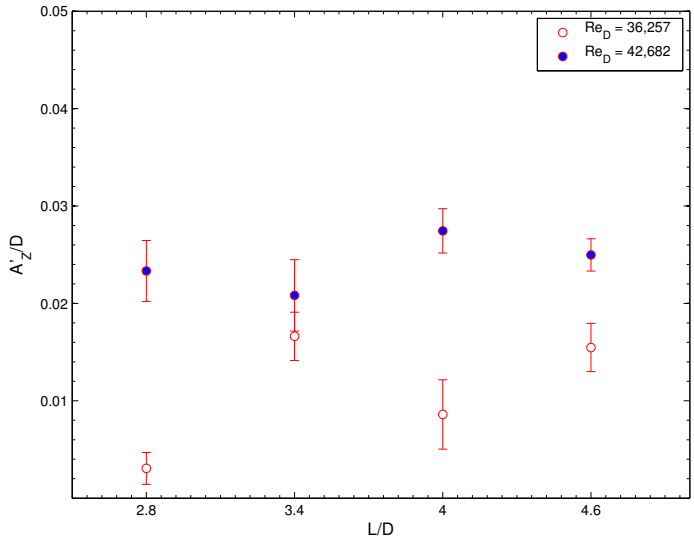

(a)

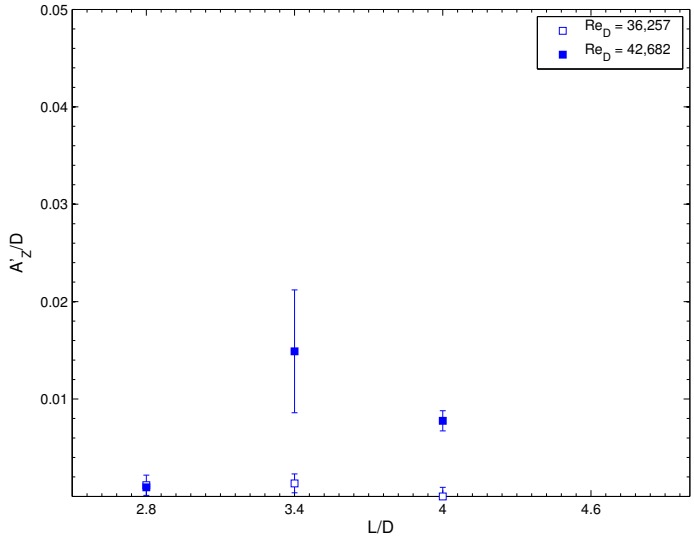

(b)

Figure 4.21: Effect of Reynolds number on the dynamic response of foreign objects at $Tu = 7.5\%$ (a) Wire (b) Plate.

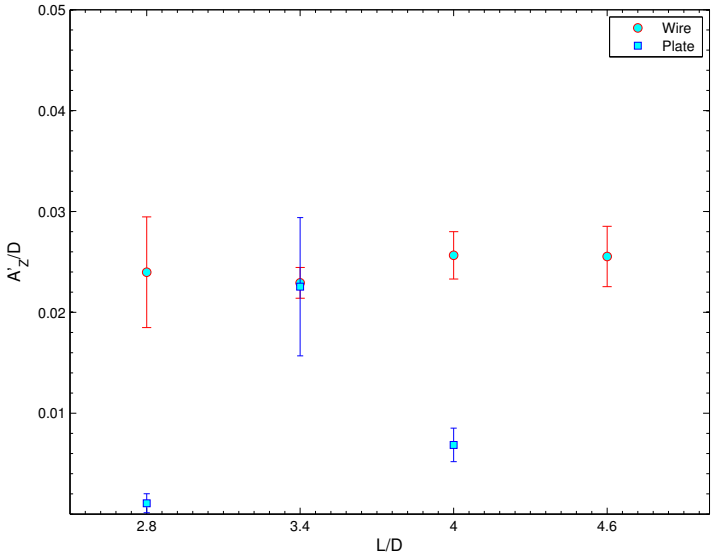

(a)

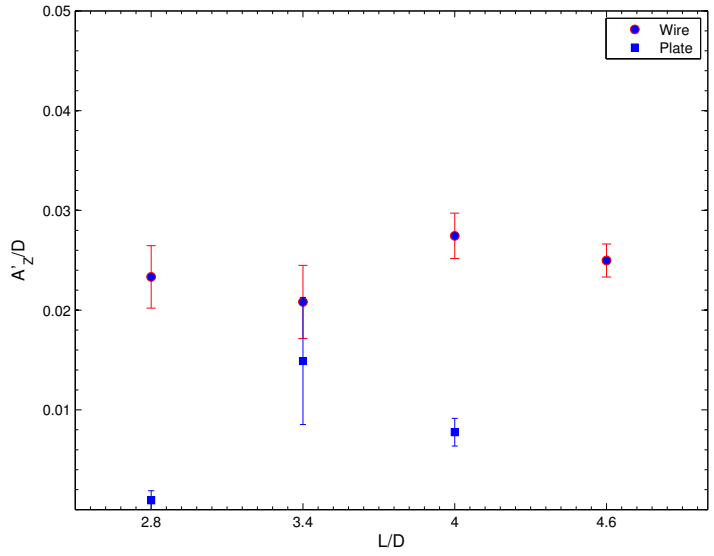

(b)

Figure 4.22: Effect of foreign object geometry on its dynamic response at (a) $Tu = 2\%$ and $Re_D = 36,257$ (b) $Tu = 7.5\%$ and $Re_D = 42,682$.

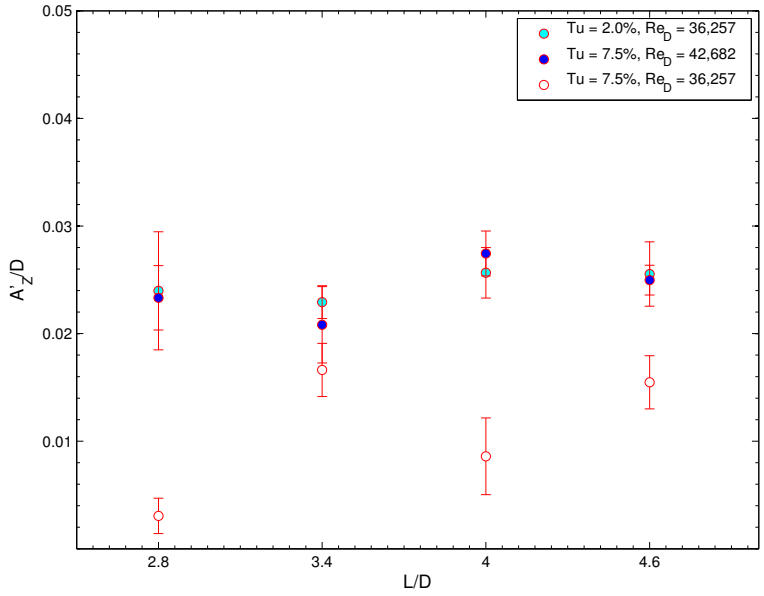

(a)

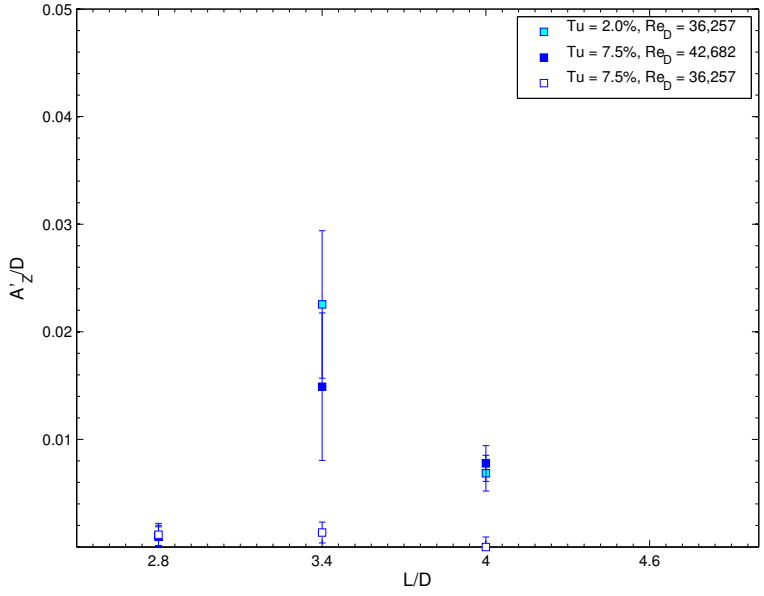

(b)

Figure 4.23: Effect of foreign object length on its dynamic response (a) Wire (b) Plate.

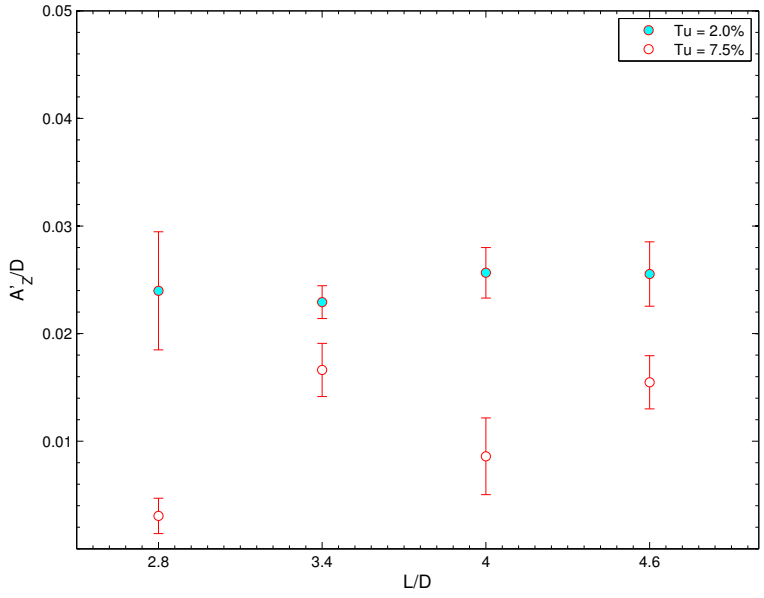

(a)

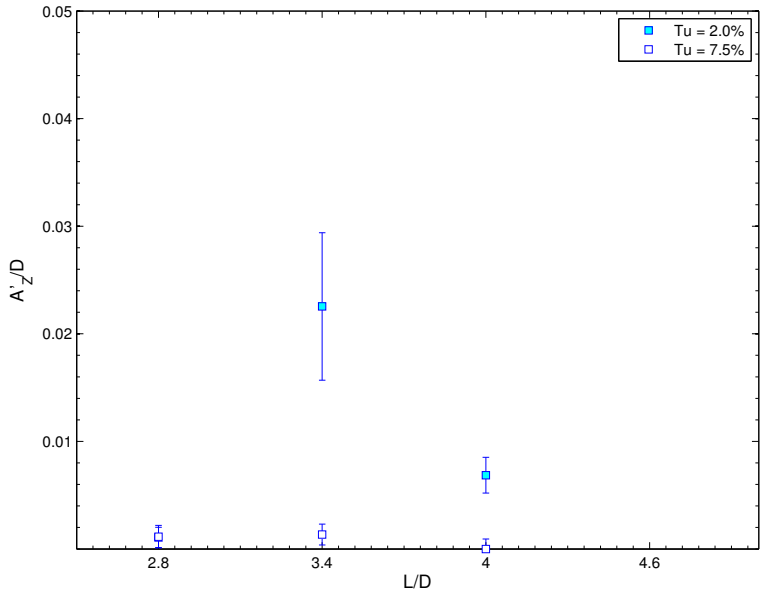

(b)

Figure 4.24: Effect of Turbulence Intensity on the dynamic response of foreign objects at $Re_D = 42,682$ (a) Wire (b) Plate.

(a)

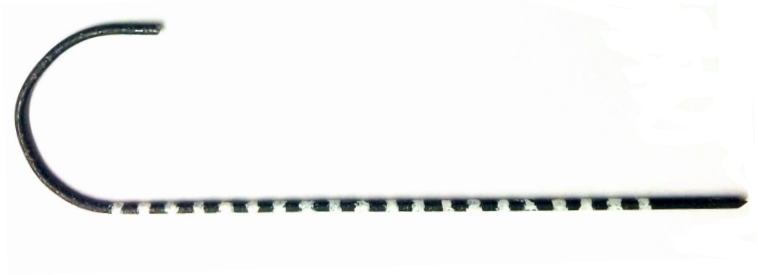

(b)

Figure 4.25: Wire type foreign object (a) used in Bonilla et al. [1] (b) used in current study.

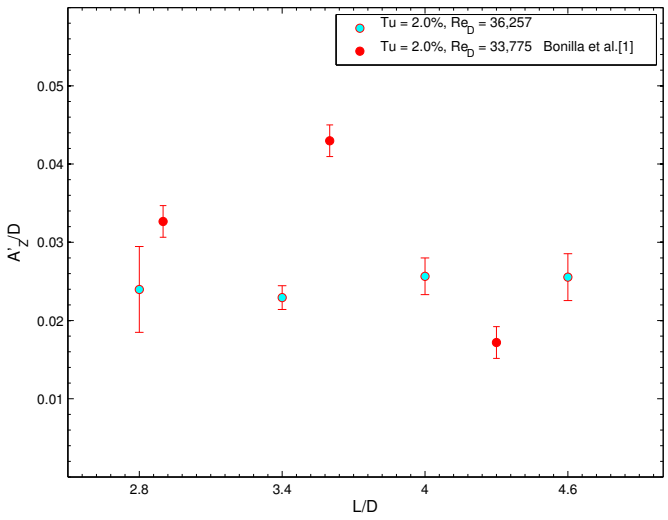

(a)

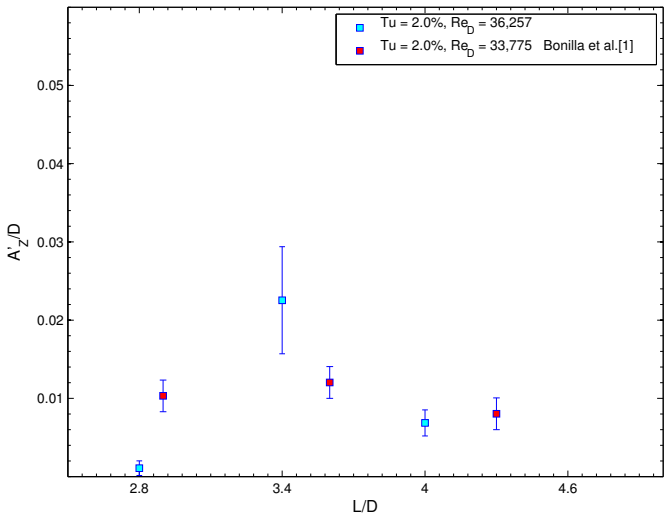

(b)

Figure 4.26: Comparing foreign object response of the current study to the previous study (a) Wire (b) Plate.

4.2 Wear Analysis

From the analysis of foreign object vibrations in the tube bundle performed in previous section, it has been determined that most foreign objects attain substantial amplitude vibrations. In particular, all wire type and most plate type foreign objects investigated vibrate with large peak to peak amplitude resulting in sliding type wear. In contrast, some plate type foreign objects are characterized by very small vibration amplitude not measurable in this study due to the limitations of measuring instruments. For such samples, fretting type wear is expeted due to tube vibration and has been estimated in previous studies [19–22, 26]. Since most foreign objects are typically discovered close to the bottom of the tube sheet, where tube vibration amplitudes are rather small. Thus, this section focuses on the wear due to the vibration of the foreign objects. The wear analysis follows the methodology discussed in Section 3.4 to compute the time for critical tube wear (i.e. time to wear out 40% of tube wall thickness due to foreign objects vibration). Influence of flow velocity, material combination, foreign object geometry and turbulence intensity on critical wear time is used to identify more damaging foreign objects. Additionally, this will help determine the areas inside the tube bundle more susceptible to foreign object related wear damage.

Figure 4.27 illustrates the influence of flow velocity (U_p), material combination and geometry on the amount of time (T) needed by foreign objects to wear out 40% of the tube wall thickness. The results show that both wire and plate type foreign objects exposed to sufficiently high flow velocities has a potential to wear tube bundle tube to its critical wall thickness in less than 4 years. Four years is an important time period since it represents

the planned forced outage cycle in nuclear power plant [28]. It can be seen in Figure 4.27 that T decreases exponentially with increasing U_p. The associated increase in wear intensity is attributed to an increase in normal force on the foreign object and sliding distance experience by tube bundle tube.

The material of foreign object and tubes inside tube bundle can vary, therefore it is important to see the influence of material combination on critical wear time. In Figure 4.27, typical materials of recovered foreign objects (S304, S409 and S403) and tube materials (I600 and I690) are considered. The results show that the effect of material combination becomes progressively more significant as the velocity decreases. For higher flow velocity, the normal force and sliding distance become dominating factor governing critical wear time, therefore reducing the influence of material combination at higher speeds. In addition, wear of I690 tubes is more aggressive when compared to I600 tubes for both wire and plate samples. This can be attributed to the properties of the material itself (such as hardness) resulting in higher wear coefficient.

The effect of foreign object geometry on critical wear time for material combination considered is also illustrated in Figure 4.27. The results indicate that wear due to plate samples is more aggressive when compared to wire samples. In particular, for I690/S304 material combination, wire samples require flow environment with pitch velocity of $3.4m/s$ which is 24% higher than plate samples to reach critical wear time of less than 4 years. This is mainly attributed to the larger sliding distance and normal force experience by tube bundle tubes due to plate-type foreign objects. During its motion, due to larger contact area, the plate samples stays in contact with the same area of tube bundle tube for much longer period of time compared to wire samples resulting in tube bundle tubes

experiencing larger sliding distance due to plate samples. In addition, tube bundle tubes experience larger normal contact force due to plate samples, hence resulting in higher wear. Similar to the effect of material combination, the effect of foreign object geometry becomes more evident in low flow velocity environment.

Tube bundle acts as turbulence generator and turbulence intensity experienced by a foreign object in the inner rows is higher compared to the periphery of the tube bundle [34, 35] . Figure 4.28 shows the influence of turbulence on the tube wear due to foreign objects. For both wire and plate samples, turbulence intensity plays an important role in determining the critical wear time, with faster wear observed at lower Tu levels. This is attributed to the increase in sliding distance with decreasing Tu level, hence decreasing wear time for wire and plate samples (Figure 4.28a and 4.28b).

Pitch velocities in tube periphery 2 to 3 inches above tube sheet in industrial stream generator reaches as high as 8 m/s [30]. Based on the results discussed in this section, it can be conclude that wire or plate type foreign object can produce critical tube damage in under four years within a velocity range typical to the operation of industrial steam generator. The material combination of vibrating objects has a more significant effect on the critical wear time only at lower flow speeds, with the effect becoming secondary as the flow speed increases. In addition, wear seen due to plate type foreign object is more aggressive as compared to wire type foreign objects. Finally, higher turbulence intensity environment tends to increase critical wear time, meaning the potential to damage the tube bundle tubes due to foreign objects placed in high turbulence intensity and low dynamic pressure environment i.e. inside the bundle is low relative when compared to tube periphery.

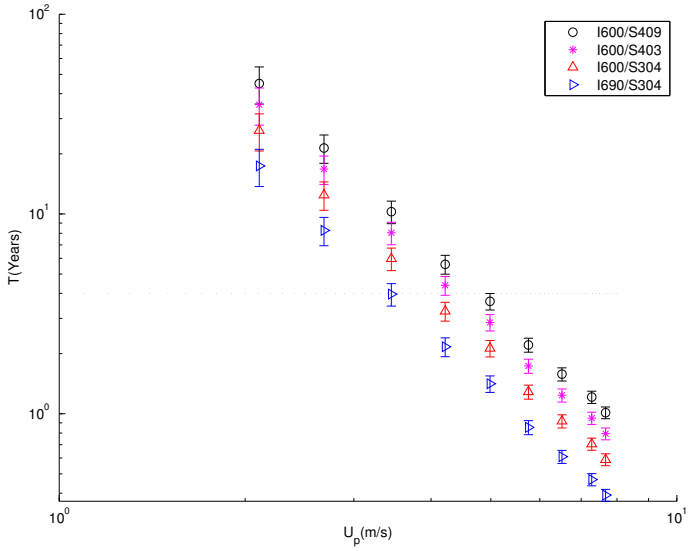

(a) Wire

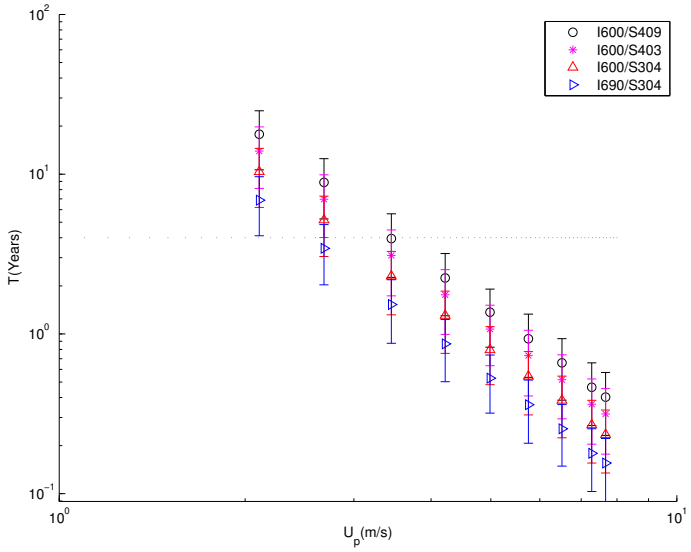

(b) Plate

Figure 4.27: Critical wear time(T) to wear out 40% of tube wall thickness as a function of flow velocity due to the vibration of foreign objects at Tu = 2.0% .

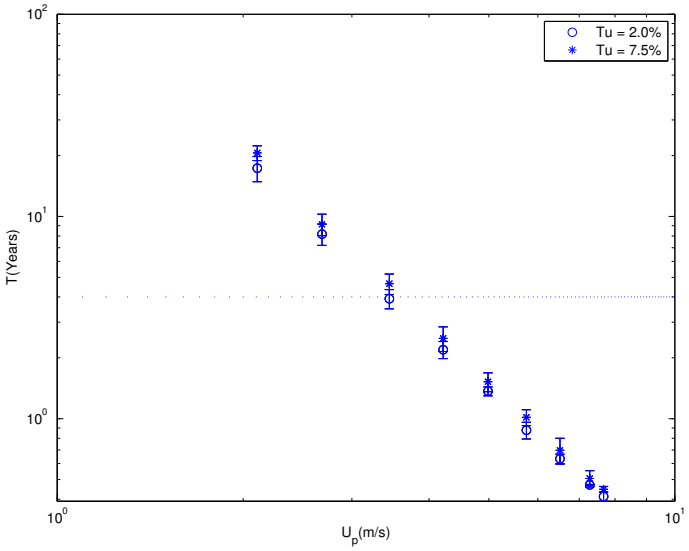

(a) Wire

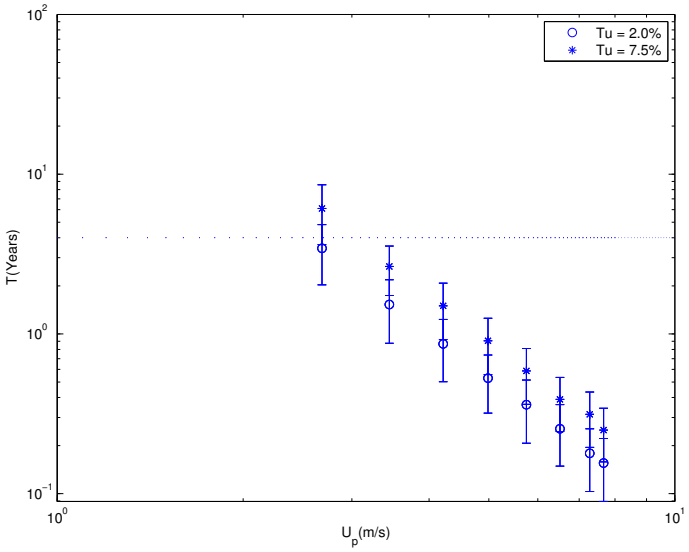

(b) Plate

Figure 4.28: Influence of turbulence intensity(Tu) on the critical wear time(T) as a function of flow velocity for I690/S304 material combination.

Chapter 5

Conclusion

This study experimentally investigated the three dimensional dynamic response of foreign objects inside peripheral tubes of the normal-triangular tube bundle (with P/D = 1.35), and semi-empirically estimated the amount of time required to cause critical wear damage to the tubes. The main objective was to understand the foreign object dynamics, identify the types of foreign objects and areas inside the tube bundle tube where foreign objects are most likely to vibrate and cause critical wear damage. The dynamics of foreign object was studied by experimentally studying the three dimensional response of hooked shape wire or plate type foreign object with non-dimensional length L/D = 2.8, 3.4, 4.0, 4.6 at Re_D = 36,257 and 42,682, and Tu = 2.0% and 7.0%, respectively. The hooked shape geometry allowed foreign object to have minimum constrains inside tube bundle, and hence allowed it to have pitching, yawing and Z direction translation response. This, then permits the tube bundle tube to experience fretting, pure sliding, impact sliding and impact fretting, type of wear processes due to foreign objects. The corresponding wear damage to the tube

bundle tubes was studied by employing Archard's semi-empirically wear equation. Wear coefficient for the material pairs of interest were obtained from previous empirical studies, whereas other parameters such as sliding velocities, wear volume and normal forces were either estimated through experiments or by extrapolation.

Experimentally recorded dynamic response of all foreign objects showed that these objects undergo stationary random vibration inside the tube bundle. The foreign object displacement autocorrelation function resembles the autocorrelation function of white-noise signal. In addition, the absence of distinct spectral peaks in the displacement power spectral density pointed to foreign objects undergoing wide-band type random vibration response. Moreover, the results also showed the amplitude response to be non Gaussian. Finally, in low turbulence intensity and high Reynolds number flow environment the response probability density function (PDF) was closer to the normal PDF, but deviates largely from normal as the turbulence intensity increases and Reynolds number decreases.

Study of foreign object's kinematics showed that the Z amplitude response was relatively large when compared to the response recorded in the X and Y direction for both wire and plate type foreign objects. In addition, for both wire and plate samples the contribution of the yaw component was negligible to the overall motion. This resulted in the motion of foreign objects to be of planar type, hence restricting the dynamic interaction between tube bundle tube and foreign object surface to be of pure sliding type. Finally, the kinematic study also showed the planar response of all the vibrating foreign objects to have contribution from both pitching and translation component of motion.

The parametric study showed that the geometry of the foreign object influences its dynamic response, with wire type foreign object vibrating at larger rms amplitude compared

to plate type objects. The effect of non-dimensional length (L/D) on the dynamic response varies with geometry, with L/D not playing a significant role in amplitude response of wire type foreign objects. In contrast, it significantly affects the amplitude response of plate samples, as such only samples with non-dimensional length L/D = 3.4 and 4.0 showed measurable vibration response. Moreover both wire and plate type foreign objects are more likely to vibrate in high Reynolds number flow environment, and their RMS amplitude decreases with the increase in turbulence intensity. Comparing the results from the current study to those form Bonilla et al. [1], even minor changes in the foreign object geometry could result in large changes in the foreign object dynamic response. The results of this investigation showed that inside tube-bundle wire type objects are more likely to vibrate when compared to plate type objects. In addition, foreign objects are more likely to vibrate inside tube bundle areas where the turbulence intensity is lower and Reynolds number is higher, which is the case at the periphery of the tube bundle.

Semi-empirical wear study showed that the time required to do critical wear damage to the tube bundle tubes decreases with the increase in pitch velocity for both wire and plate samples. Material combination has a more significant effect on critical wear time (T) only at lower flow speeds, with the effect becoming secondary as the flow speed increases. Wear due to plate type foreign geometry is more aggressive when compared to the wire type geometry. Since all wire type foreign objects exhibit relatively larger peak-to-peak amplitude vibration response, therefore only sliding type wear is expected, whereas some plates samples that do not produce measurable response and stay in one place could undergo fretting wear damage due to the vibrations of the tubes. Additionally, increase in turbulence intensity of the flow environment results in an increase in the critical wear time. However, similar

to material combination the influence of foreign object geometry and turbulence intensity becomes progressively more significant as the velocity decreases. Based on the results from the current study, it is recommended that during FOSAR activities, priority should be given to the foreign objects found in high pitch velocity and low turbulence intensity flow environment i.e. tube periphery when compared to objects found in-bundle, as they are more likely to vibrate and cause critical wear damage to the tube bundle tubes within four year time period.

Chapter 6

Recommendations

Current study has provided useful insight into the foreign object dynamics and their impact on tube bundle tubes but at the same time has raised some unsolved questions. For the future investigation on this topic, following recommendations are provided:

1. Investigate the influence of tube bundle parameters such as array geometry, pitch-to-diameter ratio, etc., on the dynamics of foreign object. In current study, all experiments were performed in a normal triangular tube bundle geometry with P/D = 1.35. By changing the tube bundle geometry to in-line, rotated square, parallel triangle, etc., or changing the pitch-to-diameter ratio will change the flow environment (such as, large P/D tube bundle might produces turbulence of large scale eddied, have different velocity distribution inside tube bundle) hence influencing the dynamic forces acting on the foreign object. Since tube bundle array parameters differ in different nuclear power plants, studying the influence of these parameters will be helpful during FOSAR activities.

2. Inside the tube bundle foreign objects are oriented randomly, therefore studying the influence of foreign object orientation for example placing foreign object at yaw angle of 180 (i.e. cross flow orientation) etc ., on the dynamic response and tube wear should be helpful in further understanding foreign object vibration response inside the tube bundle.

3. Further investigate the influence of turbulence intensity and Reynolds number on foreign object dynamic response and critical wear time. Current study strictly focused on dynamic response of tube bundle when upstream turbulence is 2.0% and 7.5% produced by only one mesh size(whereas inside tube bundle turbulence intensity can go up to 40%). Changing the mesh size can vary the scale of the eddies produced, which could influence the dynamic forces and hence foreign object response.

4. Study the dynamic response of foreign object that sinks to the tube sheet. In the current study, response of some foreign objects was not recorded as they drop out of the measurement volume to the tube sheet. Many foreign objects in industrial steam generator are found on the tube sheet hence understanding the response on tube sheet is also important.

5. Current study used sliding wear coefficients from previous empirical studies, which do not always match the wear environment inside different steam generators. Therefore, the sliding wear coefficients needed to be empirically obtained at the temperature and environment matching the inside of steam generator to provide better estimate of wear due to sliding wear process.

6. Do fretting wear analysis for objects that do not vibrate and compare them to the

sliding wear. Some objects did not exhibit larger enough peak-to-peak amplitude to be recorded by the current measurement system. Such objects can cause fretting type wear damage, investigating wear due to such objects and comparing them to the wear experienced due to objects undergoing sliding motion would be helpful in prioritizing foreign objects during FOSAR activities.

Bibliography

[1] S. M. Bonilla, S. Mahey, and S. Yarusevych, "Flow-induced vibration of flexible fragments lodged in tube bundle," tech. rep., University of Waterloo, Waterloo, 2013.

[2] W. D. Pilkey, *Formulas for Stress, Strain, and Structural Matrices.* Hoboken, NJ, USA: John Wiley & Sons, Inc., oct 2004.

[3] IAEA, "Reference data Series No. 2, 2015 Edition: Nuclear Power Reactors in the World," Tech. Rep. 2, Vienna, 2015.

[4] K. S. Kang and L. Kupcan, "Assessement and Management of Ageing of Major Nuclear Power Plant Components Important to Safety: Steam Generators," tech. rep., IAEA, Vienna, 2011.

[5] L. Bonavigo and M. D. Salve, *Steam Generator Systems: Operational Reliability and Efficiency.* 2011.

[6] P. MacDonald, P.E., Shah, V.N., Ward, L.W., Ellison, "Steam Generator Tube Failures," tech. rep., Idaho National Engineering Laboratory, Idaho, 1996.

[7] E. Fuller, "Steam generator integrity assessment guidelines: revision 2," tech. rep., EPRI, California, 2006.

[8] P. Push and W. McCurdy, "PWR Steam Generator Foreign Object Exclusion Systems," tech. rep., EPRI, Alexandria, 2006.

[9] H. Cothron, "Steam Generator Management Program : Steam Generator Integrity Assessment Guidelines," tech. rep., EPRI, 2008.

[10] Y. Liao and S. Guentay, "Potential steam generator tube rupture in the presence of severe accident thermal challenge and tube flaws due to foreign object wear," *Nuclear Engineering and Design*, vol. 239, pp. 1128–1135, 2009.

[11] A. Zukauskas, *High-Performance Single-Phase Heat Exchanger.* New York: Hemisphere Publishing Corporation, 1989.

[12] S. Ziada, "Vorticity shedding and acoustic resonance in tube bundles," *Journal of the Brazilian Society of Mechanical Sciences and Engineering*, vol. 28, no. 2, pp. 186–189, 2006.

[13] M. K. Au-Yang, *Flow-Induced Vibration of Power and Process Plant Components.* New York: ASME, 2001.

[14] R. D. Blevins, *Flow-Induced Vibration.* New York: Van Nostrand Reinhold, 2 ed., 1990.

[15] G. Parkinson, "Phenomena and modelling of flow-induced vibrations of bluff bodies," *Progress in Aerospace Sciences*, vol. 26, no. 2, pp. 169–224, 1989.

[16] J. D. Hartog, *Mechanical Vibrations*. New York: Dover Publications, 1985.

[17] G. Straffelini, *Friction and Wear*. Springer Tracts in Mechanical Engineering, Cham: Springer International Publishing, 2015.

[18] I. K. Å. Íková, B. Szewczyková, P. Blaškovitš, E. Hodúlová, and E. L. Č, "Study and Characteristic of Abrasive Wear Mechanisms," pp. 1–9, 2012.

[19] D. G. Kim and Y. Z. Lee, "Experimental investigation on sliding and fretting wear of steam generator tube materials," *Elsevier*, vol. 250-251, pp. 673–680, 2001.

[20] H.-N. Kim, H.-J. Yoo, and K.-W. Ryu, "Wear Prediction of Steam Generator Tubes due to Shell Side Foreign Objects," *Journal of Nuclear Science and Technology*, vol. 47, no. 7, pp. 582–590, 2010.

[21] H.-N. Kim, N.-C. Cho, and M.-W. Nam, "Wear on Plugged Tube due to the Foreign Objects on the Secondary Side of Steam Generator," in *Transaction of the Korean Nuclear Society Autumn Meeting*, (Gyeongju), 2013.

[22] J. C. Jo, M. J. Jhung, W. S. Kim, Y. H. Choi, H. J. Kim, and T. H. Kim, "Fretting-Wear Characteristics of Steam Generator Tubes by foreign objects.," *Journal of the Korean Nuclear Society*, pp. 442–453, 2003.

[23] O. Alquaddoomi and I. Catton, "Investigation of the Interaction between Steam Generator Tubes and Foreign Objects Resulting in Tube Wear," in *Nuclear Energy for New Europe*, 2008.

[24] T. K. Poddar and G. T. Polley, *Heat Exchanger Design Handbook*. 2000.

[25] T. Babcock and W. Company, *Steam: Its generation and use*. 2007.

[26] C. Park, "Steam Generator Management Program : PWR Steam Generator Tube Wear Alloy 690 / Supports and Alloy 690 / Foreign Objects," tech. rep., EPRI, Daejeon, 2007.

[27] K. Karawoski, G. Makar, and M. Yoder, *U . S . Operating Experience With Thermally Treated Alloy 600 Steam Generator Tubes*. 2007.

[28] R. Spiegelberg and J. Mandula, "Indicators for Management of Planned Outages in Nuclear Power Plants," Tech. Rep. April, International Atomic Energy Agency, Vienna, 2006.

[29] U. S. N. Regulatory, "NRC Integrated Program for the Resolution of Unresolved Safety Issues A-3 , A-4 , and A-5 Regarding Steam Generator Tube Integrity,"

[30] S. Fuite, "Foreign objects inside steam generator," tech. rep., Babcock & Wilcox, Canada, 2013.

[31] L. A. Endres and S. V. Möller, "On the fluctuating wall pressure field in tube banks," *Nuclear Engineering and Design*, vol. 203, no. 1, pp. 13–26, 2001.

[32] Y. A. Hassan and H. R. Barsamian, "Tube bundle flows with the large Eddy simulation technique in curvilinear coordinates," *International Journal of Heat and Mass Transfer*, vol. 47, no. 14-16, pp. 3057–3071, 2004.

[33] M. Zdravkovich, "The effects of interference between circular cylinders in cross flow," *Journal of Fluids and Structures*, vol. 1, no. June 1985, pp. 239–261, 1987.

[34] L. K. Grover and D. S. Weaver, "Cross-Flow Induced Vibrations Shedding Bank-Vortex," *Sound And Vibration*, vol. 59, pp. 263–276, 1978.

[35] E. Naudascher and D. Rockwell, *Flow-Induced Vibration*. New York: Dover Publications, 2005.

[36] M. Zdravkovich, *Flow Around Circular Cylinders: Applications*. New York: Oxford University Press, 2003.

[37] P. R. Owen, "Buffeting excitation of boiler tube vibration," *ARCHIVE: Journal of Mechanical Engineering Science 1959-1982 (vols 1-23)*, vol. 7, no. 4, pp. 431–439, 1965.

[38] A. Abd-Rabbo and D. Weaver, "A flow visualization study of flow development in a staggered tube array," *Journal of Sound and Vibration*, vol. 106, no. 2, pp. 241–256, 1986.

[39] D. Polak and D. Weaver, "Vortex shedding in normal triangular tube arrays," 1994.

[40] D. S. Weaver, J. A. Fitzpatrick, and M. ElKashlan, "Strouhal Numbers for Heat Exchanger Tube Arrays in Cross Flow," *Journal of Pressure Vessel Technology*, vol. 109, no. 2, p. 219, 1987.

[41] D. S. Weaver, "A review of cross-flow induced vibration in heat exchanger array.," *Journal of Fluid and Structures*, no. May 1987, pp. 73–93, 1988.

[42] S. Ziada and A. Oengören, "An in-depth study of vortex shedding, acoustic resonance and turbulent forces in normal triangle tube arrays," *Journal of Fluids and Structures*, vol. 12, pp. 717–758, 1998.

[43] P. Stephan, H. Martin, S. Kabelac, D. Mewes, M. Kind, and K. Schaber, *VDI Heat Atlas*. Berlin, Heidelberg: Springer Berlin Heidelberg, 2010.

[44] T. Kuppan, *Heat exchanger design handbook*. Boca Raton: CRC Press., 2nd ed., 2013.

[45] A. M. Pankonien and Z. Ounaies, "Piezoelectric artificial kelp for energy harvesting," in *ASME Conference on Smart Materials, Adaptive Structures and intellighent systems.*, 2010.

[46] W. B. Hobbs and D. L. Hu, "Tree-inspired piezoelectric energy harvesting," *Journal of Fluids and Structures*, vol. 28, pp. 103–114, 2012.

[47] O. Griffin, "Vortex Shedding from bluff bodies in a shear flow: A Review," *Journal of Fluids Engineering*, vol. 107, no. SEPTEMBER 1985, pp. 298–306, 1985.

[48] A. Richter and E. Naudascher, "Fluctuating forces on a rigid circular cylinder in confined flow," *Journal of Fluid Mechanics*, vol. 78, no. 3, pp. 561–576, 1976.

[49] S. E. Ramberg, "The effects of yaw and finite length upon the vortex wakes of stationary and vibrating circular cylinders," *Journal of Fluid Mechanics*, vol. 128, no. -1, p. 81, 1983.

[50] A. Jain, *Vortex-Induced Vibrations of an Inclined Cylinder in Flow.* PhD thesis, 2009.

[51] B. Hubran, M. Hamdan, and B. A. Bedoor, "Interference & turbulence intensity effects on the flow induced vibration of smooth & rough cylinders-main.pdf," *Journal of Fluid and Structures*, vol. 7, pp. 457–470, 1993.

[52] K. Y. Billah, "Resonance, Tacoma Narrows bridge failure, and undergraduate physics textbooks," *American Journal of Physics*, vol. 59, no. 2, p. 118, 1991.

[53] M. P. Paidoussis, S. J. Price, and E. de Langre, *Fluid-Structure Interactions: Cross-Flow-Induced Instablilites.* New York: Cambridge University Press, 2011.

[54] G. H. Toebes and P. S. Eagleson, "Hydroelastic Vibrations of Flat Plates Related to Trailing Edge Geometry," *Journal of Basic Engineering*, vol. 83, no. 4, p. 671, 1961.

[55] G. Parkinson, "Aeroelastic galloping in one degeree of freedom.," in *Wind effects on buildings and Structures.*, (Teddington), pp. 582–609, 1963.

[56] Y. Nakamura and Y. Tomonari, "Galloping of rectangular prisms in a smooth and in a turbulent flow," *Journal of Sound and Vibration*, vol. 52, no. 2, pp. 233–241, 1977.

[57] M. Matsumoto, N. Shiraishi, M. Kitazawa, C. Knisely, H. Shirato, Y. Kim, and M. Tsujii, "Aerodynamic Behaviour of Inclined Circular Cylinders - Cable Aerodynamics," *Journal of Wind Engineering and Industrial Aerodynamics*, vol. 33, pp. 63–72, 1990.

[58] A. Laneville and G. Parkinson, "Effects if turbulence on galloping of bluff cylinders.," in *Proceedings of the Third International Conference on Wind Effects on Buildings and Structures.*, (Tokyo), pp. 787–797, 1971.

[59] C. Lalanne, *Random Vibration: Mechanical Vibration and Shock Analysis*. Hoboken: Wiley, 2009.

[60] W.-F. Chen and E. M. Lui, *Handbook of Structural Engineering, Second Edition*. 2005.

[61] S. D. Savkar, "A Brief Review of Flow Induced Vibrations of Tube Arrays in Cross-Flow," *Journal of Fluids Engineering*, vol. 99, no. 3, p. 517, 1977.

[62] S. Savkar, R. So, and T. Litzinger, "Fluctuating lift and drag forces induced on large bluff bodies in a turbulent cross-flow," in *Flow-induced Heat Exchanger Tube Vibration*, 1980.

[63] D. Gorman, "Effects of artificially induced up-stream turbulence on the liquid cross-flow induced vibration of tube bundles," in *Flow-Induced Vibration of Power Plant Components*, pp. 33–43, 1980.

[64] H. Bruun and P. Davies, "An Experimental Investigation of the Separation Points on a Circular Rotating Cylinder in Cross Flow," *Journal of Sound and Vibration*, vol. 4, pp. 535–559, 1975.

[65] L. Meirovitch and R. Parker, "Fundamentals of Vibrations," 2001.

[66] S. M. Hong and I. S. Kim, "Impact fretting wear of alloy 690 tubes at 25 degree C and 290 degree C," *Wear*, vol. 259, no. 1-6, pp. 356–360, 2005.

[67] G. G. Kim and S. J. Kim, "A Study on Sliding Wear Behavior of Alloy 600 Steam Generator Tubes in NPPs," in *Proceedings of the Korean Nuclear Society Spring Meeting*, (Gyeongju), 2004.

[68] N. J. Fisher, A. B. Chow, and M. K. Weckwerth, "Experimental Fretting-Wear Studies of Steam Generator Materials," *Journal of Pressure Vessel Technology*, vol. 117, no. 4, p. 312, 1994.

[69] G. X. Chen and Z. R. Zhou, "Study on transition between fretting and reciprocating sliding wear," *Wear*, vol. 250-251, no. PART 1, pp. 665–672, 2001.

[70] C. Donnet and A. Erdemir, eds., *Tribology of Diamond-Like Carbon Films*. Boston, MA: Springer US, 2008.

[71] P. L. Ko, "Experimental Studies of Tube Frettings in Steam Generators and Heat Exchangers," *Journal of Pressure Vessel Technology*, vol. 101, no. 2, p. 125, 1979.

[72] J. F. Archard and W. Hirst, "The Wear of Metals under Unlubricated Conditions," in *Proceedings of the Royal Society A: Mathematical, Physical and Engineering Sciences*, vol. 236, pp. 397–410, 1956.

[73] I. F. Stowers and E. Rabinowicz, "The Mechanism of Fretting Wear," *Journal of Lubrication Technology*, vol. 95, no. 1, p. 65, 1973.

[74] H. Connors, "Flow-Induced vibration and wear of steam generator tubes," *Nuclear Technology*, vol. 55, pp. 311–330, 1981.

[75] D.-I. Kwon, J.-K. Hong, and I.-S. Kim, "Impact Fretting Wear of Steam Generator Tubes," No. May, 2003.

[76] F. Guerout and N. Fisher, "Steam Generator Fretting-Wear Damage: A Summary of Recent FIndings," *Journal of Pressure Vessel Technology*, vol. 121, no. 3, pp. 304–310, 1999.

[77] P. Hofmann, B. Friedrich, and H. Schrod, "Prediction of PWR Steam Generator Tube Material Loss caused by Perpendicular Impacting," in *Flow-Induced Vibration - PVP* (M. Pettigrew, ed.), (Montreal), pp. 219 – 231, 1996.

[78] Y. H. Lee, I. S. Kim, S. S. Kang, and H. D. Chung, "A study on wear coefficients and mechanisms of steam generator tube materials," *Wear*, vol. 250-251, no. PART 1, pp. 718–725, 2001.

[79] P.J. Holfmann and T. Schettler, "PWR Steam Generator Tube Fretting and Fatigue Wear," tech. rep., EPRI, 1989.

[80] M. K. Lim, S. D. Oh, and Y. Z. Lee, "Friction and wear of Inconel 690 and Inconel 600 for steam generator tube in room temperature water," *Nuclear Engineering and Design*, vol. 226, no. 2, pp. 97–105, 2003.

[81] Y. H. Lee, H. K. Kim, H. D. Kim, C. Y. Park, and I. S. Kim, "A comparative study on the fretting wear of steam generator tubes in korean power plants," *Wear*, vol. 255, no. 7-12, pp. 1198–1208, 2003.

[82] S. H. Jeong, C. W. Cho, and Y. Z. Lee, "Friction and wear of Inconel 690 for steam generator tube in elevated temperature water under fretting condition," *Tribology International*, vol. 38, no. 3, pp. 283–288, 2005.

[83] K. Kawamura, A. Yasuo, and F. Inada, "Tube-to-Support Dynamic Interaction Caused by Turbulent Flow-Induced Vibration.," in *ASME Special Publication PVP*, pp. 119–128, 1991.

[84] G. S. Park, G. G. Kim, and S. J. Kim, "Sliding wear behaviors of steam generator tube materials in high temperature water environment," *Journal of Nuclear Materials*, vol. 352, no. 1-3, pp. 80–84, 2006.

[85] D. G. Kim and Y. Z. Lee, "Experimental investigation on sliding and fretting wear of steam generator tube materials," *Wear*, vol. 250-251, no. PART 1, pp. 673–680, 2001.

[86] P. Roach, "The generation of nearly isotropic turbulence by means of grids," *International Journal of Heat and Fluid Flow*, vol. 8, no. 2, pp. 82–92, 1987.

[87] D. S. Weaver and M. El-Kashlan, "On the number of tube rows required to study cross-flow induced vibrations in tube banks," *Journal of Sound and Vibration*, vol. 75, no. 2, pp. 265–273, 1981.

[88] X. Li, X. Wu, and S. He, "Numerical investigation of the turbulent cross flow and heat transfer in a wall bounded tube bundle," *International Journal of Thermal Sciences*, vol. 75, no. JANUARY 2014, pp. 127–139, 2014.

[89] R. J. Adrian and C. S. Yao, "Power spectra of fluid velocities measured by laser Doppler velocimetry," *Experiments in Fluids*, vol. 5, pp. 17–28, 1987.

[90] D. Diercks, "Strategy for Assessment of WWER Steam Generator Tube Integrity," tech. rep., 2007.

[91] L. Yang, J. Hals, and T. Moan, "Analysis of dynamic effects relevant for the wear damage in hydraulic machines for wave energy conversion," *Ocean Engineering*, vol. 37, no. 13, pp. 1089–1102, 2010.

[92] J. K. Hong and I. S. Kim, "Environment effects on the reciprocating wear of Inconel 690 steam generator tubes," *Wear*, vol. 255, no. 7-12, pp. 1174–1182, 2003.

[93] D. Yeo and N. P. Jones, "Computational Study on 3-D Aerodynamic Characteristics of Flow around a Yawed, Inclined, Circular Cylinder," Tech. Rep. March, University of Illionois, Urbana, 2011.

[94] S. Poulin and A. Larsen, "Drag loading of circular cylinders inclined in the along-wind direction," *Journal of Wind Engineering and Industrial Aerodynamics*, vol. 95, no. 9-11, pp. 1350–1363, 2007.

[95] W. J. Michael, "Flow studies in the vicinity of a modified flat-plate rectangular wing of aspect ratio 0.25," tech. rep., Langley Aeronautical Laboratory, Langley Field, 1952.

[96] W. Bollay, *A new theory for wing of small aspect ratio*. PhD thesis, California Institute of Technology, 1936.

[97] X. Ortiz, D. Rival, and D. Wood, "Forces and moments on flat plates of small aspect ratio with Application to PV wind loads and small wind turbine blades," *Energies*, vol. 8, no. 4, pp. 2438–2453, 2015.

[98] L. Yang, *Stochastic dynamic system analysis of wave energy converter with hydraulic power take-off , with particular reference to wear damage analysis Limin Yang Stochastic dynamic system analysis of wave energy converter with hydraulic power take-off ,*. PhD thesis, Norwegian Univeristy of Science and Technology, 2011.

[99] R. Hibbler, *Engineering Mechanics Dynamics*. New York: Pearson, 12 ed., 2009.

[100] A. P. J.S. Bendat, L.D. Enochson, "Test for Randomness, Stationarity, Normality and Comparison of Spectra," tech. rep., AF Flight Dynamics Laboratory, Los Angeles, 1964.

[101] C.H.Chen, *Signal Processing Handbook*. New York: Marcle Dekker, 1988.

[102] C. Bailly and G. Comte-Bellot, *Turbulence Second ed: Experimental Fluid Mechanics*. New York: Cham : Springer, 2015.

[103] Z. Liang and G. C. Lee, *Random Vibraiton: Mechanical, Structural and Earthquake Engineering Applicaions*. New York: CRC Press, 2015.

[104] J. S. Bendat, L. D. Enochson, G. H. Klein, and A. G. Piesol, "The application of statistics to the flight vehicle vibration problem," tech. rep., Aeronautical System Division, Ohio, 1961.

[105] J. A. Mullin and W. J. A. Dahm, "Dual-plane stereo particle image velocimetry (DSPIV) for measuring velocity gradient fields at intermediate and small scales of turbulent flows," *Experiments in Fluids*, vol. 38, no. 2, pp. 185–196, 2005.

[106] K. Ehrenfried, "Processing calibration-grid images using the Hough transformation," *DLR-Mitteilung*, no. 3, pp. 1263–1268, 2001.

[107] S. G. Paikowsky and F. Xi, "Particle Motion Tracking Utilizing a High-Resolution Digital CCD Camera," *Geotechnical Testing Journal*, vol. 23, no. 1, pp. 123–134, 2000.

[108] S. Ahn and J. Fessler, "Standard Errors of Mean, Variance, and Standard Deviation Estimators," *EECS Department, University of Michigan*, no. 2, pp. 2–3, 2003.

[109] S. Castrup and H. T.Castrup, *Measurement Uncertainty Analysis Principles and Methods*. No. July, 2010.

[110] R. J. Moffat, "Describing the uncertainties in experimental results," *Experimental Thermal and Fluid Science*, vol. 1, pp. 3–17, 1988.

[111] I. Gertsbakh, *Measurement Uncertainty: Error Propagation Formula*, pp. 87–94. Berlin, Heidelberg: Springer Berlin Heidelberg, 2003.

[112] S. Tavoularis, *Measurement in Fluid Mechanics*. Cambridge University Press, 2005.

[113] D. K. Tiederman and M. W. G., "Biasing correction for individual realization of laser anemometer measurements in turbulent flows," *Physics of Fluids*, vol. 16, pp. 2082–2088, 1973.

[114] A. Blake and M. Isard, *Active Contours*. London: Springer London, 1998.

[115] S. M. Soloff, R. J. Adrian, and Z.-C. Liu, "Distortion compensation for generalized stereoscopic particle image velocimetry," *Measurement Science and Technology*, vol. 8, no. 12, pp. 1441–1454, 1997.

[116] G.-Q. Li, L. Guo, Y. Wang, Q. Guo, and Z. Jin, "2D Vision Camera Calibration Method for High-precision Measurement," vol. 1, no. 1, pp. 99–103, 2012.

[117] C. E.Willert, *Topics in Applied Physics Volume 112*, vol. 112. 2007.

[118] J. Wijker, *Random Vibration in Spacecraft Structure Design*, vol. 1. New York: Springer, 2009.

[119] D. Karnopp, "Power Balance Methord for Nonlinear Random Vibration," *Journal of Applied Mechanics*, vol. 1, pp. 212–214, 1967.

[120] Z.-J. Long, S.-K. Lee, J.-H. Jeong, and S.-J. Lee, "Study for the Safety of Ships' Nonlinear Rolling Motion in Beam Seas," *Journal of Navigation and Port Research International Edition*, vol. 33, no. 9, pp. 629–634, 2009.

[121] R. Barnoski, A. Piersol, W. V. D. Laan, P. White, and E. Winter, "Summary of Random VIbration Prediction Procedures.," tech. rep., NASA, California, 1969.

[122] R. E. Barrett, "Techniques for Predicting Localized Vibratory Environment of Rocket Vehicles.," Tech. Rep. October 1963, NASA, Huntsville, 1963.

[123] H. Himelblau, J. E. Manning, A. G. Piersol, and S. Rubin, "Dynamic Environment Criteria," tech. rep., NASA, Pasadena, 2001.

[124] T. Irvine, "Emperical Extrapolation of the acoustically-induced random vibraiton level from a reference vehicle to a new vehicle," 2009.

[125] T. Irvine, "Shock and vibration response spectra Unit 12," 2015.

[126] S. Ando and S. Qinzhong, "Extrapolation Technique for Acoustically Induced Random Vibration of Honeycomb Panel," *International Journal of Computer Science and Network Security*, vol. 6, no. 4, pp. 88–94, 2006.

[127] J. Archer and G. Jones, "Structural Vibration Prediction," tech. rep., NASA Langley Research Center, Hamptons, 1970.

[128] R. Ferebee, "Automation of vibroacoustic data bank for random vibration criteria development.," *The Journal of the Acoustical Society of America*, vol. 70, pp. 65–70, 1981.

[129] F. J. On and W. Hendricks, "Development of a vibroacoustic data base management and prediction system for payloads," in *The Shock and Vibration Bull*, pp. 53–64, 1982.

[130] R. Jewell, "A Technique for Predicting Localized Vibration Response in Rocket Vehicle Structure," in *Shock, V ibration, and Associated Environments Bulletin*, pp. 26–33, 1964.

[131] W. K. Blake, *Mechanics of flow-induced sound and vibration Volume I, General concepts and elementary sources.* Orlando: Academic Press, 1986.

[132] C. E. Taylor and M. J. Pettigrew, "Random Excitation Forces in Heat Exchanger Tube Bundles," *Journal of Pressure Vessel Technology*, vol. 122, no. 4, p. 509, 2000.

[133] F. Axisa, J. Antunes, and B. Villard, "Random Excitation of Heat Exchanger tubes by Cross-Flows," *Journal of Fluids and Structures*, vol. 4, pp. 321–341, 1990.

[134] C. Kirk, "Analysis of tazing induced vibraiton in aircraft by the power spectral density method.," Tech. Rep. 15, Air Force Flight Dynamics Laboratory, 1973.

[135] J. J. Wijker, M. H. M. Ellenbroek, and A. de Boer, "Characterization and Synthesis of Random Acceleration Vibration Specifications," in *4th ECCOMAS Thematic Conference on Computational Methods in Structural Dynamics and Earthquake Engineering*, no. June, pp. 1–22, 2013.

[136] C. Hartsuijker and J. W. Welleman, *Engineering Mechanics*. Dordrecht: Springer Netherlands, 2007.

[137] F. M. White, *Fluid Mechanics*. New York: McGraw-Hill Educaiton, 8 ed., 2016.

[138] H. S. Khatak and B. Raj, *Corrosion of Austenitic Stainless Steels: Mechanism, Mitigation and Monitoring*. New York: Woodhead Publishing Limited, 2002.

[139] V. L. Popov, *Contact Mechanics and Friction*. Berlin, Heidelberg: Springer Berlin Heidelberg, 2010.

[140] E. T. George and X. Lin, *Handbook of mechanical alloy design*. New York: Marcel Dekker, Inc., 2004.

Appendices

Appendix A

Free Stream Characteristics

Flow velocity profiles and turbulence intensities upstream of the tube bundle are measured using Laser Doppler Velociometry system. The velocity profiles at different location are plotted and suitable area where foreign objects should be placed is determined based on flow uniformity. Figures A.1a, A.1b, and A.1c shows the velocity profiles recorded at three transverse (Y) locations. The abscissa of the graph shows the mean component of velocity upstream of the tube bundle, whereas ordinate shows the Z position where velocity is measured. The least change in flow uniformity as $Tu\%$ changes, was recorded between 216 mm$\leq$ Z $\leq$ 256 mm as shown in these figures, and it was 1.8%, 6% and 7% respectively.

Turbulence intensities measured upstream of the tube bundle are shown in Figures A.2a, A.2b, and A.2c, respectively. Turbulence generated by the gird decays as it moves downstream from the grid [86]. This decay in the turbulence was measured by measuring the turbulence intensity at multiple location downstream of the grid. Figure A.3 shows the turbulence intensity recorded at multiple locations downstream of the grid. The abscissa

of the graph shows turbulence intensity and ordinate represents distance downstream from the grid. Using these graphs the turbulence intensity of the flow entering the tube bundle was calculated to be 7.5%.

PSD of streamwise component of upstream flow velocity shown in Figures A.4a, A.4b and A.4c, recorded at Tu = 2.0% and Re_D = 36,257, Tu = 7.5% and Re_D = 36,257, and Tu = 7.5% and Re_D = 42,682, respectively, shows absence of any major periodic content. Similarly, Figures A.5a and A.5b, shows no major periodic content in the PSD of cross-streamwise(Y) component of the velocity spectra recorded behind row 1 and row 2 of the tube bundle.

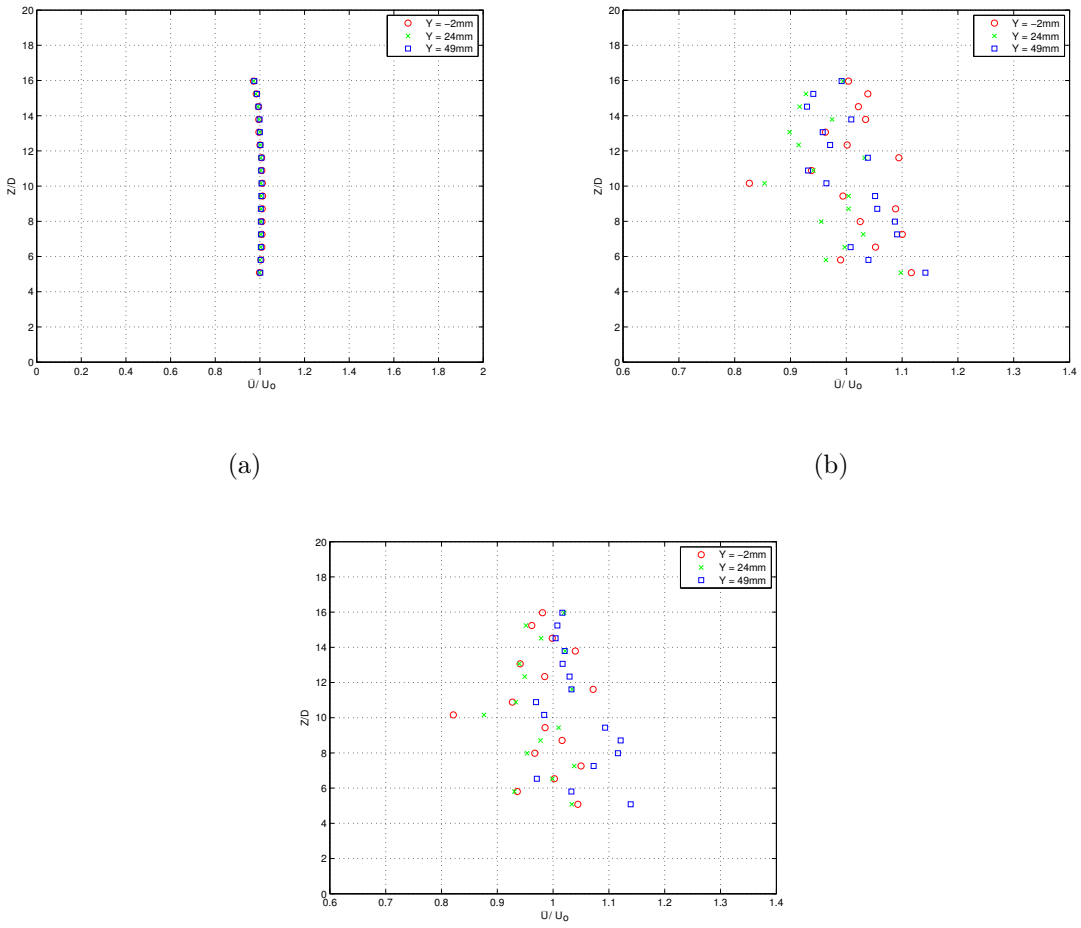

Figure A.1: Velocity profile upstream of tube bundle measured for at X = -127 mm for (a) Tu = 2.0% and Re_D = 36,257 (b) Tu = 7.5% and Re_D = 36,257 (c) Tu = 7.5% and Re_D = 42,682.

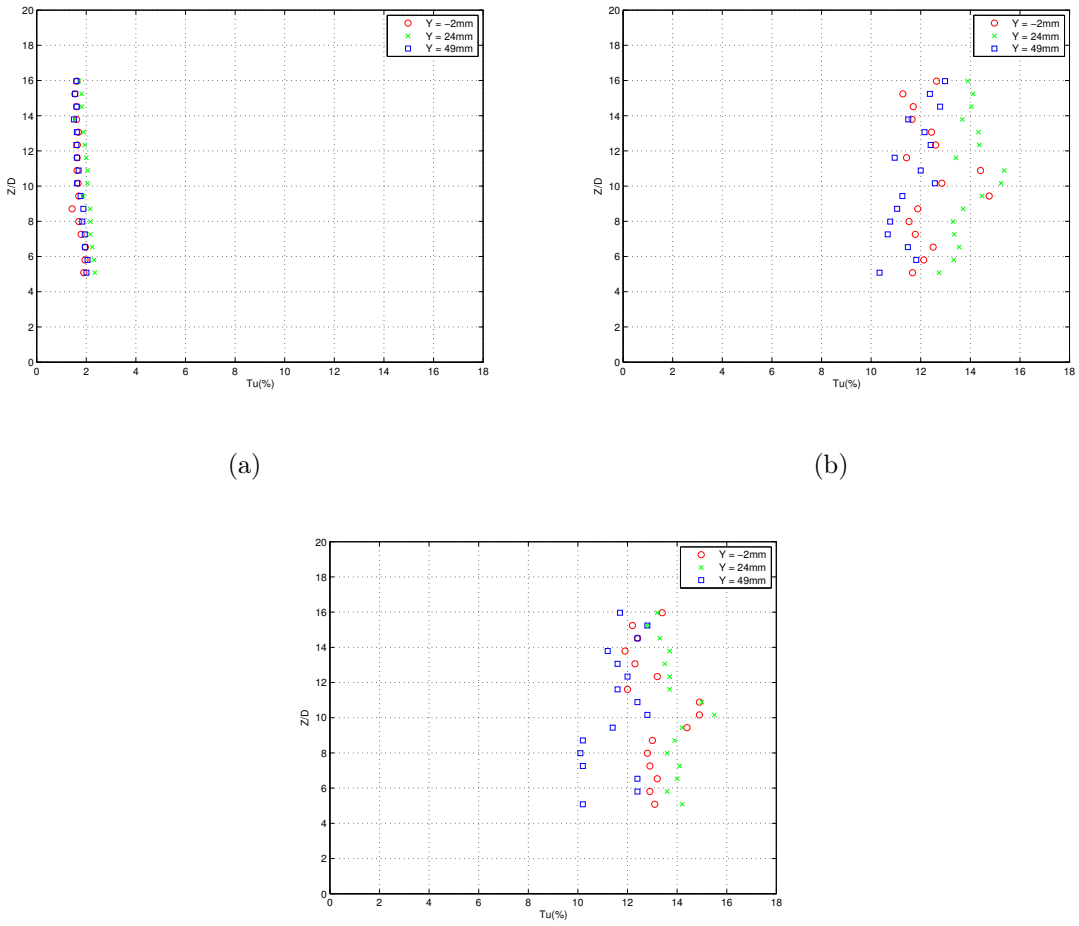

(a) (b)

(c)

Figure A.2: Turbulence intensities upstream of tube bundle measured at X = -127 mm for (a) Re_D = 36,257 (b) Re_D = 36,257 (c) Re_D = 42,682.

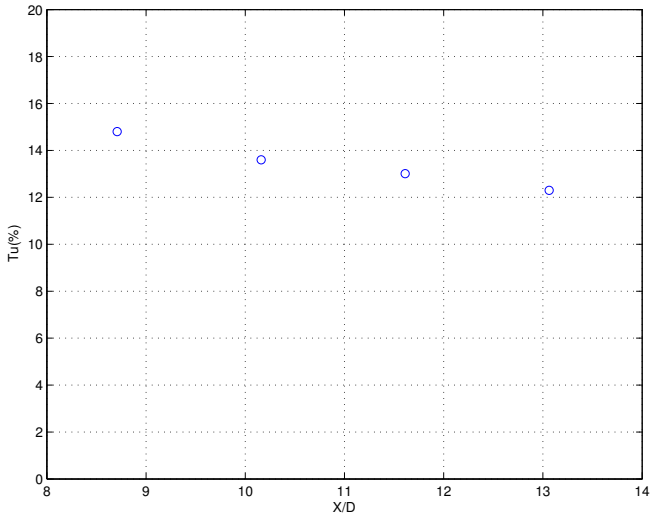

(a)

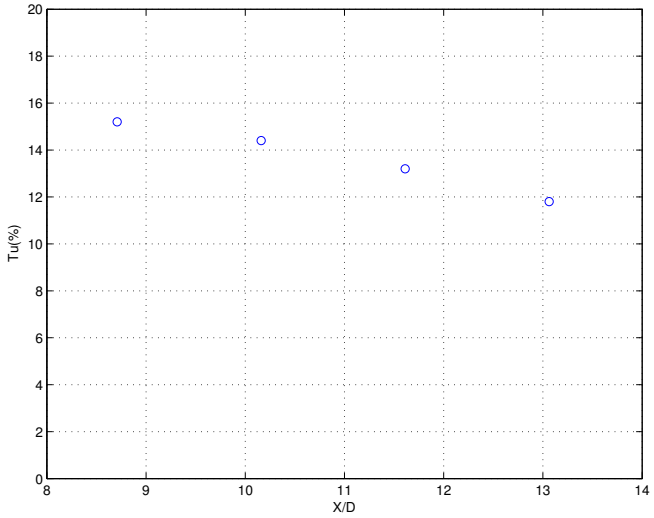

(b)

Figure A.3: Turbulence Intensity downstream of the grid (a) Re_D = 36,257 and (b) Re_D = 42,682.

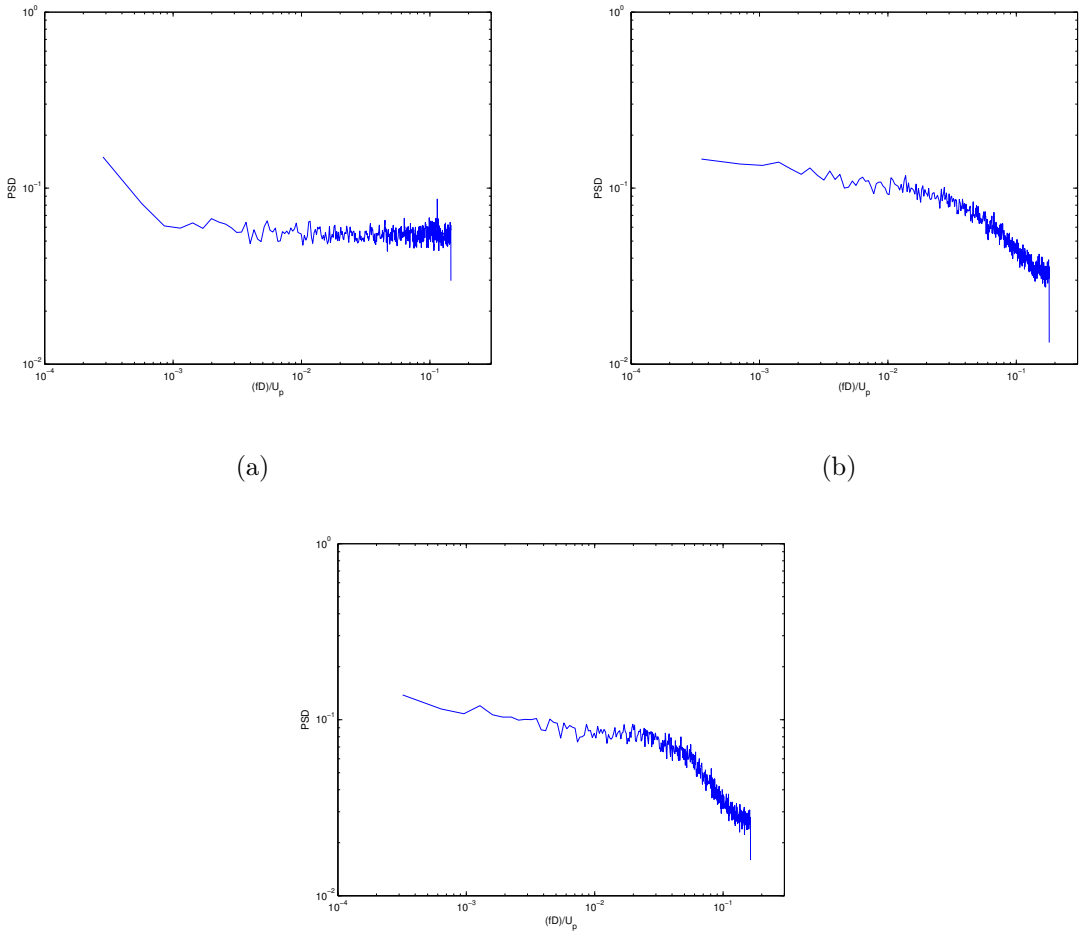

(a) (b)

(c)

Figure A.4: PSD upstream of tube bundle for streamwise upstream velocity component at (a) Tu = 2.0% and Re_D = 36,257 (b) Tu = 7.5% and Re_D = 36,257 (c) Tu = 7.5% and Re_D = 42,682.

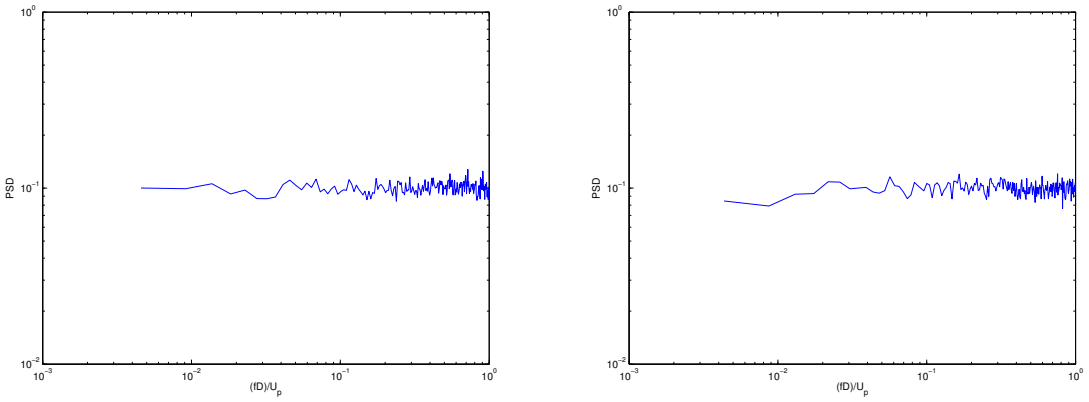

(a) (b)

Figure A.5: PSD inside of tube bundle for cross-streamwise velocity component when upstream Tu = 2.0% and Re_D = 36,257 measured (a) Behind row 1 (b) Behind row 2.

Appendix B

Experimental uncertainty

B.1 Dual Camera Set-up

The dual camera set-up gives the instantaneous three dimensional positions of the foreign object, from which the rms amplitude and sliding velocities are calculated. Uncertainty in estimating the instantaneous position of the foreign object using dual camera set-up is due to the contribution from multiple sources. In general, major sources of uncertainty are listed as follows: (i) Uncertainty introduced from approximating the true mapping polynomial by a two-dimensional third order polynomial (ii) Uncertainty due to the resolution of dual camera system (iii) Uncertainty introduced due to selecting the mapping polynomial from polynomial array using side camera, to estimate X and Y position (iv) Uncertainty due to vertical traverses while calibrating top camera.

Two dimensional third order mapping polynomial is used to map the objects position from image coordinates (u, v) to world coordinates (X, Y). The third order mapping

polynomial produces negligible errors, for images with less severe distortions [105]. The uncertanity associated with the mapping polynomial is related to the ability of the polynomial to accurately fit the data, and accuracy in locating centroid of the control points on the calibration grid [106, 107]. The rms uncertainty (u_m) associated with the two dimensional mapping polynomial is calculated by measuring the deviation between calculated and known positions of the control points on the calibration plate. The rms uncertainty (u_m) in the mapping function was estimated to be $\pm 0.04mm$.

Resolution of the image capturing system is another significant source of uncertainty. Side camera uses a scaling factor to estimate the Z position of foreign object. The spacial resolution for the side camera was calculated to be $0.1mm$. For the top camera, the dimensions of calibration grid in world coordinates and number of pixels between the grid points is used to calculate spacial resolution (u_K), which was estimated to be $0.1mm$. The uncertainty in estimating X, Y and Z position due to spacial resolution (u_K) is $\pm 0.05mm$. The uncertainty in determining the spacial resolution is due to error introduced during machining of the calibration plate and error associated with calculating the number of pixels between the grid points. However, the contribution from these two sources is an order of magnitude smaller and can be omitted from the current analysis.

Side-camera identify the mapping polynomial from polynomial array obtained during calibration of top camera, to determine X and Y position of the object. The uncertainty in choosing the mapping polynomial is limited by the resolution of the side camera in determining w coordinate of the foreign object centorid, which is $\pm 1pixel$. This can results in an uncertainty (u_p) of $\pm 0.03mm$, in estimating the X and Y position of the foreign object. Finally, the traverse system used to calibrate top camera do add to the measurement

uncertainty, but it is significantly smaller than the other uncertainty sources discussed in this section. Hence, its contribution is also omitted from the current analysis.

The uncertainty (u_X) and (u_Y) in determining the X and Y position of the foreign object is determined to be $\pm 0.07mm$ according to Equation B.1

$$u_X = u_Y = \pm\sqrt{(u_m)^2 + (u_K)^2 + (u_p)^2} \tag{B.1}$$

Uncertainty in estimating the instantaneous Z position of the foreign object is $u_Z = \pm 0.05mm$.

B.1.1 Uncertainty in RMS amplitude

The major sources of uncertainty in measuring RMS amplitude are listed as follows: (i) Uncertainty (u_N) in estimating the true RMS amplitude using data with limited sample size [108] (ii) Repeatability uncertainty u_{Repeat} [109]. The uncertainty in determining RMS amplitude is calculated as follows [110]:

$$u_{\delta Z_{RMS}} = \pm\sqrt{(u_N)^2 + (u_{Repeat})^2} = \pm\sqrt{\left(\frac{Z_{RMS}}{\sqrt{2(N-1)}}\right)^2 + (u_{Repeat})^2} \tag{B.2}$$

here, N is the number of samples in the time realization.

B.1.2 Uncertainty in wear time

Critical wear time (T) is calculated using volume removed (q_c), wear coefficient (K), normal force (F_n) and sliding velocity (S_v). The uncertainty in wear time is calculated as follows

[111]

$$u_T = \pm|T|\sqrt{\left(\frac{u_{q_c}}{q_c}\right)^2 + \left(\frac{u_K}{K}\right)^2 + \left(\frac{u_{F_n}}{F_n}\right)^2 + \left(\frac{u_{S_v}}{S_v}\right)^2} \tag{B.3}$$

here, since q_c and F_n are calculated theoretically, therefore the uncertainty is only due to K and S_v. Uncertainty in K is obtained from previous empirical studies and uncertainty in sliding velocity is calculated form in this section.

The sliding velocity S_v is calculated using sliding distance S_d during time t and is calculated as follows:

$$u_{S_v} = \pm|S_v|\sqrt{\left(\frac{u_{S_d}}{S_d}\right)^2 + \left(\frac{u_t}{t}\right)^2} \tag{B.4}$$

here, sliding distance (S_d) is measured experimentally. The major sources of uncertainty in measuring sliding distance are as follows: (i) uncertainty due to measuring system i.e. dual camera setup (ii) Repeatability uncertainty.

Uncertainty in calculating displacement in Z direction between two Z positions is estimated using Equation B.5

$$u_{\delta Z} = \pm\sqrt{(u_{Z_1})^2 + (u_{Z_2})^2} \tag{B.5}$$

this gives the uncertainty in calculating displacement in Z direction to be $u_{\delta Z} = \pm 0.07mm$. Similarly, the uncertainty in calculating the displacement in X and Y direction is obtained as $u_{\delta X} = \pm 0.10mm$ and $u_{\delta Y} = \pm 0.10mm$.

Total sliding distance in time t is calculated as the sum of multiple small displacements between discrete points from the time realization, the uncertainty is calculated using Equa-

tion (B.6) [109].

$$u_{\delta S_Z} = \pm\sqrt{(u_{\delta Z_1})^2 + (u_{\delta Z_2})^2 + (u_{\delta Z_3})^2 + ...(u_{\delta Z_n})^2} \tag{B.6}$$

An ensemble of four time realizations were recorded for each parameter that was varied giving the repeatability uncertainty (u_{Repeat}) in measuring sliding distance. Hence, total uncertainty associated with the sliding distance calculated is due the uncertainty measuring the sliding distance ($u_{\delta S_Z}$) and the uncertainty associated with the repeatability of the measurement (u_{Repeat}). The uncertainty in displacement is calculated as follows:

$$u_{S_d} = \pm\sqrt{(u_{\delta S_Z})^2 + (u_{Repeat})^2} \tag{B.7}$$

B.2 Laser Doppler Velocimetry

Multiple sources contributes towards the error associated with Laser Doppler Velocimetry (LDV), the most significant of which is the velocity bias [112]. For LDV measurements, the seeding particles crosses the probe volume randomly with different velocities. In a given time interval, a high velocity partial will crosses the probe volume more often than low velocity partial, resulting in a velocity bias. This is estimated using the equation proposed by McLaughlin and Tiedermann [113],

$$\frac{\bar{U}}{\bar{U_T}} \approx 1 + \frac{\bar{u^2}}{\bar{U}^2} \tag{B.8}$$

where $\bar{U}$ is the mean velocity measured using LDV, $\bar{U_T}$ is the true mean velocity and $\bar{u^2}$ is the variance associated with the velocity measured using LDV. Resampling the data at constant frequency results in reducing this velocity bias [113]. The bias error estimated after re-sampling the data ranges from 0 - 12 mm/s. The velocity biased error is negligible at low turbulence intensity, whereas high biased is estimated at higher turbulence intensity. According to manufacturer's specifications, the system has a repeatability error of 0.1% and an accuracy of 0.3%. The uncertanity u_t from velocity bias, accuracy and repeatability is calculated using the root-sum square method [110]

$$u_t = \pm \left(\sum_{k=1}^{n} {u_k}^2 \right)^{1/2} \tag{B.9}$$

where u_k is the uncertainty form each source. The maximum error approximated using equation (B.9) is less then 3.0%.

Additional errors are introduced due to variable particle size, fringe divergence and mounting the system at an angle. The mean seeding particle size is 10 μm and is expected to vary from $0 - 20\mu m$. This would result in an slight over prediction of the RMS velocity. In addition, for LDV measurements there is a possibility of error associated due to fringe divergence [113]. For the dual beam MSE miniLDV system, used in the present experimental set-up, the optics inside the laser system ensures that the two beams stay parallel and crosses at the same plane. Hence, the fringes will stay parallel, resulting in negligible fringe divergence error. In addition, digital level was used to ensure that the system is mounted within $\pm 0.1^o$ of horizontal. Therefore, uncertainty introduced due to these sources are assumed to be negligible.

Appendix C

Dual Camera Measurement System

This section employs a dual camera technique that maps the position of foreign object from image coordinate system (u,v,w) to world coordinate system (X,Y,Z), as shown in Figure C.1. Here, (u_o,v_o,w_o) and (X_o,Y_o,Z_o) are the coordinates of reference point in image and world coordinate system. The methodology followed in this section is presented in Figure C.2. Side camera uses the scaling factor (S_f) obtained from camera calibration, to map the w position of the foreign object form image coordinate system to Z position in the world coordinate system [114]. Top camera after calibration produces an array of two dimensional third order mapping polynomials used to map any point on uv plane to XY plane [115–117]. Based on the real time w position obtained from the side camera, the associated mapping polynomial is selected. The corresponding u and v coordinates obtained from the top camera image analysis are used as an input into the relevant mapping polynomial to obtain the respective X and Y coordinates of the foreign object. Details about calibration, image analysis and mapping for both side and top cameras is discussed

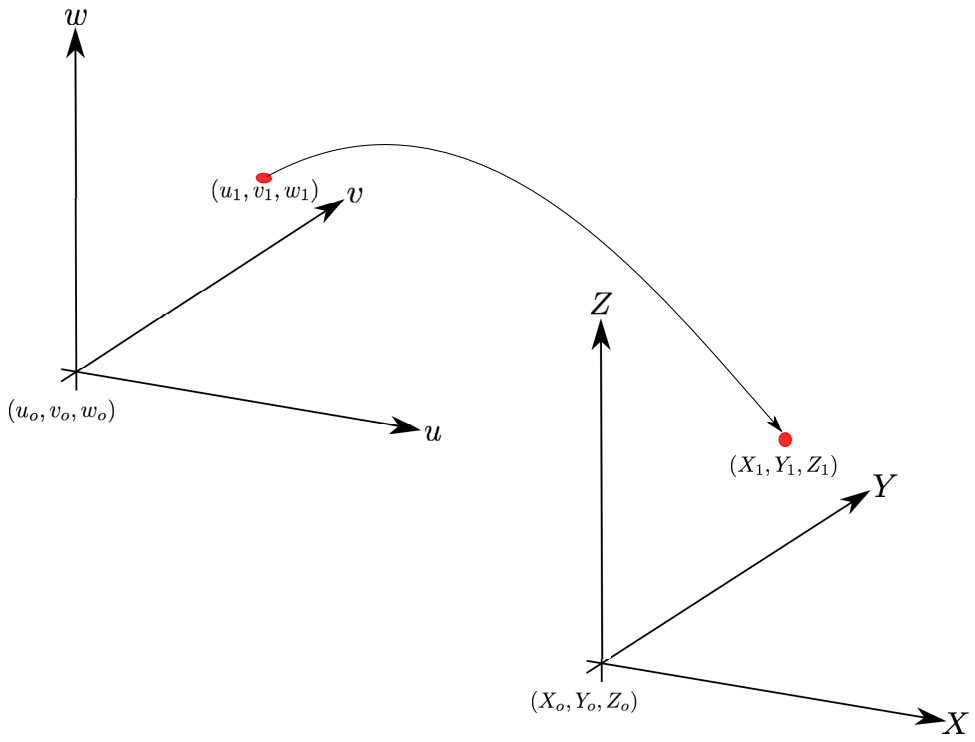

Figure C.1: Mapping from image coordinate system to world coordinate system.

in detail in this section.

Side camera as discussed in chapter 3 is placed outside the flume, with its optical axis perpendicular to the XZ plane. Side camera is calibrated using the calibration plate inserted into the tube bundle while the flume is running as seen in Figure C.3a. The calibration plate is viewed by the side camera through the gaps of width 3 mm. The view of calibration plate as seen through these gaps by the side camera is shown in Figure C.3b. This calibration plate consists of laminated graph paper with 5 mm grids attached to 2

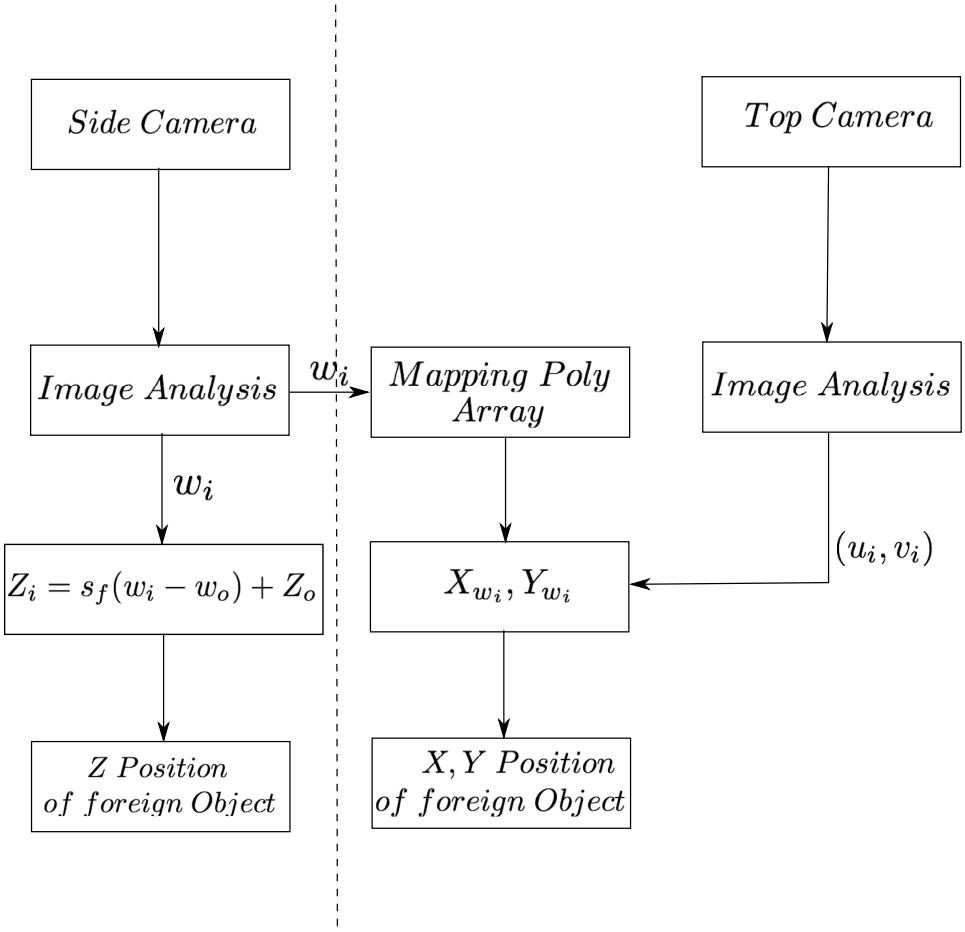

Figure C.2: Flow chart.

mm thick steel plate. Scaling factor (S_f) with units $mm/pixel$ was obtained as follows:

$$S_f = \frac{Z_1 - Z_o}{w_1 - w_o} \tag{C.1}$$

where, Z_1 and Z_o are the Z positions of the points on the calibration grid, while w_1 and w_o are the corresponding w positions of the the same points in image coordinates.

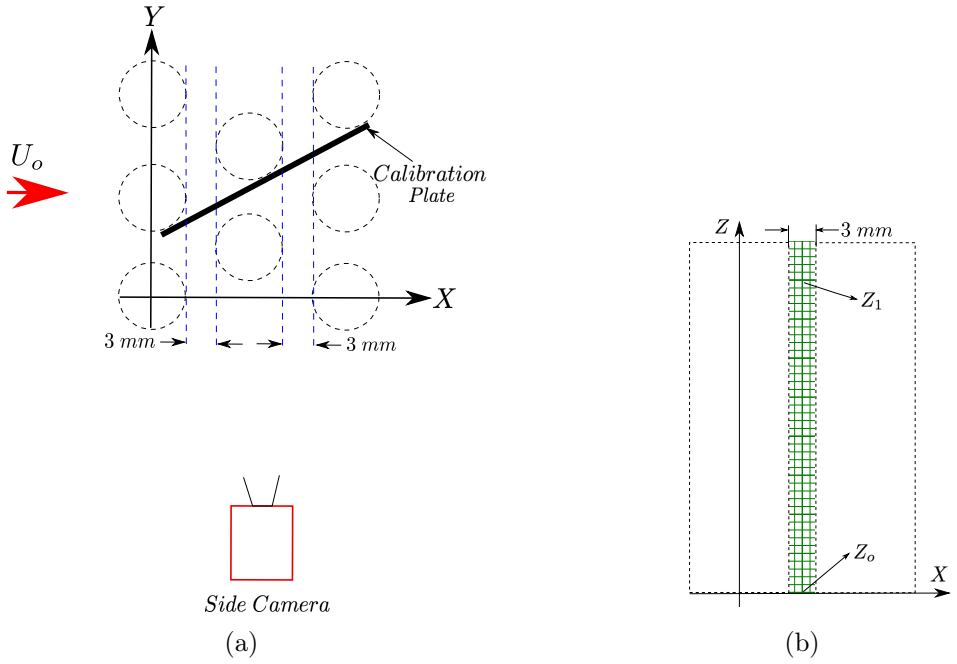

Figure C.3: Side camera calibration (a) Top view Schematic (b) Calibration plate in gap g_1.

Foreign object is marked with white markers as shown in Figure C.4a. The motion of the foreign object is tracked by tracking the movement of these markers on the object. The view of these marker on the foreign object as seen from the side camera is shown in Figure C.4c. Each time realization of foreign object inside tube bundle contains a set of 7127 images obtained at 150 Hz. Each image obtained from the side camera shows marker M_1 and M_2 on the foreign object visible through the tube bundle gaps as shown in Figure C.4c. The image coordinate w associated with the marker is obtained by calculating the centroid of these markers during image analysis [115]. The centroid w_i associated with the marker obtained from the i^{th} image is used in the following equation to obtained the Z

position:

$$Z_i = S_f(w_i - w_o) + Z_o \tag{C.2}$$

Top camera is calibrated using calibration plate with doted gird consisting of dots with 2.00 mm diameter shown in Figure C.5a. The distance between two adjacent dots was 5.00 mm, with position precision of ± 0.5 μm . The calibration plate is placed parallel to XY plane and is imaged at five Z positions 10 mm apart form each other (i.e. Z = 0, 10, 20, 30 and 40 mm) as shown in Figure C.5b, the corresponding w position of the planes in image coordinate system is recorded from the side camera. For each gap and at every w_i position, top camera calibration require the world (X, Y, Z) and image (u, v, w) coordinates of 16 control points $(d_1, d_2, ..., d_{16})$ as the calibration plane under goes a known translation from w_o to w_n. Each control point on the calibration grid underwent known translation motion, for example point d_1 shown in Figure C.5c, went from position (u_o,v_o,w_o) to position (u_n,v_n,w_n). The u and v values of intermediate locations of d_1 i.e. for its $w_o \leq w_i \leq w_n$ are obtained using linear interpolation as follows:

$$\frac{u - u_o}{u_n - u_o} = \frac{v - v_o}{v_n - v_o} = \frac{w - w_o}{w_n - w_o} \tag{C.3}$$

by implementing the above equation, u and v coordinates of all control points $d_1, d_2, ..., d_{16}$ at every $w_o \leq w \leq w_n$ are obtained.

Once the (u,v) coordinates of all the control points $(d_1, d_2, ..., d_{16})$ for all $w_o \leq w_i \leq w_n$ is calculated. The array of coefficients $(a_1, a_2, ..., a_{10})$ and $(b_1, b_2, ..., b_{10})$ for mapping polynomial shown in Equation C.4 and C.5 respectively are calculated for $w_o \leq w_i \leq w_n$.

(a)

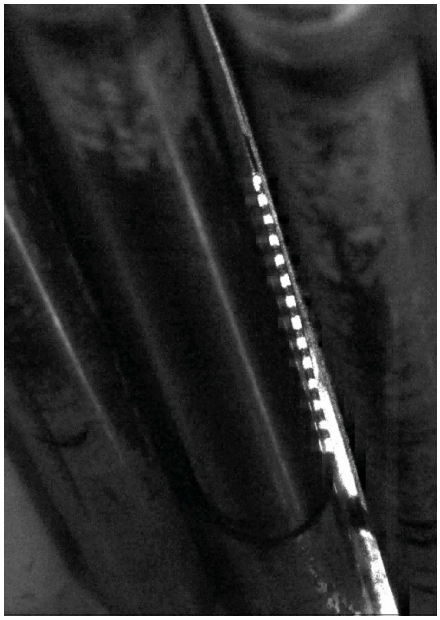

(b)

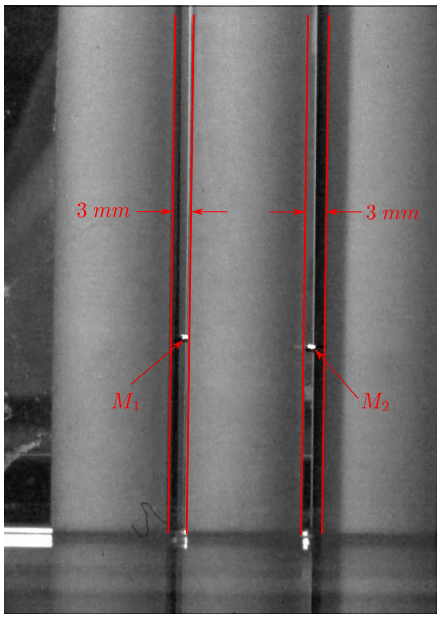

(c)

Figure C.4: Foreign object placed inside tube bundle (a) White markers painted on Foreign object (b) Top Camera and (c) Side Camera.

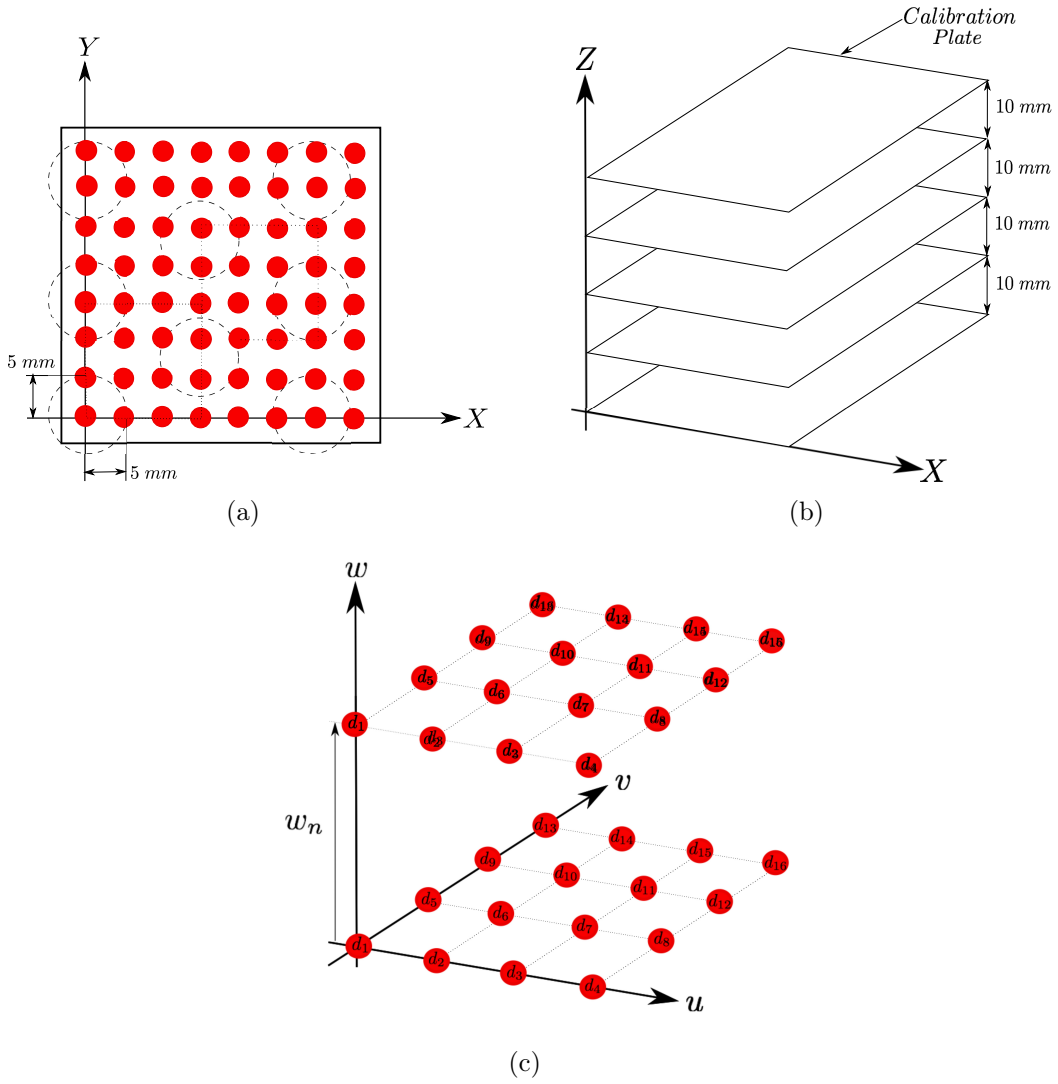

Figure C.5: Calibration of Top camera (a) Calibration Plate (b) Five images of Calibration Plate at known Z locations (b) Calibration Plate translation motion in image coordinates.

For $w = w_i$ location of the measurement volume, the relationship between (u,v) and (X,Y) is established by using the following third order mapping polynomial:

$$X_{w_i} = a_1 + a_2u + a_3v + a_4u^2 + a_5v^2 + a_6uv + a_7u^3 + a_8v^3 + a_9u^2v + a_{10}uv^2 \qquad \text{(C.4)}$$

$$Y_{w_i} = b_1 + b_2u + b_3v + b_4u^2 + b_5v^2 + b_6uv + b_7u^3 + b_8v^3 + b_9u^2v + b_{10}uv^2 \qquad \text{(C.5)}$$

here coefficients of the polynomial are obtained based on the coordinated of the control points on the calibration grid using least square method.

Image analysis for the top camera is done on the 7127 images recorded at 150 Hz for every time realization. For i^{th} image, Figure C.4b show the foreign object as seen by the top camera. Masking function is used to located both gaps on the top camera images as shown in Figure C.6. The centroid position (u_i, v_i) for both markers located in both gaps are obtained and its respective w_i position is obtained from the side camera. For this $w = w_i$ location of foreign object, the relationship between (u, v) and (X, Y) is established by using the corresponding third order mapping polynomial from equation C.4 and C.5.

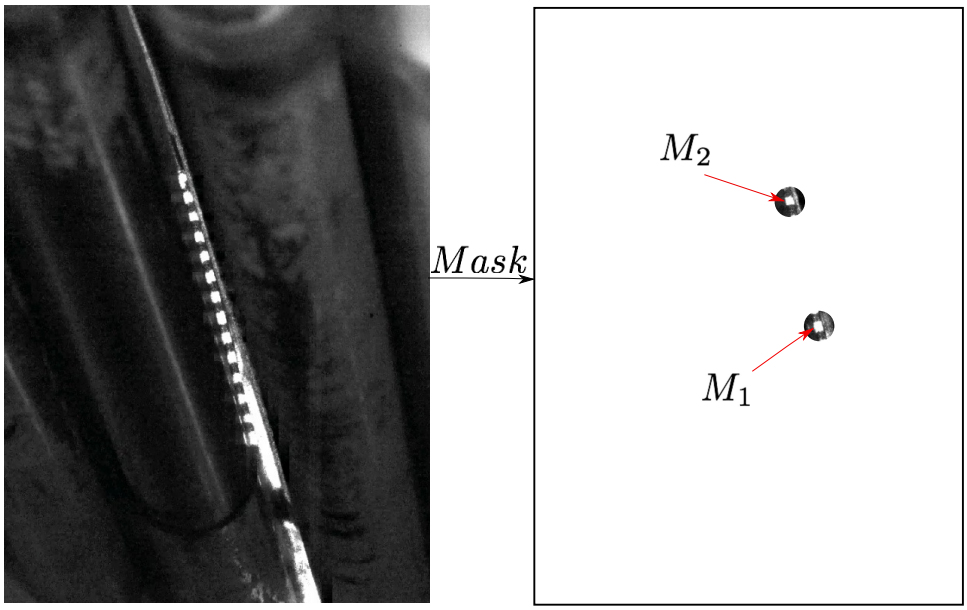

Figure C.6: Masking top camera images.

Appendix D

Sliding Velocity

Let the tubes be divided into n number of equal areas of width (M) as shown in Figure D.1a. For foreign object vibrating against tube bundle tube, certain areas of tube experience continuous contact (i.e., foreign object while vibrating will always be in contact with those areas) while other areas experience discontinuous contact (i.e. foreign object goes in and out of contact). For tube areas that are in continuous contact, the sliding distance experience by i^{th} area (A_i) is obtained directly from the discrete displacement time realization as follows:

$$S_d(A_i) = \sum_{i=1}^{N} |Z_{i+1}(t) - Z_i(t)| \tag{D.1}$$

here, for current study each recorded time history has N = 7124 points recorded at 150 Hz.

For discontinuous contact [91], the number of crossings (r) experience by i^{th} area (A_i)

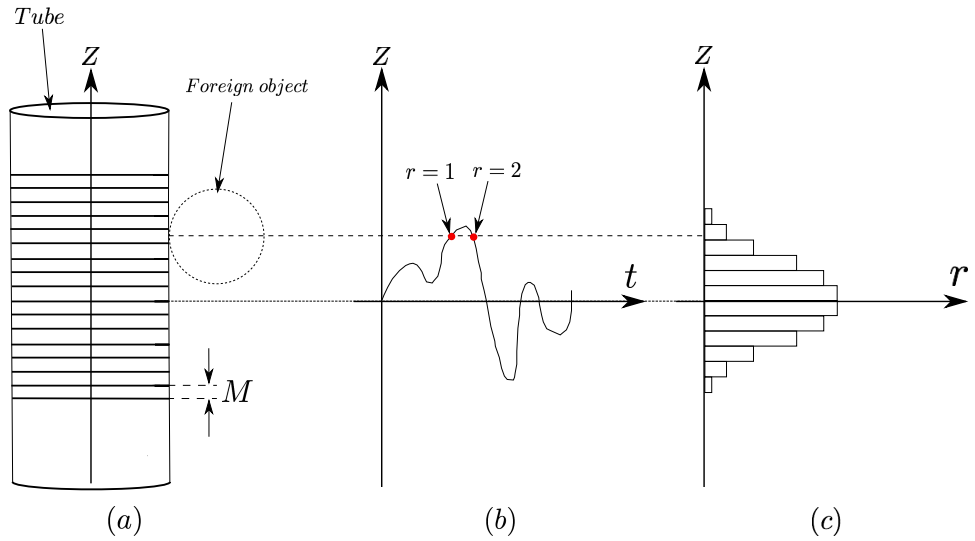

Figure D.1: Discontinues sliding contact due to foreign object vibration (a) Discrete areas of width M on tube bundle tube (b) Time history (c) Histogram of crossings (r) as a function of Z.

of the tube during the recorded time realization is calculated from the time realization as shown in Figures D.1b and D.1c. During every foreign object crossing, the tube area (A_i) experience sliding distance equal to the width of the contact area between tube and foreign object. The width ($M = 2b$) of the contact area, where b is the length of semi-minor axis of the ellipse calculated in Appendix K, is used to calculate the sliding distance as follows:

$$S_d(A_i) = rM \tag{D.2}$$

The sliding velocity experience by tube area (A_i) during each recorded time history is calculated as follows:

$$S_v(A_i) = \frac{S_d(A_i)}{(t)} \tag{D.3}$$

here, sliding distance is obtained form either equation D.1 or D.2, and t form current time history of foreign object(which is 47.5 seconds).

Appendix E

Extrapolating PSD & Estimate time realization

E.1 Extrapolation of PSD

Due to velocity constrains in the experimental facility, experiments were conducted at pitch velocity of 2 m/s ($Re_D = 36,257$) and 2.5 m/s ($Re_D = 42,682$). Wear due to foreign objects at higher flow velocities is estimated by extrapolating the sliding velocity of foreign object as a function of flow velocity. The response of foreign object at higher flow velocities is estimated from the response obtained experimentally and by utilizing extrapolation based on power balancing [118–120]. This method has been used previously to predict the response of structures based on the known response of a dynamically similar reference structure. [121–129].

Basis of this extrapolation method is that for any dynamic system undergoing steady

state or stationary vibration, the power input into the system is balanced by the power dissipated by the system [118–120]. Barret et al. [122] used this method to extrapolate the vibration response of rocket skin excited due to random acoustic pressure fluctuations. Ando & Qinzhong [126] showed that this extrapolation technique provides good predictions and, in some cases, gives better accuracy than the more complicated and time consuming Statistical Energy Analysis method. Frebee [128] and On & Hendricks [129] employed this approach to predict the response of new space vehicles based on the known response of dynamically similar structures. Jewell [130] used the power balancing technique method to predict the response in rocket vehicle structures.

The hook shaped foreign objects inside the tube-bundle behaves as a planar physical pendulum with movable pivot point, driven by dynamic pressure due to turbulence which is a power input source. The power dissipated by foreign object is mainly due to friction, which can be estimated from the measured dynamics of foreign object. Using the ratio of power balance equations for structure response at reference and new flow environment, equation (E.1), can be used to obtained the extrapolation function.

$$\frac{(P_{in})_{new}}{(P_{in})_{ref}} = \frac{(P_{out})_{new}}{(P_{out})_{ref}} \tag{E.1}$$

where P_{in} is power input into the vibrating structure and P_{out} is power dissipated by the vibrating structure. Since the PSD of pressure fluctuation inside tube bundle is known at various Reynolds number flow environment from previous empirical studies, the power input ($(P_{in})_{new}$ and $(P_{in})_{ref}$) to the structure can be estimated for both reference and new flow environment [13]. The power dissipated $(P_{out})_{ref}$ by the structure at reference flow

environment is estimated using the displacement PSD obtained experimentally. The power dissipated $(P_{out})_{new}$ by the structure at new flow environment is then estimated based on the known power input ratio $\left(\frac{(P_{in})_{new}}{(P_{in})_{ref}}\right)$ and known power dissipated $(P_{out})_{ref}$ of reference flow environment.

The power input due to randomly fluctuating pressure acting on foreign object is obtained by the following expression [118, 119, 131]:

$$P_{in} = \frac{\pi A_s^2}{M} \int_{f_a}^{f_b} \frac{G_{pp}(f)}{f_b - f_a} df \tag{E.2}$$

where G_{pp} is the random pressure power spectral density with lower and upper frequency bounds f_a and f_b, f is frequecney, A_s is the surface area of the foreign object and M is the mass of the foreign object. Equation E.2 requires random pressure power spectral density (G_{pp}) acting on foreign object logged inside tube-bundle at both reference and new pitch velocities conditions as an input. This expression is obtained from previous empirical studies which provides pressure power spectral density (G_{pp}) inside tube-bundle periphery at various flow conditions. Belvin [14] and Pettigurw [132] proposed an empirically derived expression for the random pressure PSD inside tube bundle to calculate the random vibration response of steam generator tubes. Axisa et el. [133] in their study on normal rectangular and normal triangular tube bundle geometry found the reduced force spectrum to be independent of the tube geometry for single phase cross flow. Au-yang [13] combined available data from previous empirical studies and proposed the following expression for

estimating pressure power spectral density in tube array periphery:

$$G_{pp}(F) = \frac{1}{4}\rho^2 {U_p}^3 D\bar{G_{pp}}(F) \tag{E.3}$$

where $\bar{G_{pp}}$ is normalized pressure power spectral density, U_p is the pitch velocity and D is the tube diameter. For tubes in upstream rows, the following values of $\bar{G_{pp}}$ is suggested,

$$\bar{G_{pp}} = \begin{cases} 0.01 & \text{for } F < 0.1 \\ 0.2 & \text{for } 0.1 \leq F \leq 0.4 \\ 5.3E-4/F^{7/2} & \text{for } F > 0.4 \end{cases}$$

where, F is the dimensionless frequency,

$$F = \frac{fD}{U_p} \tag{E.4}$$

Rate of work done by friction force gives the following expression for power dissipated by randomly vibrating foreign object [134]:

$$P_{out} = \sqrt{8\pi} N_f \sqrt{\int_{f_a}^{f_b} f^2 G_{ZZ}(f) df} \tag{E.5}$$

where N_f is the friction force, f is frequency and G_{ZZ} is the displacement power spectral density with lower and upper frequency bounds f_a and f_b. The reference function for G_{ZZ} used in equation (E.5) is obtained empirically.

Substituting equation (E.5), (E.2) and (E.3) into equation (E.1) and simplifying it gives

the following equation relating new and reference displacement PSD:

$$(G_{ZZ}(f))_{new} = (G_{ZZ}(f))_{ref} \frac{(U_p)_{ref}}{(U_p)_{new}} \tag{E.6}$$

Finally, the frequencies within the frequency bound f_a to f_b of the displacement power spectral density are extrapolated as follows [126, 129].

$$f_{new} = f_{ref} \left(\frac{(U_p)_{new}}{(U_p)_{ref}} \right) \left(\frac{d_{ref}}{d_{new}} \right) \tag{E.7}$$

where, d is diameter of wire samples or width of plate samples.

E.2 Estimate time realization

So far the displacement PSD (G_{ZZ}) of the foreign object is extrapolated, but the goal of this appendex is to estimate the corrosponding time realizationa and use it in Appendix D to estimate sliding velocity. This is accomplished by using the extrapolated displacement PSD to estimate time realization through the method proposed by Irvine [125] and Wijker et al. [135]. The amplitudes and associated frequencies obtained from the displacement PSD (G_{ZZ}) are substituted into the following equation to estimate the time realization:

$$Z(t) = \sum_{i=1}^{n} A_i sin(2\pi f_i t + \phi_i) \tag{E.8}$$

where, $Z(t)$ is the time realization function, n is the number of frequencies, f is the frequency of the vibrating system, ϕ is the phase and A is the vibrating amplitude of

the associated frequency. The phase is assumed to be a random variable with uniform distribution. This new time realization exhibits the same statistical characteristics i.e. Kurtosis, skewness, probability density function etc as the reference time realization. From the extrapolated time realization, the sliding velocity is calculated in Appendix D and finally, the wear time to reach 40% of the tube wall thickness at higher pitch velocities is obtained.

Appendix F

Bending analysis

The maximum deflection (Δ_{max}) experienced by foreign object was calculated assuming that simply supported foreign object was in cross flow orientation to the flow as can be seen in Figure F.1a [136]. The deflection experienced by foreign object when the yaw angle is 180 degree should be largest since the foreign object will experience largest drag force distribution (l) in this configuration.

Second moment of area (I) is calculated as follows:

For wire with cross-section shown in Figure F.1c:

$$I = \frac{\pi}{4}\left(\frac{d_w}{2}\right)^4 \tag{F.1}$$

For Plate with cross-section shown in Figure F.1b:

$$I = \frac{d_p h_p^3}{12} \tag{F.2}$$

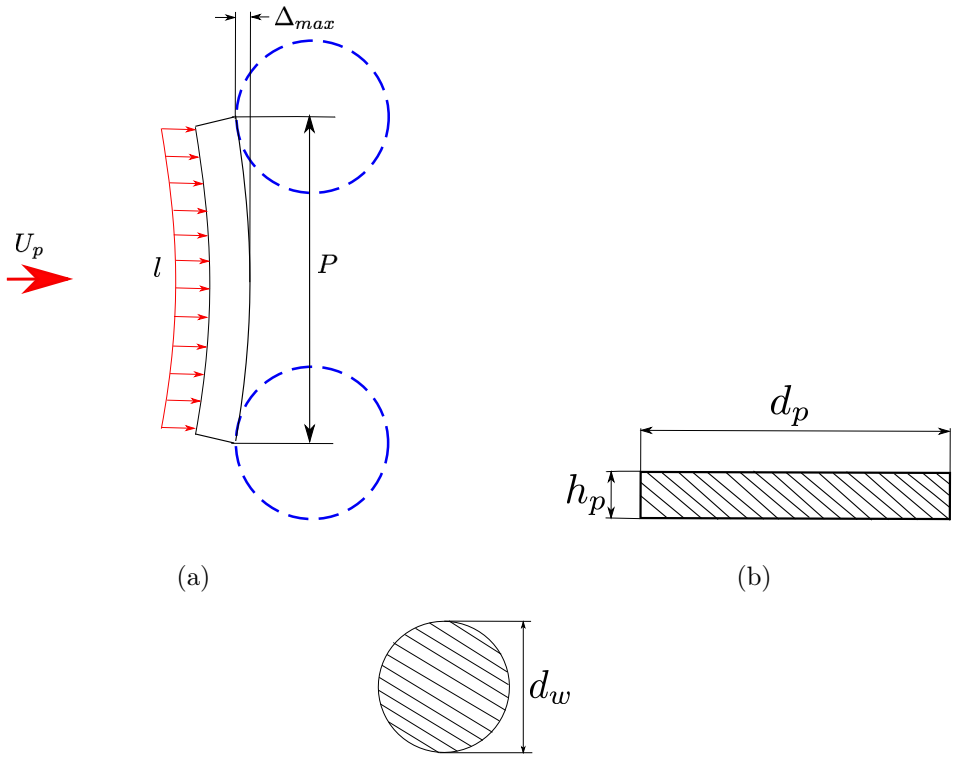

Figure F.1: Simply supported beam deflection due to distributed load (a) Schematic of Foreign object deflection. (b) Plate cross-section. (c) Wire cross-section.

Reynolds number (Re_d) was calculated using the following equation:

$$Re_d = \frac{\rho U_p d_{(w\ or\ p)}}{\mu} \tag{F.3}$$

Front area (O_r) for wire and plate samples is calculated as follows:

$$O_r = (d_{(w\ or\ p)})(P) \tag{F.4}$$

The distributed drag force (l) on the body was calculated as follows:

$$l = \frac{\frac{1}{2} C_d \rho U_p^2 O_r}{P} \tag{F.5}$$

where, the drag coefficient is obtained form the literature based on the foreign object Reynolds number [137].

Finally, the maximum defection experienced by simply supported foreign object is calculated as follows:

$$\Delta_{max} = \frac{5 l P^4}{384 E I} \tag{F.6}$$

The pitch velocity experience by foreign object ranges between 2.5 m/s to 8.0 m/s. The deflection experienced by foreign object should be maximum when the pitch velocity is 8 m/s and the yaw angle is 180 degrees (i.e cross flow orientation). Using the constant summarized in Table F.1 and the methodology presented above, the maximum deflection is calculated and is presented in Table F.2. For this results, it can be deducted that even in this extreme case scenario, both wire and plate samples experience negligible deflection and can be considered as rigid object inside tube bundle.

Table F.1: Constants for foreign object bending analysis

Constants	Wire	Plate
$d_w\ (m)$	0.0012	-
$d_p\ (m)$	-	0.0046
$h_p\ (m)$	-	0.0005
$P\ (m)$	0.0236	0.0236
$E\ (GPa)$ [138]	193	193
C_d [137]	1.2	2
$\rho\ (Kg/m^3)$ [137]	998.2	998.2
$\mu\ (Pa.s)$ [137]	0.0012	0.0012
$U_p\ (m/s)$	8	8

Table F.2: Maximum deflection experienced by simply supported Foreign object

	Wire (10^{-6} m)	Plate (10^{-3} m)
Max deflection(m)	9.5	0.1

Appendix G

Statistical Properties

Mean and RMS

Random time realization recorded for time interval T is shown in Figure G.1. For discrete displacement time realization (containing $N = 7127$ points) recorded during the experiments, the mean can then be obtained as follows:

$$\bar{A}_Z = \frac{1}{N} \sum_{n=1}^{N} Z(t_n) \tag{G.1}$$

Data with mean removed:

$$Z_o(t_n) = Z(t_n) - \bar{A}_Z \tag{G.2}$$

Standard deviation of the data can be obtained as follows:

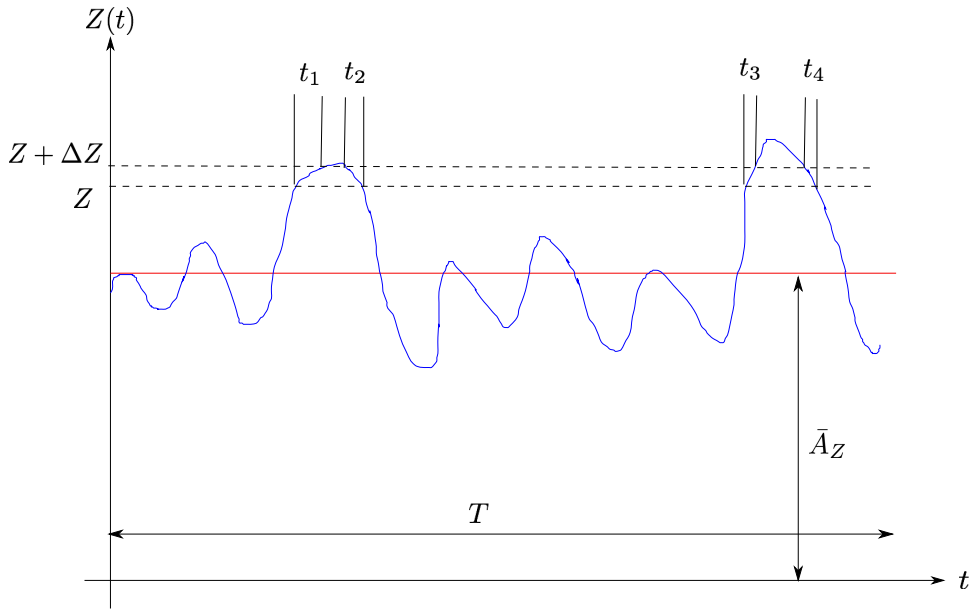

Figure G.1: Random time history.

$$A_{RMS,Z} = \sqrt{\frac{1}{N}\sum_{n=1}^{N}(Z_o(t_n))^2} \tag{G.3}$$

Autocorrelation

Autocorrelation gives the correlation of the time realization with itself at different time delay τ. This autocorrelation of a time realization gives an indication of the time interval over which the data is correlated. For a discrete time realization with N points separated by interval ΔT, for $\tau = m\Delta T$, autocorrelaiton can be obtained as follows:

$$R_{ZZ}(\tau) = \frac{1}{N-m}\sum_{n=1}^{N-m} Z_o(t)Z_o(t+\tau) \tag{G.4}$$

this can be done for different τ obtain the plots in chapter 4.

For continuous signal can be obtained as follows:

$$R_{ZZ}(\tau) = \lim_{T\to\infty} \frac{1}{2T} \int_{-T}^{+T} \mathrm{Z_o(t)Z_o(t+\tau)}\,\mathrm{d}t \tag{G.5}$$

Power Spectral Density (PSD)

Power spectral density gives the indication of frequency content associated with random signal. Fourier transform of autocorrelation gives the Power Spectral Density:

$$S_{ZZ}(\omega) = \lim_{T\to\infty} \frac{1}{2\pi} \int_{-T}^{+T} R(\tau)\mathrm{e}^{-i\omega\tau}\,\mathrm{d}\tau \tag{G.6}$$

Here, $S_{ZZ}(w)$ is two sided PSD as a function of angular frequency. This can be expressed as single sided PSD as a function of frequency as follows:

$$G_{ZZ}(f) = 4\pi S_{ZZ}(\omega) \tag{G.7}$$

The area under the curve of power spectral density, gives the mean square value $(A_{RMS,Z})^2$ of the random signal.

Probability Density

For a time signal seen in Figure G.1, to determine the percentage of time the random variable such as displacement of the foreign object exceeds a given value, a probability density function is required. Probability that $Z(t)$ lies between the interval Z and $Z + \Delta Z$ can be obtained as:

$$prob[Z < Z(t) < Z + \Delta Z] = \sum_i \frac{t_i}{T} \tag{G.8}$$

For a very small interval ΔZ, a probability density function can be defined as

$$prob[Z < Z(t) < Z + \Delta Z] = p(Z)\Delta Z \tag{G.9}$$

where,

$$p(Z) = \frac{\sum_i t_i}{T\Delta Z} \tag{G.10}$$

For very small ΔZ and very long time duration T, the probability density function can be written as:

$$p(Z) = \lim_{\Delta Z \to 0} \left[\lim_{T \to \infty} \left(\frac{\sum_i t_i}{T\Delta Z} \right) \right] \tag{G.11}$$

Quantile

Quantile in qq plot are points in the data below which a certain fraction or percentage of points falls. For example, in a 0 mean normally distributed data, the 0.5 quantile is 0, that is 50% or half of the data falls below 0.

Appendix H

Displacement Time Realizations

Figures H.1, H.2, H.3, and H.4, show the X, Y and Z amplitude response of point p on the wire type foreign object of length L/D = 2.8, 3.4, 4.0 and 4.6 at $Tu = 2.0\%$ and $Re = 36,257$, respectively. As can be seen in these figures, the Z amplitude response is relatively large compare to X and Y response for all L/D. Similarly, Figures H.5 and H.6, show the X, Y and Z amplitude response of point p on the plate type foreign object of length L/D = 3.4 and 4.0 at $Tu = 2.0\%$ and $Re = 36,257$, respectively. The Z amplitude response of plate samples, same as wire samples, is relatively large compared to its X and Y amplitude response.

Figures H.7, H.8, H.9, and H.10, show the X, Y and Z amplitude response of point p on the wire type foreign object of length L/D = 2.8, 3.4, 4.0 and 4.6 at $Tu = 7.5\%$ and $Re = 36,257$, respectively. The Z amplitude response of these wire samples is relatively large compared to its X and Y amplitude response. Compared to the amplitude repose of wire samples at $Tu = 2.0\%$ (as discussed in previous paragraph), these wire samples shows

reduction in peak-to-peak amplitude due to increase in Tu.

Figures H.11, H.12, H.13, and H.14, show the X, Y and Z amplitude response of point p on the wire type foreign object of length L/D = 2.8, 3.4, 4.0 and 4.6 at $Tu = 7.5\%$ and $Re = 42,682$, respectively. Similar to other flow environment, the Z amplitude response of wire samples is more dominant compared to X and Y amplitude response. Compared to Figures H.7,H.8, H.9, and H.10, the peak-to-peak response of wire samples increase with increase in Re. Figures H.15 and H.16, show the X, Y and Z amplitude response of point p on the plate type foreign object of length L/D = 3.4 and 4.0 at $Tu = 7.5\%$ and $Re = 42,682$, respectively. As can be seen in these graphs, the Z amplitude response of plate samples, same as wire samples, is relatively large compared to its X and Y amplitude response.

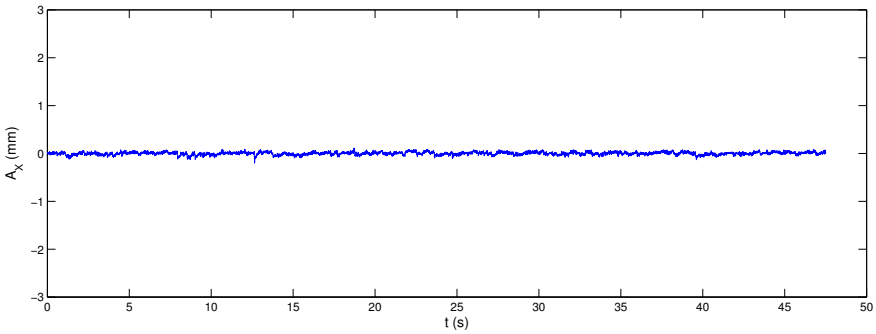

(a) X Displacement

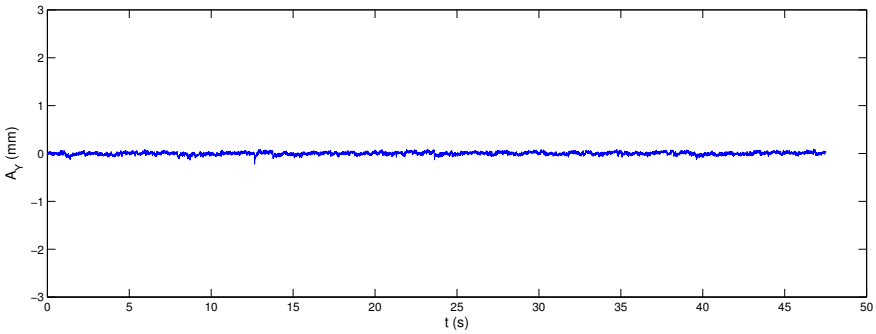

(b) Y Displacement

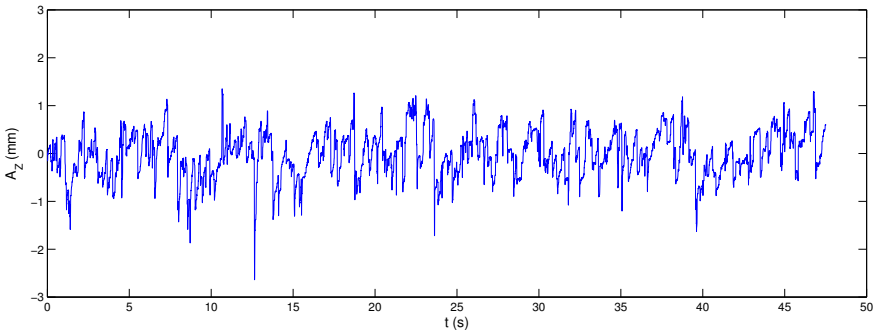

(c) Z displacement

Figure H.1: Displacement time realization of $L/D = 2.8$ wire sample at $Tu = 2.0\%$ and $Re = 36,257$.

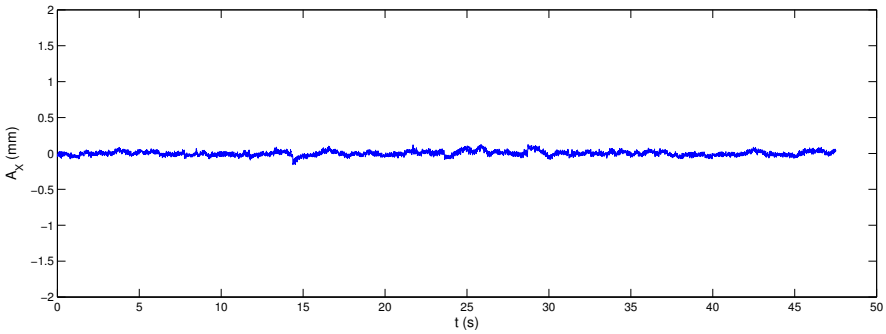

(a) X Displacement

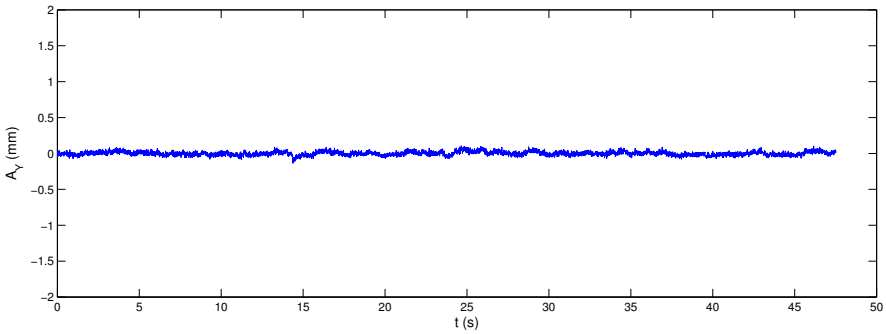

(b) Y Displacement

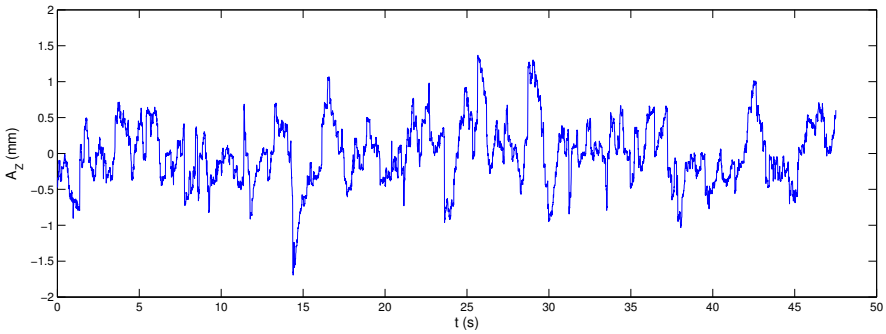

(c) Z Displacement

Figure H.2: Displacement time realization of $L/D = 3.4$ wire sample at $Tu = 2.0\%$ and $Re = 36,257$.

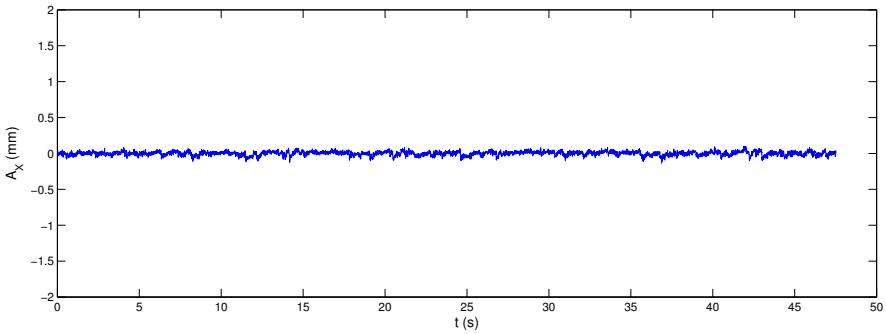

(a) X Displacement

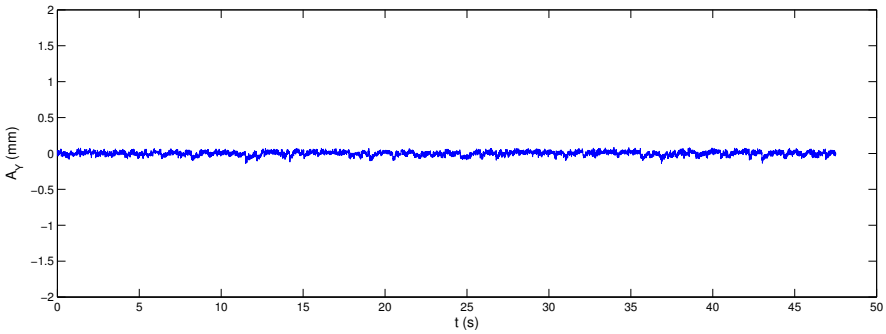

(b) Y Displacement

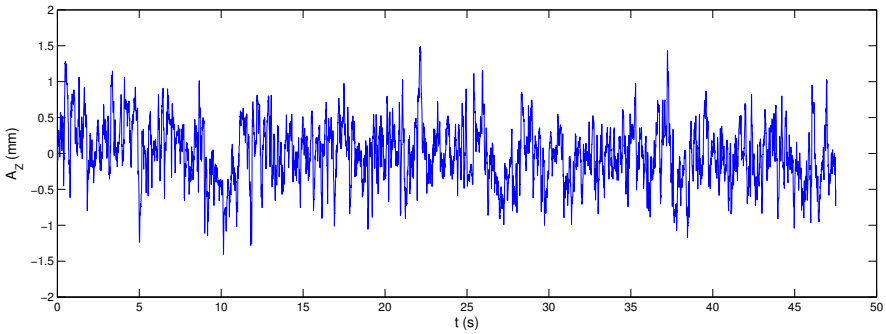

(c) Z Displacement

Figure H.3: Displacement time realization of $L/D = 4.0$ wire sample at $Tu = 2.0\%$ and $Re = 36,257$.

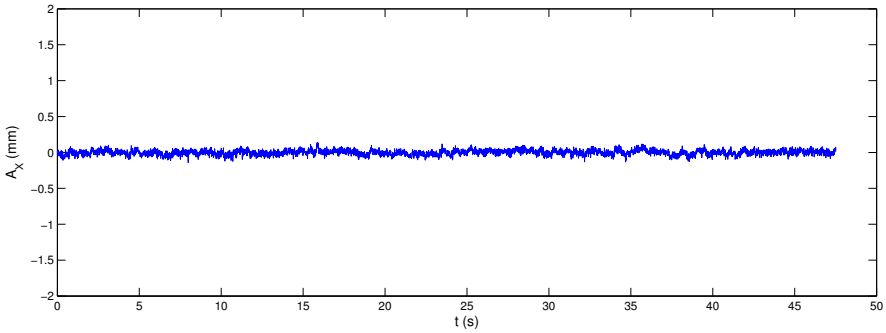

(a) X Displacement

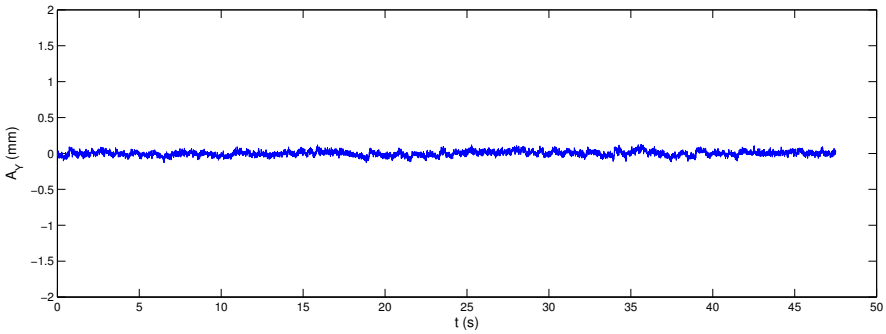

(b) Y Displacement

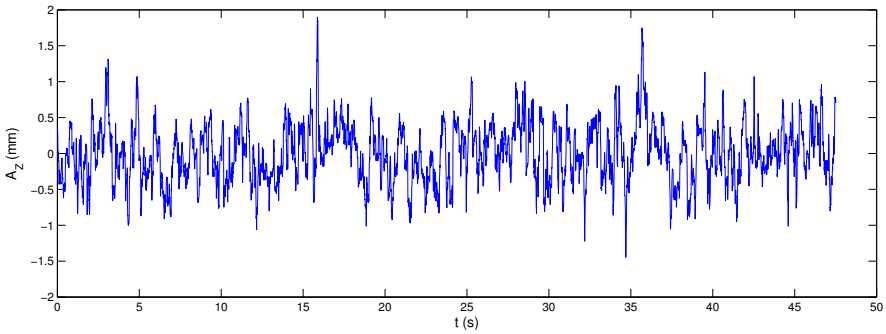

(c) Z Displacement

Figure H.4: Displacement time realization of $L/D = 4.6$ wire sample at $Tu = 2.0\%$ and $Re = 36,257$.

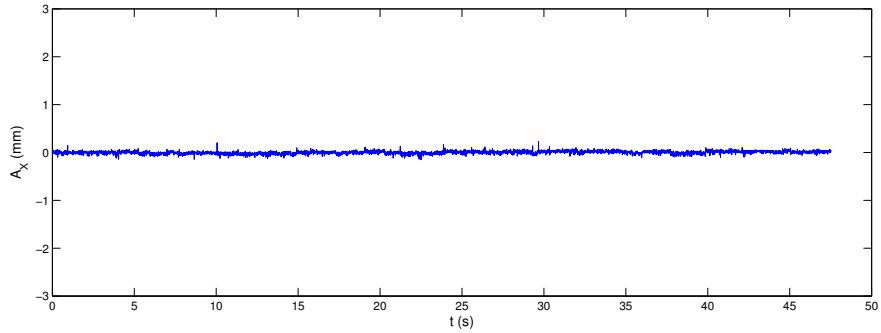

(a) X Displacement

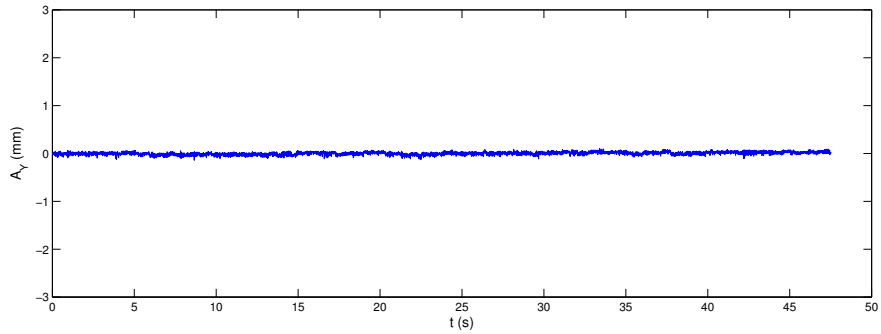

(b) Y Displacement

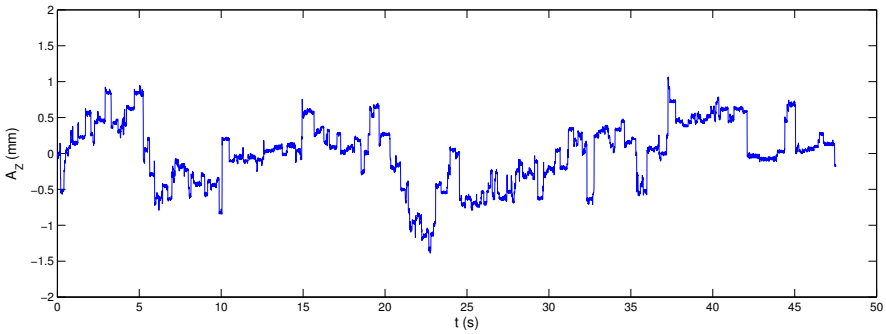

(c) Z Displacement

Figure H.5: Displacement time realization of $L/D = 3.4$ plate sample at $Tu = 2.0\%$ and $Re = 36,257$.

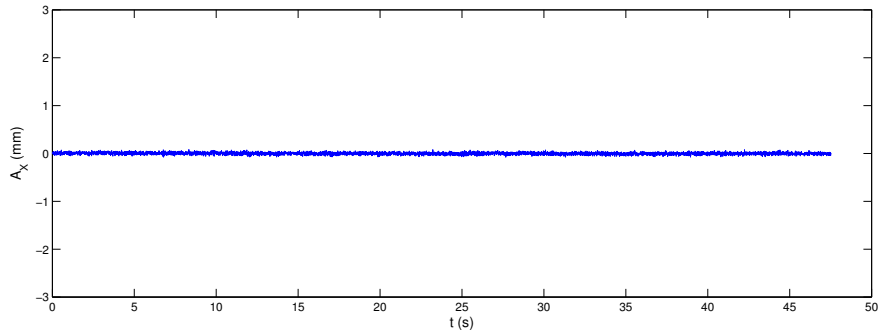

(a) X Displacement

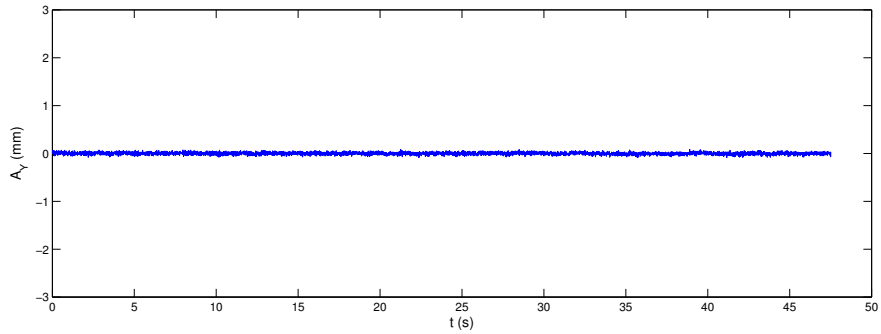

(b) Y Displacement

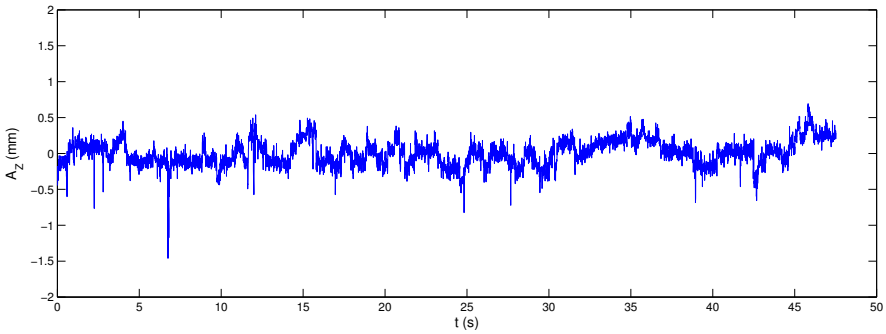

(c) Z Displacement

Figure H.6: Displacement time realization of $L/D = 4.0$ plate sample at $Tu = 2.0\%$ and $Re = 36,257$.

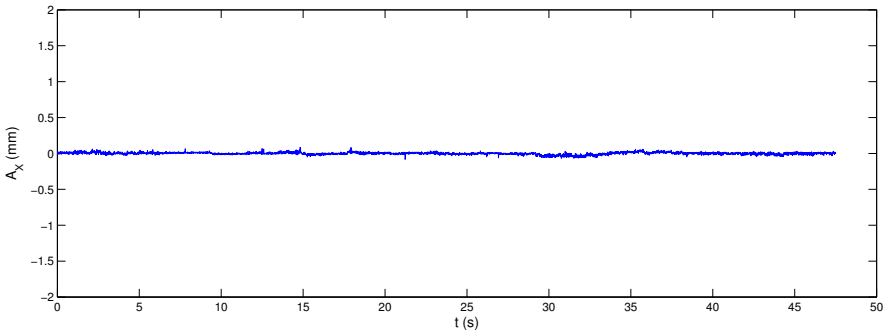

(a) X Displacement

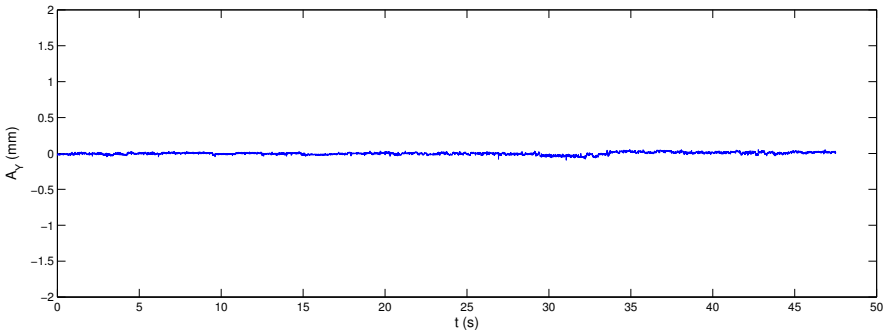

(b) Y Displacement

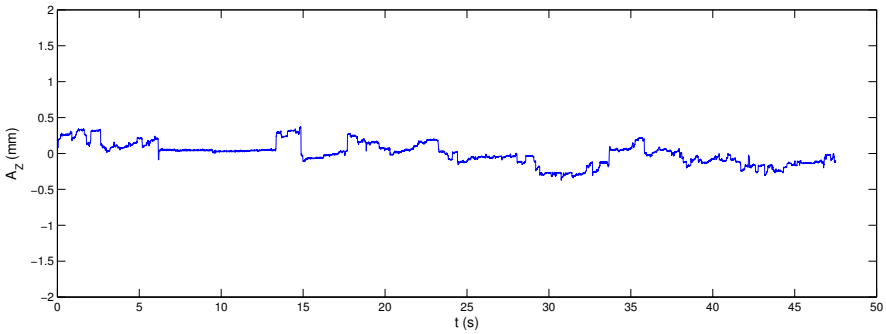

(c) Z Displacement

Figure H.7: Displacement time realization of $L/D = 2.8$ wire sample at $Tu = 7.5\%$ and $Re = 36,257$.

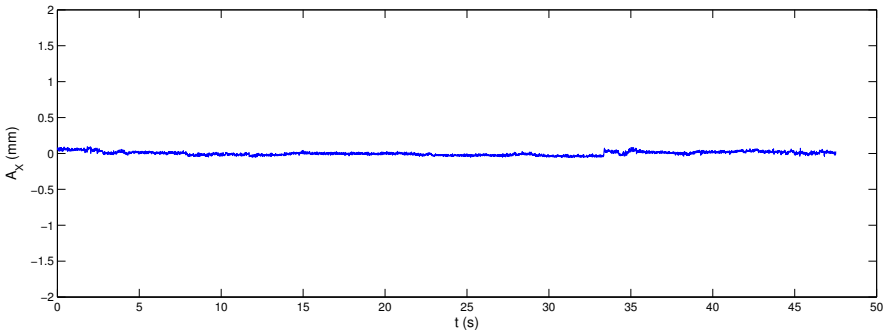

(a) X Displacement

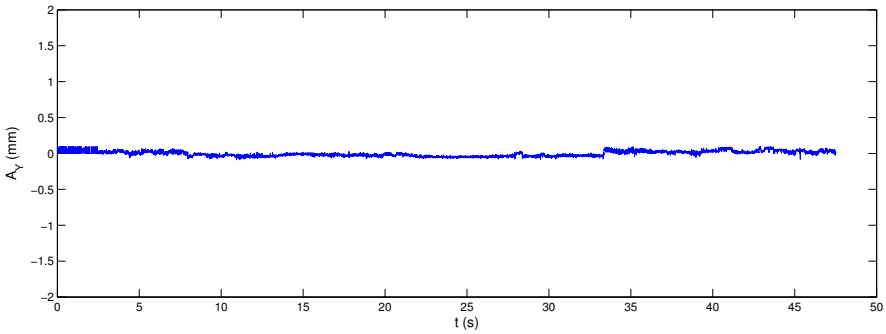

(b) Y Displacement

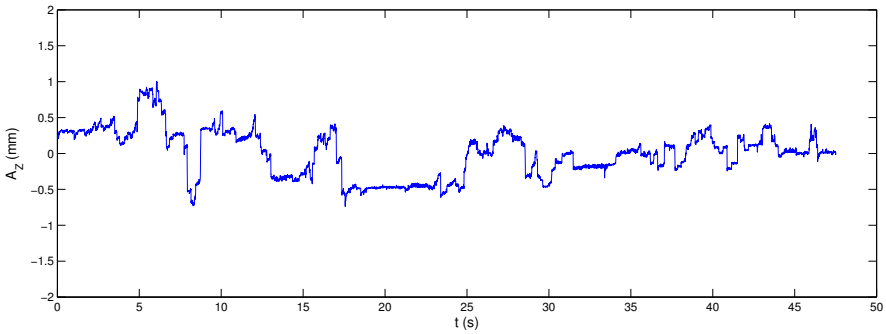

(c) Z Displacement

Figure H.8: Displacement time realization of $L/D = 3.4$ wire sample at $Tu = 7.5\%$ and $Re = 36,257$.

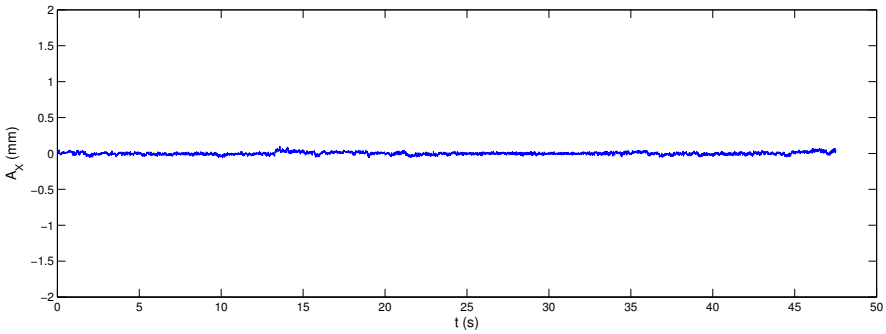

(a) X Displacement

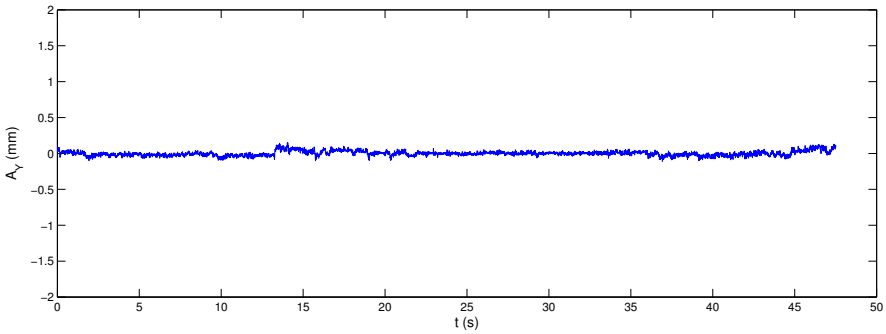

(b) Y Displacement

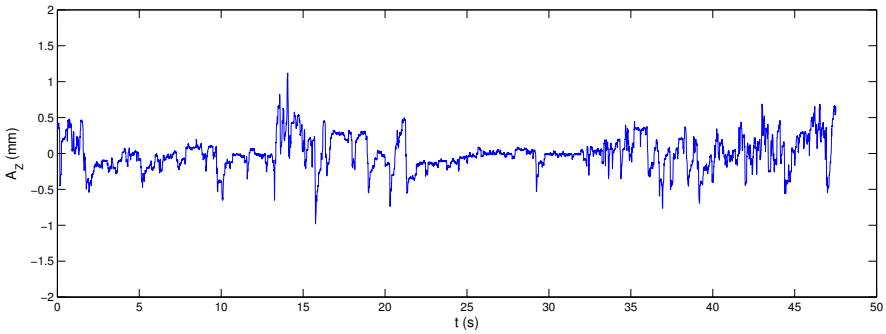

(c) Z Displacement

Figure H.9: Displacement time realization of $L/D = 4.0$ wire sample at $Tu = 7.5\%$ and $Re = 36,257$.

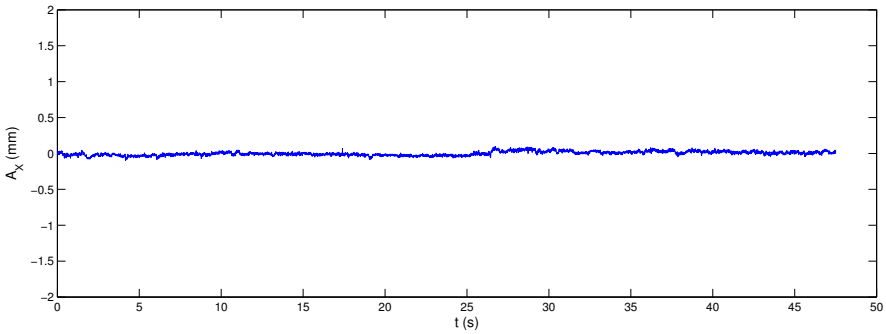

(a) X Displacement

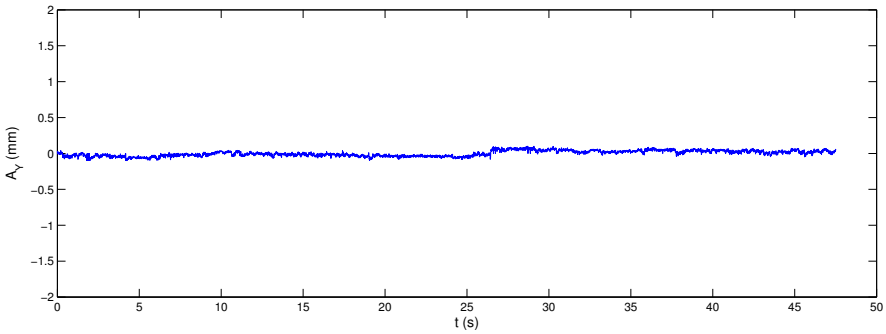

(b) Y Displacement

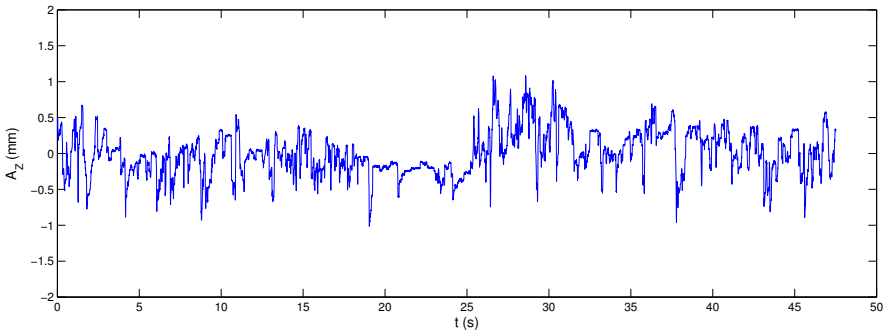

(c) Z Displacement

Figure H.10: Displacement time realization of $L/D = 4.6$ wire sample at $Tu = 7.5\%$ and $Re = 36,257$.

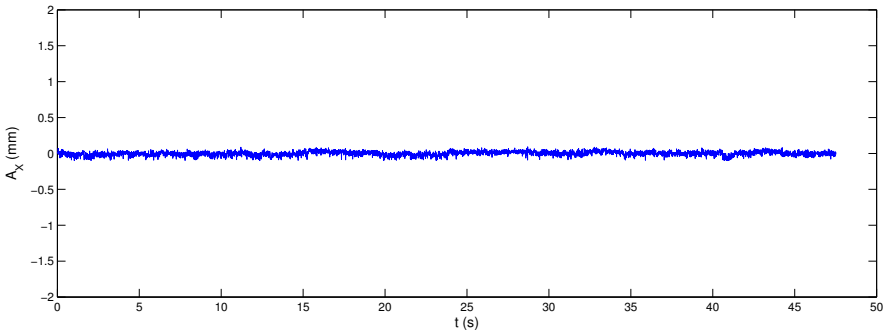

(a) X Displacement

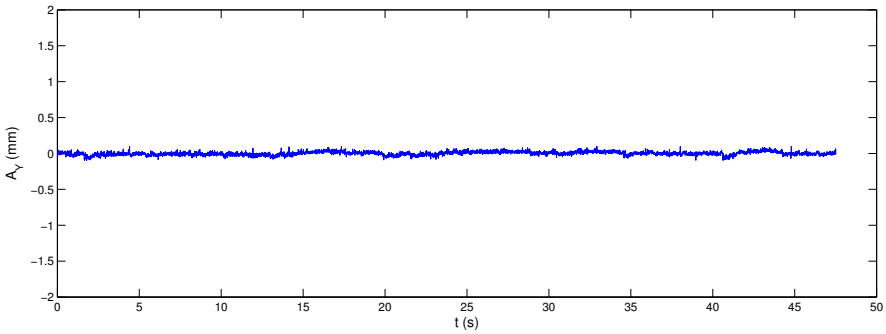

(b) Y Displacement

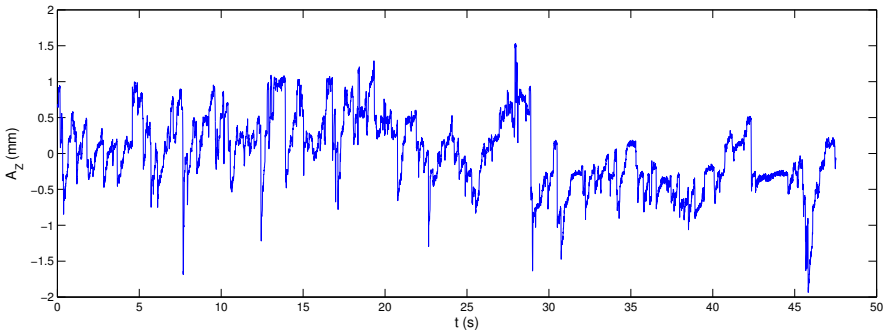

(c) Z Displacement

Figure H.11: Displacement time realization of $L/D = 2.8$ wire sample at $Tu = 7.5\%$ and $Re = 42,682$.

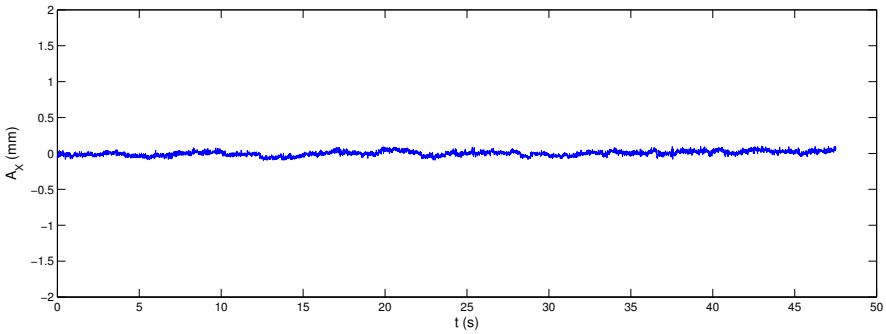

(a) X Displacement

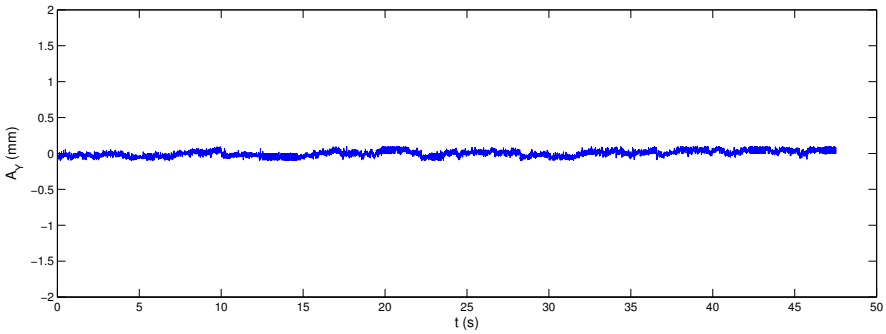

(b) Y Displacement

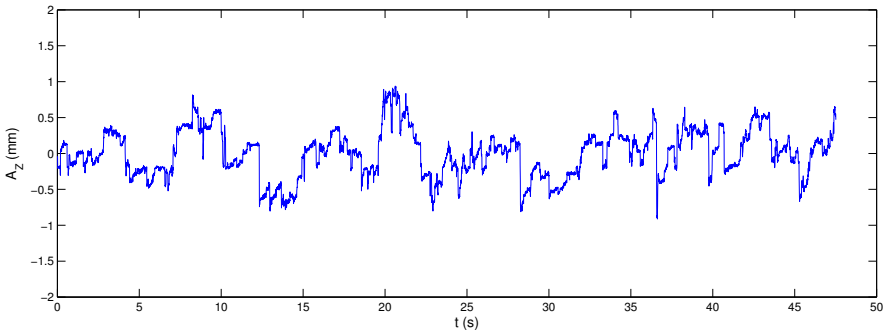

(c) Z Displacement

Figure H.12: Displacement time realization of $L/D = 3.4$ wire sample at $Tu = 7.5\%$ and $Re = 42,682$.

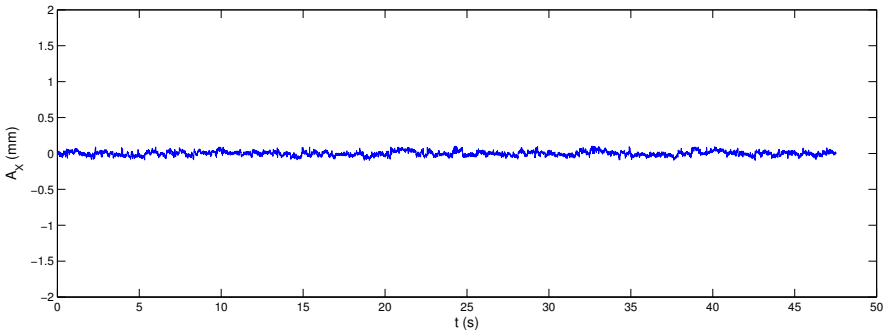

(a) X Displacement

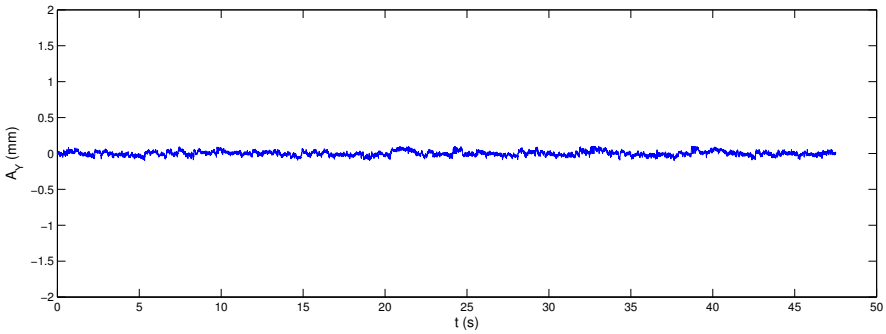

(b) Y Displacement

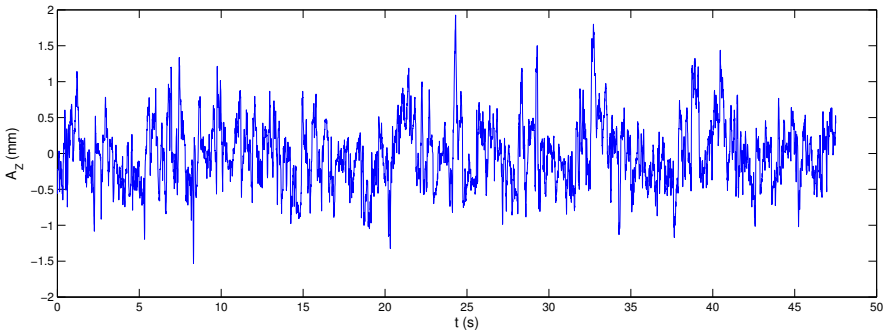

(c) Z Displacement

Figure H.13: Displacement time realization of $L/D = 4.0$ wire sample at $Tu = 7.5\%$ and $Re = 42,682$.

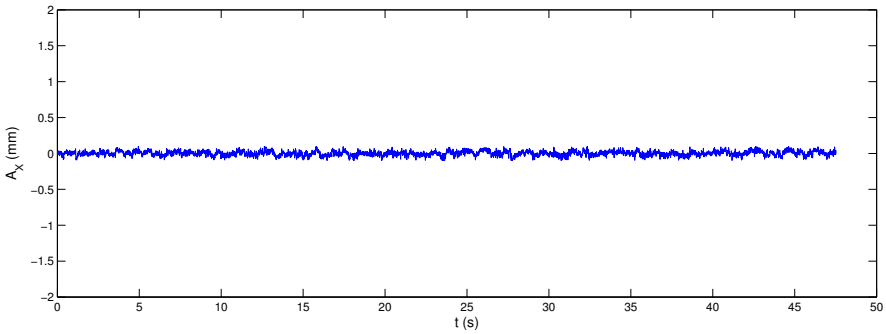

(a) X Displacement

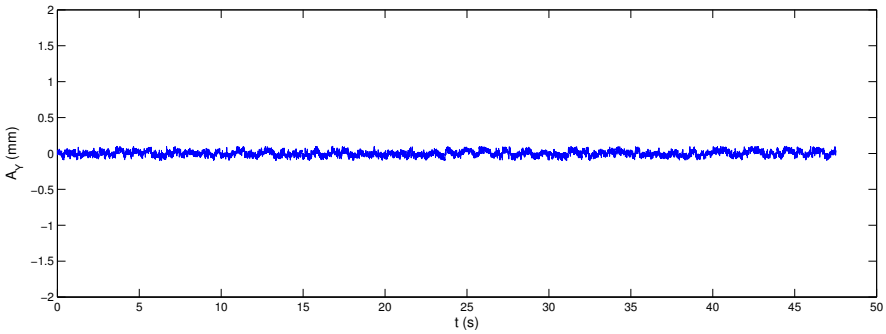

(b) Y Displacement

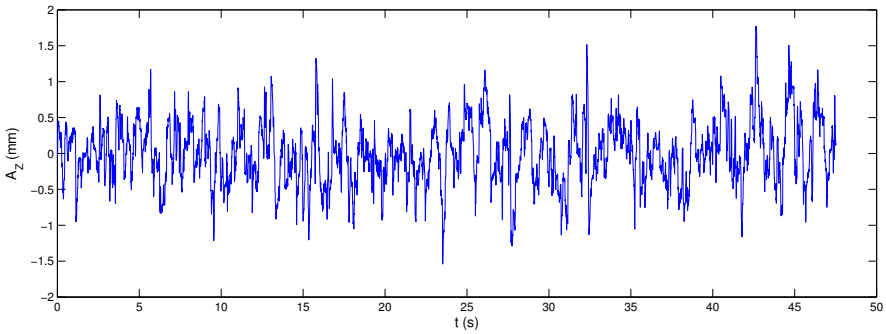

(c) Z Displacement

Figure H.14: Displacement time realization of $L/D = 4.6$ wire sample at $Tu = 7.5\%$ and $Re = 42,682$.

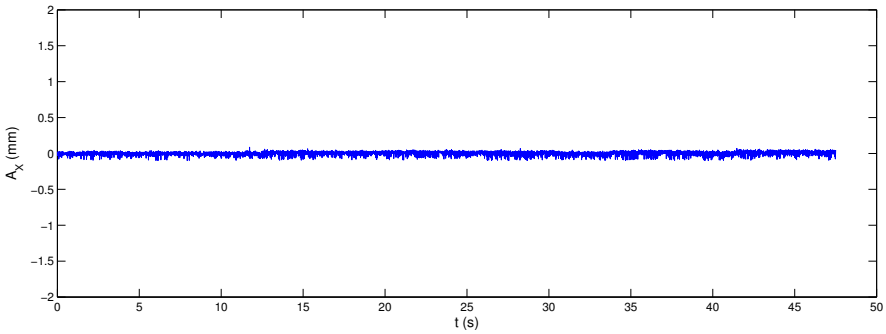

(a) X Displacement

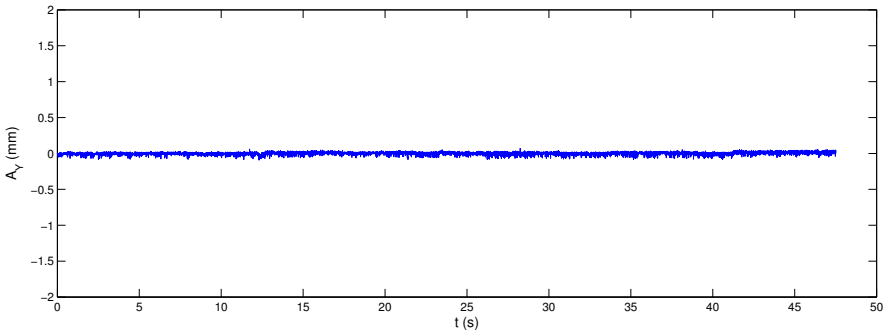

(b) Y Displacement

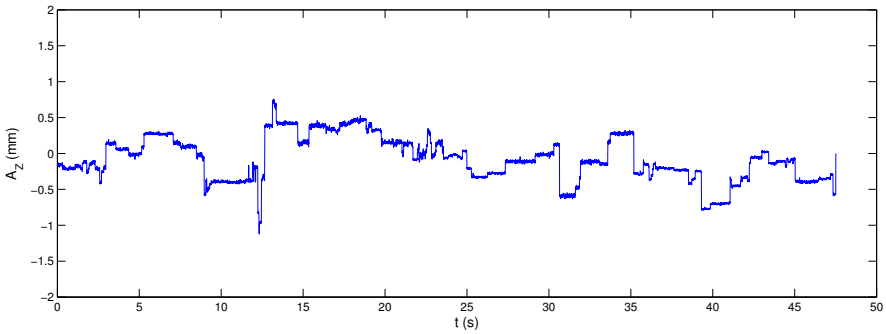

(c) Z Displacement

Figure H.15: Displacement time realization of $L/D = 3.4$ plate sample at $Tu = 7.5\%$ and $Re = 42,682$.

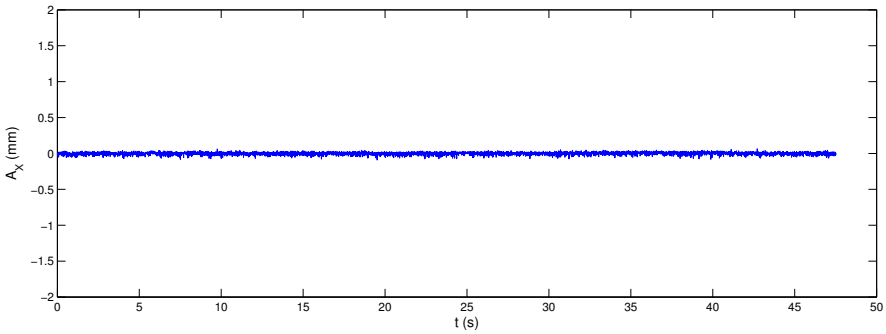

(a) X Displacement

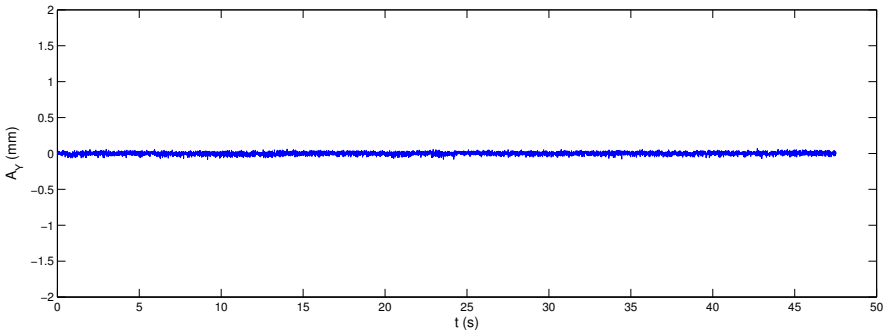

(b) Y Displacement

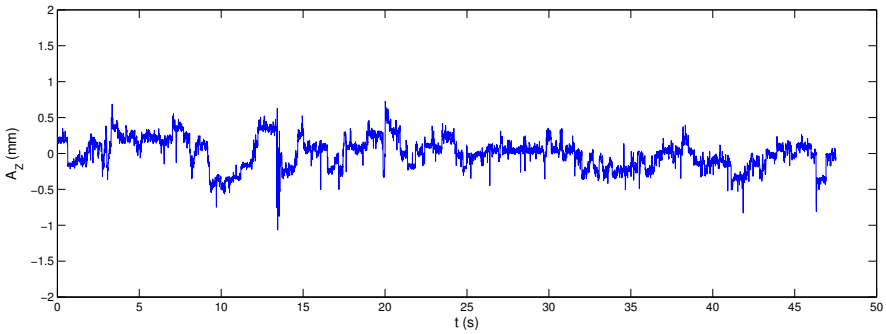

(c) Z Displacement

Figure H.16: Displacement time realization of $L/D = 4.0$ plate sample at $Tu = 7.5\%$ and $Re = 42,682$.

Appendix I

Stationary Plots

Figures I.1, I.2, I.3, and I.4, shows the running mean and rms plot for wire and plate samples. As can be seen in these graphs, the mean and rms value have converged for all wire and plate samples. As discussed earlier, the absence of any monotonic or fluctuating trend in these graphs indicate the vibration being weekly stationary.

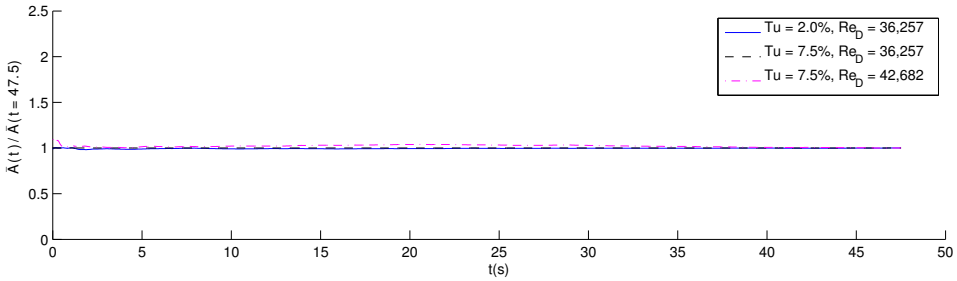

(a) Mean

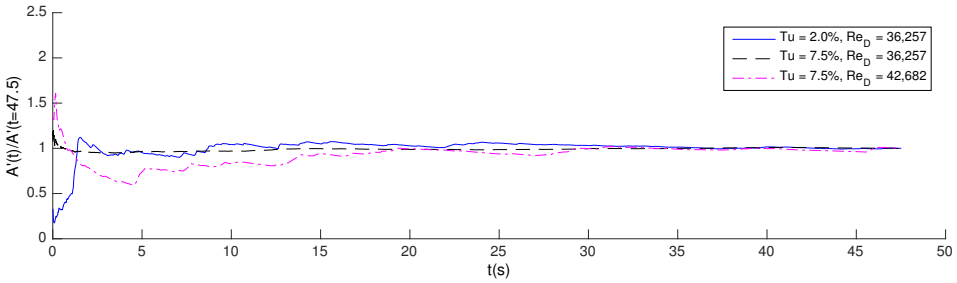

(b) RMS

Figure I.1: Running Mean and RMS of Z displacement time realization from wire samples with $L/D = 2.8$.

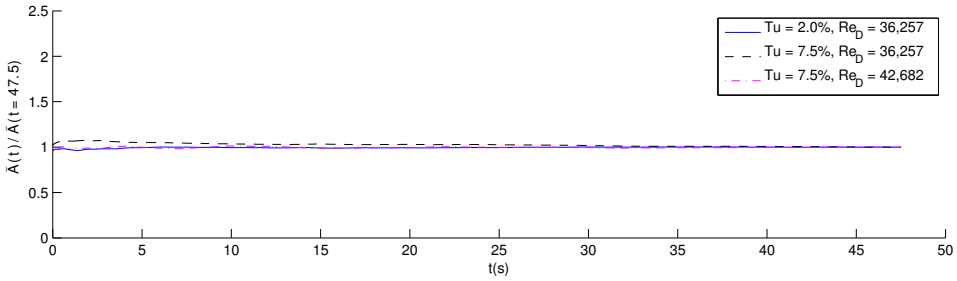

(a) Mean

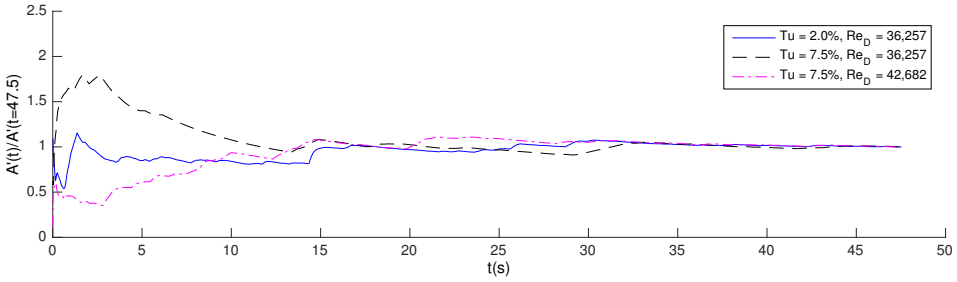

(b) RMS

Figure I.2: Running Mean and RMS of Z displacement time realization from wire samples with $L/D = 3.4$.

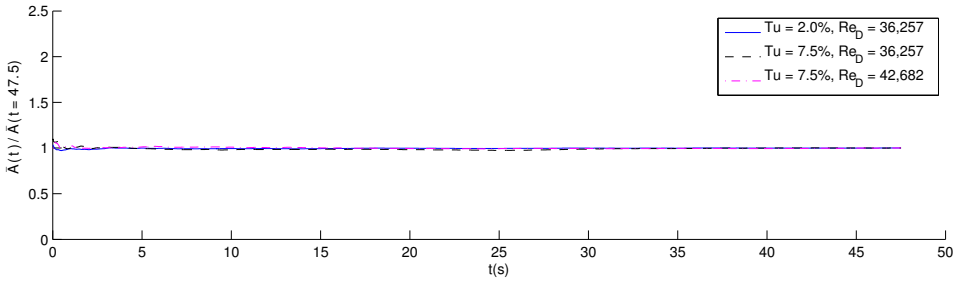

(a) Mean

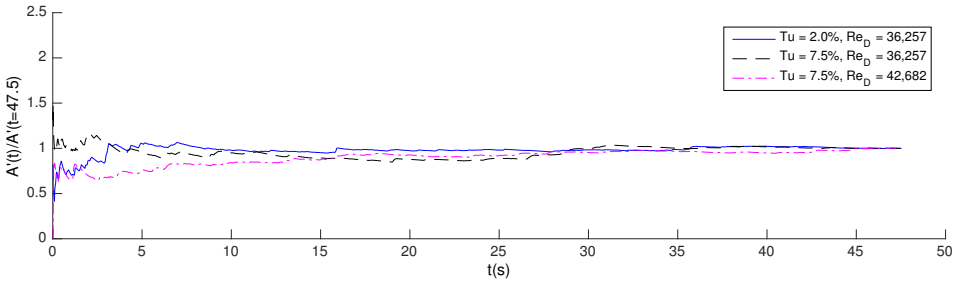

(b) RMS

Figure I.3: Running Mean and RMS of Z displacement time realization from wire samples with $L/D = 4.6$.

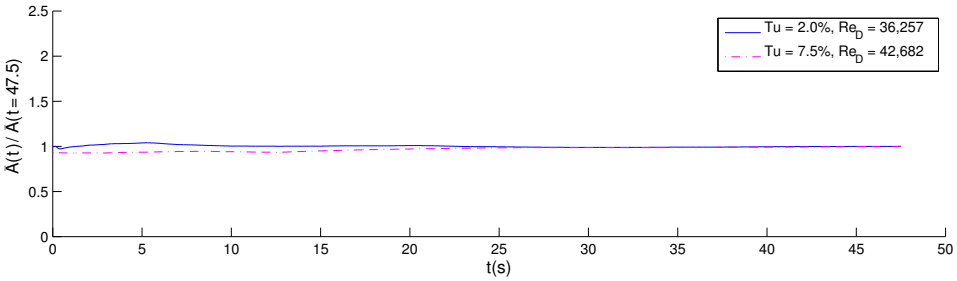

(a) Mean

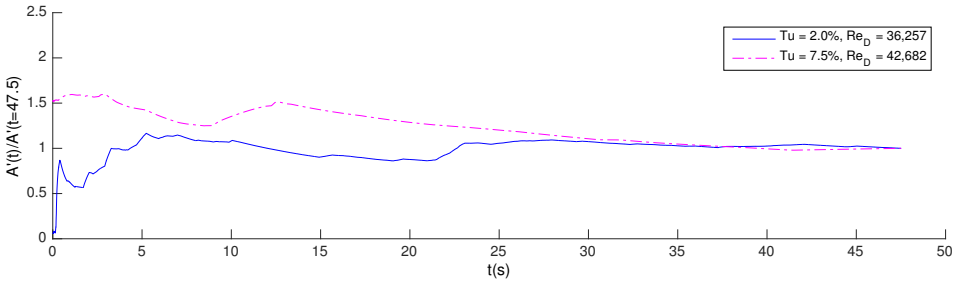

(b) RMS

Figure I.4: Running Mean and RMS of Z displacement time realization from plate samples with $L/D = 3.4$.

Appendix J

Reverse arrangement Hypothesis

This trend test is employed to confirm the stationarity of the data [100]. This test is very good at detecting monotonic trend and not fluctuating trends. Following assumptions are considered when employing this test: 1) If the random process in non-stationary, the statistical properties computed in each of the small time interval will vary significantly from each other. 2) Week stationariy is acceptable for current data analysis. 3) The time history is very long compared to the random fluctuation of the data.

Divide the time history Z(t) with time interval T, into n smaller time histories of time interval δT:

$$Z_1, Z_2, Z_3, ..., Z_n \tag{J.1}$$

Compute the RMS amplitude associated with each time history:

$$A_{RMS,Z_1}, A_{RMS,Z_2}, A_{RMS,Z_3}, ..., A_{RMS,Z_n} \tag{J.2}$$

Count the number of times $A_{RMS,Z_i} > A_{RMS,Z_j}$ for i < j:

$$h_{ij} = \begin{cases} 1 & \text{if } A_{RMS,Z_i} > A_{RMS,Z_j} \\ 0 & \text{otherwise} \end{cases}$$

Then, the reverse arrangement ξ_i is obtained as follows

$$\xi_i = \sum_{j=i+1}^{N} h_{ij} \tag{J.3}$$

and

$$\xi = \sum_{i=1}^{N} \xi_i \tag{J.4}$$

For sequence with n number of independent observations of a random variable, the mean and variance is obtained as follows:

$$\mu = \frac{n(n-1)}{4} \tag{J.5}$$

$$\sigma^2 = \frac{n(2n+5)(n-1)}{72} \tag{J.6}$$

For the hypothesis (i.e. the random response is stationary) to be true, reverse arrange-

ment ξ obtained from the above analysis should lie within the 95% confidence interval bounds.

Example: Time realization of Wire sample with length $L/D = 2.8$ vibrating at $Tu = 2.0\%$ and $Re_D = 36,257$ is split into n = 10 equal intervals with each interval containing 712 points. The rms value obtained from each interval is shown in Table J.1.

The number of reverse arrangements in the observations are shown in Table J.2. The total number of reverse arrangement is $\xi = 29$.

Assuming the observations are independent observation of random variable $A_{RMS,Z}$ with no trend. The acceptance region for this hypothesis is at 95% confidence interval is as follows:

$$\xi_{10;(0.975)} \leq \xi \leq \xi_{10;(0.025)} \tag{J.7}$$

the bounds are obtained from the literature, with $\xi_{10;(0.975)} = 12$ and $\xi_{10;(0.025)} = 33$ [100]. Since ξ lie within these bounds the hypotheses that rms is stationary is accepted.

Table J.1: RMS amplitude

i	A_{RMS,Z_i}
1	0.46
2	0.53
3	0.53
4	0.45
5	0.53
6	0.44
7	0.44
8	0.38
9	0.47
10	0.47

Table J.2: Reverse Arrangement

i	ξ_i
1	4
2	8
3	6
4	3
5	5
6	1
7	1
8	0
9	1

Appendix K

Contact Area

Inside tube bundle the angle between the central axis of the tube and foreign object in contact varies. For simplicity, it is assumed that the area of contact between wire and tube is the same as the area of contact of two cylinders with their central axis perpendicular to each other. This appendix calculate the contact area of two rigid body cylinders with their central axis perpendicular to each other as shown in Figure K.1a [2, 139]. Two cylinders with different diameter forms a contact area in the shape of an ellipses as shown in Figure K.1b. The semi-minor axis length (b) and semi-major axis length (a) of this ellipse are shown in Figure K.1b. It is important to note that the length (b) shown in this figure is in the Z direction. The length of semi-major axis is calculated using the following formula:

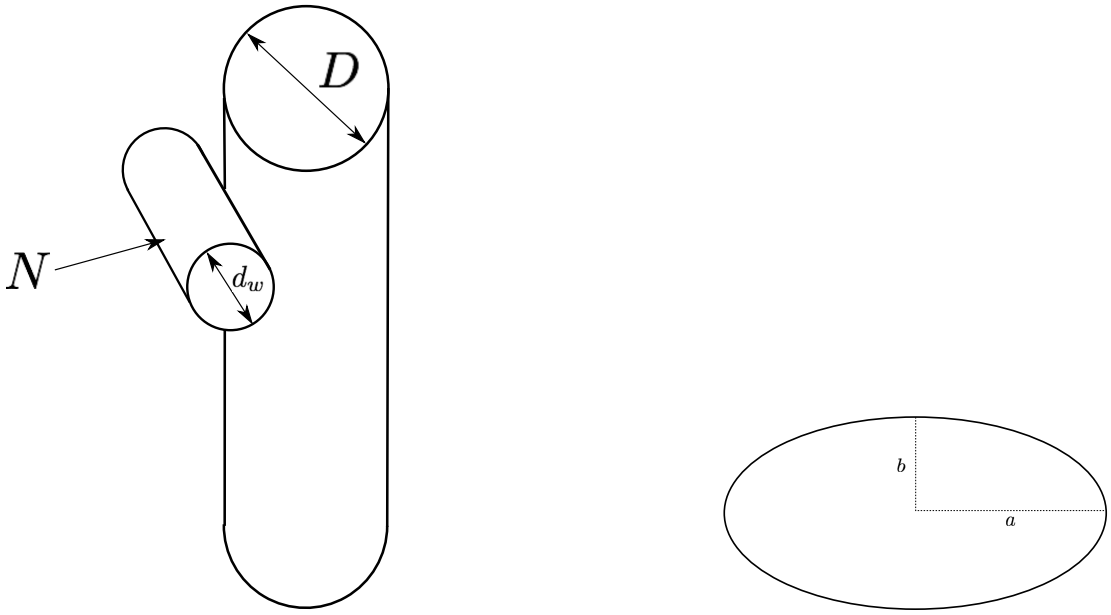

(a) (b)

Figure K.1: Contact area of two cylinders perpendicular to each other (a) Three-dimensional View (b) Contact area dimensions. Adapted from [2]

$$b = 0.909 n_b (Nk\gamma) \tag{K.1}$$

The length of semi-minor axis is calculated using the following formula:

$$a = 0.909 n_a (Nk\gamma) \tag{K.2}$$

here, n_b and n_a are constants obtained from literature and are calulated based on the ratio of the diameters and geometry [2], N is the normal force on the foreign object, k is obtained from the geometric parameters and γ is obtained using material properties. Force

(N) acting on the foreign object is calculated as follows:

$$N = \frac{\frac{1}{2} C_d \rho U_p^2 O_r}{e} \tag{K.3}$$

where, C_d is the drag coefficient, ρ is fluid density, U_p is pitch velocity, O_r is the frontal area of the foreign object and e is the number of tubes in contact with the foreign object. The frontal area (O_r) for the foreign object is calculated as follows:

$$O_r = d_w L(-cos(\phi)) \tag{K.4}$$

Constant k is calculated as follows:

$$k = \frac{d_w D}{d_w + D} \tag{K.5}$$

Constant γ is calculated as follows:

$$\gamma = \frac{1 - \nu_w^2}{E_w} - \frac{1 - \nu_D^2}{E_D} \tag{K.6}$$

where, ν_w and ν_D are Poission's ratio and E_w and E_D are modulus of elasticity for wire and tube respectively. Using the constants presented in Table K.1, the dimensions of contact area for wire samples of length $L/D = 4.0$ are calculated and are presented in Table K.2.

Table K.1: Constants for contact mechanics

Constants	Wire	Tube
$d_w\ (m)$	0.0012	-
$D\ (m)$	-	0.0175
$L\ (m)$	-	0.070
n_a	-	2.80
n_b	0.49	-
$E_w\ (GPa)$ [138]	193	-
$E_D\ (GPa)$ [140]	-	207
ν_w	0.24	-
ν_D	-	0.314
C_D	1.2	-
$\rho\ (Kg/m^3)$	998.2	998.2
e	2	2
$\phi(degrees)$	120	-

Table K.2: Contact Dimensions

$U_p\ (m/s)$	$b(m)(10^{-6})$	$a(m)(10^{-6})$
2.11	2.8	16.0
2.68	3.3	18.8
3.45	3.9	22.3
4.22	4.4	25.4
4.98	4.9	28.4
5.75	5.4	31.3
6.51	5.9	34.0
7.28	6.4	36.6
7.67	6.9	37.9